UNIONE EUROPEA
Fondo Sociale Europeo

Ministero dell'Università e della Ricerca

PON RICERCA E INNOVAZIONE 2014 - 2020

UNIVERSITÀ DELLA CALABRIA

UNIVERSITY OF CALABRIA
Department of Pharmacy and Health and Nutrition Science
(DFSSN)

PhD Course
Translational Medicine

Granted by
Ministry for Universities and Research (MUR)

Cycle
XXXVI

"DESIGN AND SYNTHESIS OF SMART MESOPOROUS SILICA-BASED NANODEVICES FUNCTIONALIZED WITH SMALL MOLECULES AND PEPTIDES FOR TARGETED CANCER THERAPY"

Scientific disciplinary sector CHIM/06

Coordinator: Ch.mo Prof. Stefania Catalano
Signature ________________________

STEFANIA
CATALANO
15.07.2024
12:45:41
GMT+01:00

Supervisor/Tutor: Ch.mo Prof. Antonella Leggio
Signature________________________

PhD student: Dott. Marzia De Santo
Signature_______________________

Abstract

My PhD research project focused on the design and synthesis of mesoporous silica-based nanoframworks for the targeted delivery of anticancer drugs.

The use of nanomaterials for cancer treatment has revolutionized chemotherapy, improving drug efficacy and safety while reducing side effects. Mesoporous silica nanoparticles (MSNs) offer unique advantages, including tunable pore size and shape, easy surface functionalization, high loading capacity, and excellent biocompatibility, making them a promising platform for cancer therapy.

Initially, my PhD research activity was concentrated on developing highly selective MSN-based nanosystems for the smart administration of bortezomib (BTZ), a first-line treatment for multiple myeloma.

A novel bortezomib (BTZ) delivery system, named FOL-MSN-BTZ, was developed using NanoSiliCal Devices' proprietary MSN technology. NanoSiliCal Devices, an innovative PMI and spin-off from the University of Calabria, hosted me for an 18-month internship during my doctoral studies.

The engineered FOL-MSN-BTZ nanodevices consists of MSU-type mesoporous silica nanoparticles able to selectively delivery bortezomib to folate receptor overexpressing multiple myeloma (FR+ MM) cells. The receptor-specific ligand, folic acid (FOL), grafted on the external surface of MSNs, allows tumor recognition and cell internalization, while BTZ linked to the pore internal surface by a pH-responsive bond, is released in a slightly acidic tumor microenvironment. By carefully balancing the different functionalities on the external and internal surface of MSNs we identified an optimized nanostructure that selectively induces death in FR+ tumor cells while sparing

FR- healthy cells. After an accurate suspendability assessment, injectable FOL-MSN-BTZ suspensions showed a significantly higher *in vivo* anticancer efficacy, and a better safety profile compared to conventional BTZ administration.

Building on the remarkable *in vitro* and *in vivo* results of FOL-MSN-BTZ, we developed a new MSN-based nanodevice for the selective delivery of doxorubicin (DOXO). DOXO is a potent chemotherapeutic agent effective against a wide range of cancers but is associated with serious side effects, such as cardiotoxicity and myelosuppression. To mitigate these toxicities and enhance therapeutic performance through site-specific targeting and controlled release, we created the FOL-MSN-DOXO nanodevice.

In this system, folic acid is again used as the targeting molecule on the external surface of the mesoporous silica nanoparticles (MSNs), while doxorubicin is conjugated to the internal pore walls through an acid-labile hydrazone bond. The FOL-MSN-DOXO nanosystem selectively targets FR-overexpressing cancer cells, while sparing the FR-low normal cells. Furthermore, FOL-MSN-DOXO uptake occurred via FR-mediated endocytosis.

Additionally, a more specific DOXO-loaded prototype, HER2PEP-MSN-DOXO, featuring a peptide ligand on its external surface that can recognize the HER2 receptor, was designed and developed. This receptor is a crucial therapeutic target in treating HER2-overexpressing (HER2+) breast cancer. In this innovative design, the folic acid previously used on the MSNs' external surface was replaced with a peptide ligand specifically engineered to target the HER2 receptor.

The interactions of the designed peptides with the HER2 receptor were studied and evaluated through computational analysis. After identifying the optimal amino acid sequence for interacting with HER2, we synthesized the sequence using solid-phase methodologies and anchored it to the external surface of the silica nanoparticles. The obtained nanosystem significantly inhibited the proliferation of HER2-positive cancer cells, without affecting the growth of HER2-negative healthy cells. The uptake of HER2PEP-MSN-DOX in HER2+ cancer cells occurred though HER2-mediated endocytosis.

During a six-month period at the Institute Charles Gerhardt Montpellier (ICGM) in France, under the supervision of Prof. Colacino, my PhD research focused on preparing hybrid mesoporous silica-based materials using innovative, eco-friendly mechanochemical methodologies. The aim was to functionalize mesoporous silica nanoparticles (MSNs) with appropriate linkers and targeting molecules.

By employing mechanochemical synthetic approaches, we selectively functionalized MSU-type starting materials on both their external and internal surfaces, creating nanodevices suitable for potential drug delivery applications. The primary goal was to optimize the traditional solvent-based process by minimizing solvent usage, waste generation, and reaction times, thereby enhancing overall process efficiency and eco-friendliness.

Targeting molecules, such as small peptides, were effectively grafted onto the external surfaces of the MSNs. Additionally, the internal surfaces were successfully modified with organosilanes to develop stimuli-responsive linkers. Mechanochemical methods were also employed to improve the extraction of surfactants from within the pores of the MSNs, significantly reducing water consumption during the process.

In conclusion, my PhD research on mesoporous silica-based systems for controlled release and targeted delivery of anticancer drugs has highlighted significant advancements in the field of targeted therapies and the strategic shift toward molecular multi-targeted approaches. While traditional methods like molecular recognition and pH sensitivity are still effective, the future of cancer treatment lies in molecular multi-targeted therapies, with nanotechnology playing a pivotal role in drug design. To address the complex nature of cancer and improve therapeutic outcomes in terms of both efficacy and reduced toxicity, a polypharmacology approach utilizing Molecular Multi-Targeted Nanostructured (MMTN) cancer therapeutics is proposed in perspective.

The hypothesized MMTN device consists of mesoporous silica nanoparticles with an antibody-mimicking peptide on the external surface, connected via an uncleavable bond, and two small molecules inside the silica pores linked with a pH-sensitive bond that hydrolyses in the acidic tumor microenvironment. This design allows the antibody-mimicking peptide to inhibit extracellular target proteins, while the small molecules penetrate the cell to target intracellular proteins, resulting in a synergistic attack on cancer cells.

This thesis encompasses published work (papers), completed studies awaiting publication, and ongoing research. Peptide sequences and part of experimental data of the synthesized systems have been omitted for confidentiality reasons, as patent applications are currently in progress.

Table of Contents

INTRODUCTION 1

MESOPOROUS SILICAS IN MATERIALS ENGINEERING: NANODEVICES FOR BIONANOTECHNOLOGIES **1**
- Mesoporous silica nanoparticles (MSNs): synthesis and properties 3
- Design of Mesoporous silica nanoparticles for drug delivery 6
  - *Surface targeting strategy* 6
  - *Drug delivery: Stimuli responsiveness strategy* 8
- Pharmacokinetics, biocompatibility, and toxicity of MSNs 10
- References 13

CHAPTER 1 19

ENGINEERED MESOPOROUS SILICA-BASED NANOPARTICLES AS SMART CHEMOTHERAPY NANODEVICE FOR BORTEZOMIB ADMINISTRATION **19**
- 1.1 Introduction 19
- 1.2 Synthesis and optimization of MSN-based nanodevice for the smart administration of Bortezomib 24
  - *1.2.1 Results and Discussions* 24
  - *1.2.2 Experimental* 43
- 1.3 Conclusion 55
- References 56

CHAPTER 2 59

FUNCTIONALIZED MESOPOROUS SILICA-BASED NANOFRAMEWORKS FOR SMART DELIVERY OF DOXORUBICIN TO CANCER CELLS **59**
- 2.1 Introduction 59
- 2.2 Synthesis and in vitro evaluation of FOL-MSN-DOXO prototype 65
  - *2.2.1 Results and Discussion* 65
  - *2.2.2 Experimental* 76
- 2.3 Synthesis of HER2-targeted mesoporous silica nanoparticles for DOXO delivery in breast cancer (HER2PEP-MSN-DOXO) 83
  - *2.3.1 Results and Discussion* 83
  - *2.3.2 Experimental* 100
- 2.4 Conclusion 110
- References 112

CHAPTER 3 117

DESIGN AND SYNTHESIS OF HYBRID MATERIALS USING INNOVATIVE ECO-FRINEDLY METHODOLOGIES BASED ON MECHANOCHEMISTRY **117**
- 3.1 Introduction 117
  - *3.1.1 Green chemistry and green metrics* 117
  - *3.1.2 Mechanochemistry and mechanochemical methods* 119
- 3.2 Mechanochemical modification of mesoporous silica-based nanoparticles 122
  - *3.2.1 Results and Discussion* 122
  - *3.2.2 Experimental* 137

3.3 Conclusion and possible future prospects 137
References 138

CHAPTER 4 ***142***

THE ADVENT OF MOLECULAR TARGETED THERAPIES AGAINST CANCER: TOWARDS MULTI-TARGETING DRUGS THROUGH MATERILAS ENGINEERING: A POSSIBLE FUTURE **142**
References 148

Introduction

MESOPOROUS SILICAS IN MATERIALS ENGINEERING: NANODEVICES FOR BIONANOTECHNOLOGIES

Elisabetta Mazzotta, Marzia De Santo, Domenico Lombardo, Antonella Leggio, and Luigi Pasqua

Published on: *Materials Today Bio*, **2022**, 17, 100472.

DOI: 10.1016/j.mtbio.2022.100472.

Cancer is a devasting disease affecting millions of people all over the world, presenting significant therapeutic challenges. According to the latest World Health Organization (WHO) statistics, there were 20 million new cancer cases and 9.7 million deaths in 2022, with a projected global burden of 35 million cases by 2050 [1]. Conventional cancer therapeutic approaches involve surgery, chemotherapy, and radiotherapy [2]. Among these, chemotherapy is widely used but has significant drawbacks. Chemotherapy agents lack specificity towards cancer cells, leading to damage to healthy tissues and causing serious adverse effects. These side effects can impact the dosage or follow-up [3]. Additionally, cancer cells can develop resistance to chemotherapy, leading to treatment failure and reducing patient adherence and quality of life [4].

In recent years, innovative drug delivery technologies have been widely developed to overcome limitations and improve therapeutic outcomes, such as reducing toxicity, ensuring target specificity, maximizing efficacy, enhancing safety, and increasing compliance of patients [5].

Drug delivery systems (DDSs) are smart platforms designed to store biological active substances, ensuring targeted and controlled release. Common administration routes of DDSs in *in vivo* cancer models are intravenous, intra-tumor, and localized [6].

The rapid evolution of nanotechnology has significantly revolutionized cancer treatment, leading to the development of nanomedicine and nanoscale DDSs.

The incorporation of a drug in a nanocarrier can improve its solubility and stability, facilitate transmembrane transport, overcome anatomical and chemical barriers within the tumour microenvironment and prolong drug's circulation time [7, 8].

Due to their unique physiochemical and biological properties, nanoparticles (NPs) have significantly enhanced the effectiveness of anticancer agents. Nanoparticles can be opportunely engineered to achieve specific surface properties that allow them to selectivity target tumour cells while sparing healthy ones, thereby reducing the side effects of drugs [9].

In addition, nanoparticles (NPs) can be designed to release their payloads in a controlled manner, ensuring sustained drug delivery over time [10].

The design of NP-based drug delivery system is constantly evolving to meet the medical needs and complexity of cancer disease and progression. Various classes of NPs have been utilized, each offering distinct advantages and disadvantages in terms of cargo loading, delivery, and patient compliance.

Lipid-based NPs are the most common type of FDA-approved nanomedicine [11]. They typically consist of a lipid bilayer surrounding at least one internal aqueous compartment, resulting in simple, self-assembling, biocompatible, and highly bioavailable delivery systems with enhanced payloads flexibility [12]. Recently lipid-based NPs have emerged as a viable platform for delivering of nucleic acids [13]. However, lipid-based NPs generally exhibit low drug capability and limited biodistribution [14].

Polymeric NPs can be carefully formulated with controlled particle properties, enabling the delivery of hydrophobic and hydrophilic compounds, as well as cargo with different molecular weights [15]. They are synthesized and surface-modified using different techniques [16]. However, the main disadvantages of polymeric NPs include a tendency for particle aggregation and potential toxicity [17].

Inorganic materials, such as iron, gold, and silica are precisely formulated and engineered in a wide variety of sizes, shapes, and geometries, providing nanostructured systems for therapeutic and theragnostic purposes [18]. These materials possess good biocompatibility and stability. However, their clinical applications are limited due to low solubility and toxicity concerns, particularly with formulations that use heavy metals [19, 20].

Mesoporous silica nanoparticles (MSNs): synthesis and properties

Among the innovative approaches proposed for cancer therapies, mesoporous silica nanoparticles offer a highly promising architecture for bionanotechnology applications [21]. Mesoporous silica nanoparticles (MSNs) have emerged as exiting DDSs thanks to their unique and intrinsic properties, including high loading capability due to large surface area and high pore volume, favourable biocompatibility and biodegradability, and chemical stability [22].

Additionally, MSNs surface properties can be easily modulated, allowing for the customization of pore size, chemistry, and shape, crucial issues for effective drug delivery. Interestingly, MSNs have been extensively investigated both *in vitro* and *in vivo*, demonstrating excellent performance and safety [23, 24].

According to IUPAC, MSNs are a class of porous material with an order pore structure, featuring pore diameters ranging from 2 to 50 nm. MSNs were first synthesized in the early 1990s by Kresge *et al*. at the Mobile Research and Development Corporation [25], naming them Mobil Corporation of Matter (MCM-41). The fabrication process involves using an amphiphilic surfactant as structure-directing agent combined with a silica precursor, resulting in an ordered hexagonal mesophase. Since then, several prototypes with different physicochemical properties have been developed by changing silica source, surfactant templates, and reaction conditions. MSNs can be categorized in various types, such as Santa Barbara (SBA, the most important SBA-15 and SBA-16) [26], Mobile Corporation of Matter (MCM) (MCM-41, 48, and 50) [27- 29], Michigan State University (MSU) [30], and Hexagonal Mesoporous Silica (HMS) [31].

The synthesis of the ordered mesoporous silica materials primarily relies on templating method that employs a silica source, such as tetraethoxysilane (TEOS) and an amphiphilic surfactant like cetyltrimethylammonium bromide (CTAB) acting as structure-directing agent. This strategy, known as Ströber method or sol-gel method [32], involves initially dissolving the surfactant molecules to self-arrange into micelles at an alkaline pH above the critical micelle concentration (CMC). Afterward, the added silica interacts with the micelles through electrostatic interactions established between the inorganic silica and organic surfactants, leading to the formation of an ordered mesoarchitecture. The silica condenses around the polar heads of the surfactant micelles, forming a layered structure. Mesopores can be made accessible by surfactant removal via calcination or solvent extraction processes (Figure 1).

The precise control of the interfacial tensions during the self-assembly of micelles and silica condensation is crucial for achieving the desired particles size and shape, as well as tunable pore sizes [33].

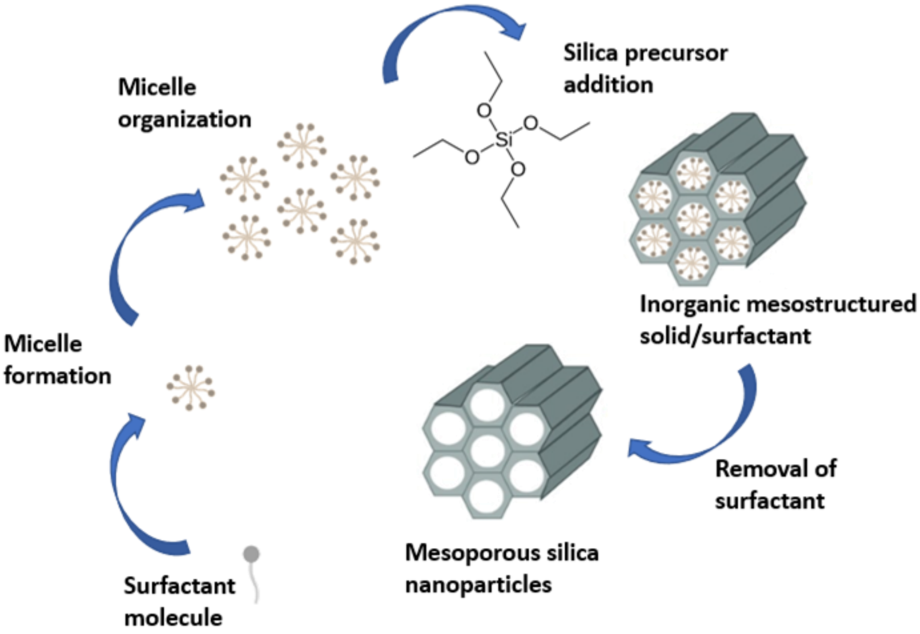

Figure 1. Schematic illustration of sequential steps of the fabrication process of MSN materials.

MSNs properties, such as shape and size, can be well-modulated by changing synthesis conditions, including surfactant, silica source and solvent, and/or modifying operative parameters like pH, temperature and stirring speed [34-36].

The sol-gel method involves two main stages: the hydrolysis of precursor in the medium and the condensation of the hydrolysed product.

MSNs particle size is mostly controlled by the pH of the reaction medium. A decrease in pH results in a smaller particle size. Fang *et al.* observed that as the pH decreased to 11.38, 11.32, and 11.00, the average size of synthesized particles changed to 170, 110, and 50 nm, respectively [37]. However, other parameters such as silica concentration, reaction time and temperature, catalyst, co-solvent, and water amount also affect particle size [38, 39].

The choice of surfactant molecules can influence pore dimensions. Surfactants with longer chain lengths form MSNs with larger pores compared to those with shorter chain lengths [40]. Moreover, increasing the concentration of CTAB surfactant results in highly disordered mesostructure [41], a similar effect is observed with an increase in TEOS concentration [39].

Finally, different MSNs shapes can be realized by varying molar concentration of TEOS, surfactant, and base catalyst. For example, Cai *et al.* synthesized MSNs of various shapes, including silica rods, oblate silica of nanometric size, and spherical shape, by changing the concentration of CTAB, TEOS, and NH_4OH/NaOH [42].

Design of Mesoporous silica nanoparticles for drug delivery

Surface targeting strategy

MSNs surfaces are covered with a large amount of silanol groups (Si-OH), making them highly susceptible to internal and external surface modifications [43]. These modifications can confer new physical and chemical properties to the mesoporous materials, expanding their suitability for various applications.

In drug delivery, functionalization of MSNs surfaces is a common approach to achieve selectivity to targeted tissue, increase the specificity of therapeutic treatments, reduce adverse effects, and even overcome multi-drug resistance.

Two main techniques for MSN modification are co-condensation and grafting. The first is a direct method involving sol-gel chemistry between the tetralkoxysilanes and one or more organoalkoxysilane [44]. This approach results in a more homogeneous coverage of functional groups [45] but can lead to a less ordered final structure [46].

Grafting is a post-fabrication process that involves the attachment of functional groups to the pre-formed silica network. This approach does not alter silica mesostructured [47], allowing for easy control over particle size, morphology and pore diameters [48].

Targeted drug delivery systems can involve passive or active targeting. Passive targeting refers to the accumulation of DDSs at the desired site due to pharmacological or physiochemical factors [49]. In cancer treatment, the disordered, discontinuous, and highly fenestrated tumor microenvironment allows nanoparticles to accumulate in tumor tissue through passive extravasation mediated by the enhanced permeability and retention (EPR) effect [50]. The anatomical and functional irregularities in tumor vasculature increase the permeability of nanoparticles compared to the normal tissue. DDS properties, such as surface chemistry and charge, size, hydrophobicity, and biocompatibility, can affect the EPR mechanism [51].

Active targeting relies on the overexpression of specific receptors in cancer cells compared to normal cells [52]. The conjugation of targeting molecules to the external surfaces of nanoparticles enhances cellular uptake through the molecular recognition between the ligand and the overexpressed receptors in tumors [53].

Various targeting ligands have been explored for the development of tumor-targeted drug delivery systems, including, small molecules (i.e. folic acid) [54], proteins [55], small peptides [56], antibodies [57], and aptamers [58].

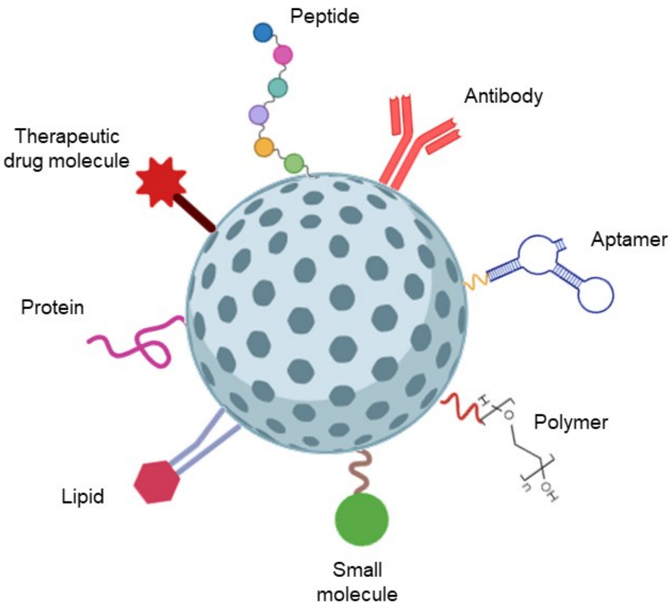

Figure 2. Examples of different moieties that can be conjugated to MSNs for effective cancer treatment.

Drug delivery: Stimuli responsiveness strategy

Even though targeting improves the efficiency of the drug delivery systems, it does not prevent the premature drug release from DDSs or ensure optimal release of the drug once the target site is reached [59]. The ideal DDSs should hamper the premature or incomplete release of the cargo upon reaching the target site [60]. To achieve this, stimuli-responsive DDSs have been developed to enhance the effectiveness of targeted strategies. The design of stimuli responsive nanocarriers considers the differences between tumor microenvironment (TME) and normal tissues.

Stimuli-responsive nanocarriers can respond to external stimuli such as magnetic fields, temperature, ultrasound, and light, or internal stimuli, including pH, ATP, enzyme, redox potential, and hypoxia. These stimuli may be present inside cancer cells or within the TME [61].

Recent advancements include dual- or multi-stimuli approaches, showing superior performance in drug delivery and release. Unlike single-stimulus systems, multi-stimuli DDSs incorporate several activable strategies within a single nanocarrier, allowing them to respond to various stimuli either individually or simultaneously [62].

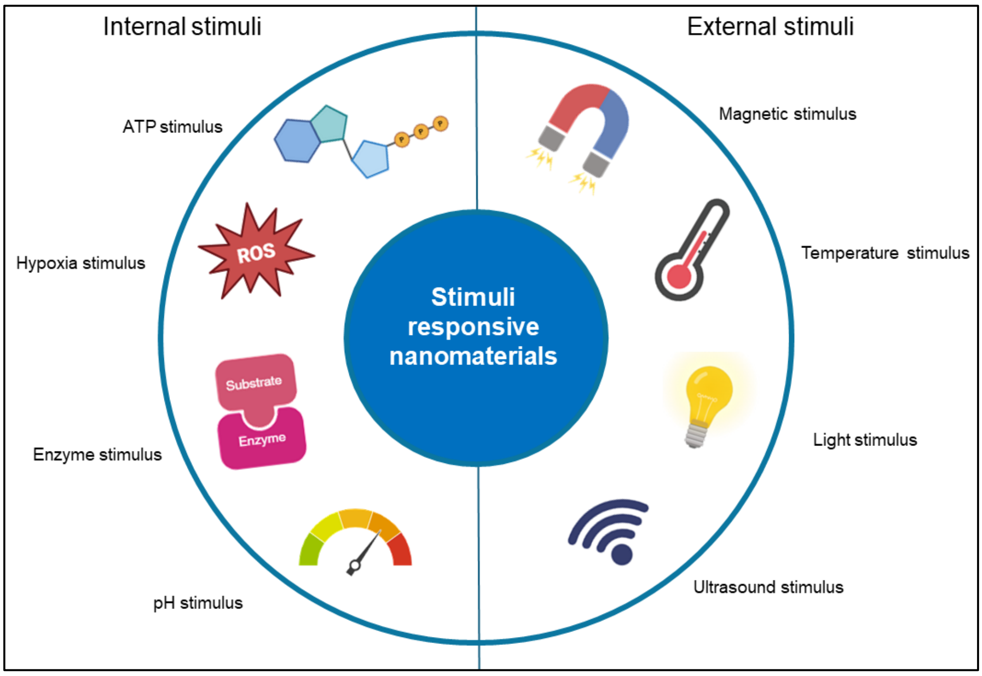

Figure 3. External and internal stimuli responsive strategies in drug delivery systems.

Stimuli responsive MSN-based nanosystems enable the conjugation of therapeutic agents inside the pore walls using stimuli-responsive bonds, linkers, or substrates. These systems ensure that the therapeutic agents are released only at the targeted site in response to specific stimuli [63].

Given the pH differences between normal and tumor tissues, as well as between intra- and extracellular environments, pH responsive nanoplatforms are widely utilized as effective tools to prevent unspecific and uncontrolled drug release. These nanoplatforms store drugs in normal pH conditions and release them exclusively in the acidic tumor microenvironment. To achieve this, different pH-sensitive chemical bonds such as hydrazone [64], imine [65], oxime [66], amide [67], acetal [68], and orthoester [69], are incorporated within the internal surfaces of the nanocarrier.

Beside the cleavage of acid-labile chemical bonds, another mechanism for constructing pH-sensitive nanosystems involves the protonation approach. This method uses polymers with ionizable pendant groups to modify nanocarrier properties. These functional groups can accept or donate protons in response to the pH changes, triggering the release of the drug [70, 71].

Pharmacokinetics, biocompatibility, and toxicity of MSNs

The rational design of MSN-based drug delivery systems should carefully consider the crucial role of important physicochemical parameters, such as morphology, size, shape, surface area and charge. These factors strongly impact the *in vivo* performance, biodistribution, and biocompatibility of MSNs [72].

The degradation of MSNs in the body is mostly influenced by their morphology, surface area and surface modification, and drug loaded. Spherical MSN degrade faster than rod-shaped ones due to their larger interaction area with the physiological environment [73]. The degradation rate can also be increased by adding cations like Ca^{2+} and Fe^{3+}, which disrupt the silica network [74, 75].

Degradation of MSNs can be optimized with coating of nanoparticles with macromolecules and polymers, such as PEG. Depending on the density of the coverage and the chain length of polymer, PEGylation significantly reduces the dissolution rate, promoting disintegration of MSNs [76]. Recent studies have also shown that drug loading within the MSN pores enhances *in vitro* degradability [77].

MSNs are generally recognized as highly biocompatible materials, degrading into silicic acid, that is safe and naturally present in body [78].

The biocompatibility and biodistribution of MSNs can be tailored by adjusting surface properties. In a study by He and coworkers, the effect of PEGylation and particle size on the *in vivo* biodistribution and urinary excretion were investigated. They found that PEGylated MSNs of various sizes primarily accumulated in the liver and spleen. Grafting with PEG prevented the MSNs from being captured by liver, spleen, and lung, especially for larger nanoparticles, resulting in longer blood-circulation lifetime [79].

Additionally, adding various surface moieties and reducing the overall surface charge can significantly lower the cytotoxicity of MSNs [80].

In a mouse model study, Liu *et al.* demonstrated that MSNs exhibit good biocompatibility even at higher doses, with a lethal dose for 110 nm MSNs exceeding 1000 mg/kg. After multiple administrations, no deaths were observed in mice over 14 days [81].

Nanoparticles size primarily affects their biodistribution. Typically, nanoparticles greater than 200 nm are quickly removed from bloodstream and accumulate in the liver and spleen, while particles smaller than 10 nm are rapidly cleared by the kidneys [82].

Larger MSNs may cause more adverse effects in organs and tissues, such as inflammation, oxidative stress, dysfunction, due to their slower clearance rate and longer retention time in body [83].

MSNs cytotoxicity is mainly associated with the silanol groups on nanoparticles surface. The negative charge of MSNs increases the risk of interactions with red blood cells, which can lead to hemolysis, and may also trigger unintended immune responses, leading to *in vivo* protein opsonization [84].

The phenomenon of protein corona consists of the adsorption of plasma protein onto the surface of nanoparticles, affecting their circulation lifetime, accumulation in tissue, cellular uptake, and consequently their therapeutic response [85, 86].

The safety and performance of MSNs are affected by their shape and structure. For example, rod-shapes MSNs are more readily taken up by cells and exhibit longer retention compared to spherical MSNs [87].

MSNs pore size also affects their anticancer efficacy. MSNs with medium pore size (around 5 nm) exhibit higher cellular uptake and nucleic accumulation, stronger anti-proliferative effects and induction of cell apoptosis in tumor tissues *in vitro*, and efficient suppression of *in vivo* tumor growth compared to MSNs with smaller or larger pore sizes [88].

References

1. Global cancer burden growing, amidst mounting need for services, World Health Organization, 1 February 2024, https://www.who.int/news/item/01-02-2024-global-cancer-burden-growing--amidst-mounting-need-for-services.
2. Hoda, M. Potential Alternatives to Conventional Cancer Therapeutic Approaches: The Way Forward. Current Pharmaceutical Biotechnology, 2021, 22(9), 1141-1148.
3. Ingrand, I., Defossez, G., Lafay-Chebassier, C., Chavant, F., Ferru, A., Ingrand, P., & Pérault-Pochat, M. C. (2020). Serious adverse effects occurring after chemotherapy: A general cancer registry-based incidence survey. British Journal of Clinical Pharmacology, 86(4), 711-722.
4. Greer, J. A., Amoyal, N., Nisotel, L., Fishbein, J. N., MacDonald, J., Stagl, J., Lennes, I., Temel, J. S., Safren, S., Pirl, W. F. A systematic review of adherence to oral antineoplastic therapies. The oncologist, 2016, 21(3), 354-376.
5. Vargason, A. M., Anselmo, A. C., Mitragotri, S. The evolution of commercial drug delivery technologies. Nature biomedical engineering, 2021, 5(9), 951-967.
6. Patra, J. K., Das, G., Fraceto, L. F., Campos, E. V. R., Rodriguez-Torres, M. D. P., Acosta-Torres, L. S., Diaz-Torres, L. A., Grillo, R., Swamy, M. K., Sharma, S., Habtemariam, S., Shin, H. S. Nano based drug delivery systems: recent developments and future prospects. Journal of nanobiotechnology, 2018, 16, 1-33.
7. Yao, Y., Zhou, Y., Liu, L., Xu, Y., Chen, Q., Wang, Y., Wu, S., Deng, Y., Zhasng, J., Shao, A. Nanoparticle-based drug delivery in cancer therapy and its role in overcoming drug resistance. Frontiers in molecular biosciences, 2020, 7, 193.
8. Kou, L., Bhutia, Y. D., Yao, Q., He, Z., Sun, J., & Ganapathy, V. Transporter-guided delivery of nanoparticles to improve drug permeation across cellular barriers and drug exposure to selective cell types. Frontiers in pharmacology, 2018, 9, 337630.
9. Fan, D., Cao, Y., Cao, M., Wang, Y., Cao, Y., Gong, T. Nanomedicine in cancer therapy. Signal Transduction and Targeted Therapy, 2023, 8(1), 293.
10. Pei, J., Yan, Y., Palanisamy, C. P., Jayaraman, S., Natarajan, P. M., Umapathy, V. R., Gopathy, S., Roy, J. R., Sadagopan, J. C., Thalamati, D., Mironescu, M. Materials-based drug delivery approaches: Recent advances and future perspectives. Green Processing and Synthesis, 2024, 13(1), 20230094.
11. Anselmo, A. C., & Mitragotri, S. Nanoparticles in the clinic: An update. Bioengineering & translational medicine, 2019, 4(3), e10143.
12. Sercombe, L., Veerati, T., Moheimani, F., Wu, S. Y., Sood, A. K., Hua, S. Advances and challenges of liposome assisted drug delivery. Frontiers in pharmacology, 2015, 6, 163819.
13. Kulkarni, J. A., Witzigmann, D., Thomson, S. B., Chen, S., Leavitt, B. R., Cullis, P. R., van der Meel, R. The current landscape of nucleic acid therapeutics. Nature nanotechnology, 2021, 16(6), 630-643.
14. Xu, L., Wang, X., Liu, Y., Yang, G., Falconer, R. J., Zhao, C. X. Lipid nanoparticles for drug delivery. Advanced NanoBiomed Research, 2022, 2(2), 2100109.
15. Beach, M. A., Nayanathara, U., Gao, Y., Zhang, C., Xiong, Y., Wang, Y., Such, G. K. Polymeric Nanoparticles for Drug Delivery. Chemical Reviews, 2024, 124(9), 5505-5616.
16. Grisolia, A., Dell'Olio, G., Spadafora, A., De Santo, M., Morelli, C., Leggio, A., Pasqua, L. Hybrid Polymer-Silica Nanostructured Materials for Environmental Remediation. Molecules, 2023, 28, 5105.

17. Lazzari, S., Moscatelli, D., Codari, F., Salmona, M., Morbidelli, M., Diomede, L. Colloidal stability of polymeric nanoparticles in biological fluids. Journal of nanoparticle research, 2012, 14, 1-10.
18. Kim, C. S., Tonga, G. Y., Solfiell, D., & Rotello, V. M. Inorganic nanosystems for therapeutic delivery: Status and prospects. Advanced drug delivery reviews, 2013, 65(1), 93-99.
19. Arias, L. S., Pessan, J. P., Vieira, A. P. M., Lima, T. M. T. D., Delbem, A. C. B., Monteiro, D. R. Iron oxide nanoparticles for biomedical applications: a perspective on synthesis, drugs, antimicrobial activity, and toxicity. Antibiotics, 72018, (2), 46.
20. Manshian, B. B., Jiménez, J., Himmelreich, U., Soenen, S. J. Personalized medicine and follow-up of therapeutic delivery through exploitation of quantum dot toxicity. Biomaterials, 2017, 127, 1-12.
21. Mazzotta, E., De Santo, M., Lombardo, D., Leggio, A., Pasqua, L. Mesoporous silicas in materials engineering: Nanodevices for bionanotechnologies. Materials Today Bio, 2022, 17, 100472.
22. Stephen, S., Gorain, B., Choudhury, H., Chatterjee, B. Exploring the role of mesoporous silica nanoparticle in the development of novel drug delivery systems. Drug delivery and translational research, 2022, 1-19.
23. Lin, C. Y., Yang, C. M., & Lindén, M. Dissolution and morphology evolution of mesoporous silica nanoparticles under biologically relevant conditions. Journal of Colloid and Interface Science, 2022, 608, 995-1004.
24. Lindén, M. Biodistribution and excretion of intravenously injected mesoporous silica nanoparticles: implications for drug delivery efficiency and safety. the enzymes, 2018, 43, 155-180.
25. Kresge, A. C., Leonowicz, M. E., Roth, W. J., Vartuli, J. C., Beck, J. S. Ordered mesoporous molecular sieves synthesized by a liquid-crystal template mechanism. Nature, 1992, 359(6397), 710-712.
26. Van Speybroeck, M., Barillaro, V., Do Thi, T., Mellaerts, R., Martens, J., Van Humbeeck, J., Vermant, J., Annnaert, P., den Mooter, G. V., Augustijns, P. Ordered mesoporous silica material SBA-15: a broad-spectrum formulation platform for poorly soluble drugs. Journal of pharmaceutical sciences, 2009, 98(8), 2648-2658.
27. Chen, C. Y., Li, H. X., Davis, M. E. Studies on mesoporous materials: I. Synthesis and characterization of MCM-41. Microporous materials, 1993, 2(1), 17-26.
28. Kim, T. W., Chung, P. W., Lin, V. S. Y. Facile synthesis of monodisperse spherical MCM-48 mesoporous silica nanoparticles with controlled particle size. Chemistry of Materials, 2010, 22(17), 5093-5104.
29. Øye, G., Sjöblom, J., Stöcker, M. Synthesis, characterization and potential applications of new materials in the mesoporous range. Advances in colloid and interface science, 2001, 89, 439-466.
30. Bagshaw, S. A., Prouzet, E., & Pinnavaia, T. J. Templating of mesoporous molecular sieves by nonionic polyethylene oxide surfactants. Science, 1995, 269(5228), 1242-1244.
31. Lin, H. Y., Chen, Y. W. Preparation of spherical hexagonal mesoporous silica. Journal of Porous Materials, 2005, 12, 95-105.
32. Stöber, W., Fink, A., & Bohn, E. Controlled growth of monodisperse silica spheres in the micron size range. Journal of colloid and interface science,1968, 26(1), 62-69.
33. Duan, L., Wang, C., Zhang, W., Ma, B., Deng, Y., Li, W., Zhao, D. Interfacial assembly and applications of functional mesoporous materials. Chemical reviews, 2021, 121(23), 14349-14429.

34. Wu, S. H., Mou, C. Y., Lin, H. P. Synthesis of mesoporous silica nanoparticles. Chemical Society Reviews, 2013, 42(9), 3862-3875.
35. Lee, C. H., Lin, T. S., Mou, C. Y. Mesoporous materials for encapsulating enzymes. Nano today, 2009, 4(2), 165-179.
36. Lang, N., Tuel, A. A fast and efficient ion-exchange procedure to remove surfactant molecules from MCM-41 materials. Chemistry of materials, 2004, 16(10), 1961-1966.
37. Lu, F., Wu, S. H., Hung, Y., Mou, C. Y. Size effect on cell uptake in well-suspended, uniform mesoporous silica nanoparticles. Small, 2009, 5(12), 1408-1413.
38. Dabbaghian, M. A., Babalou, A. A., Hadi, P., Jannatdoust, E. A parametric study of the synthesis of silica nanoparticles via sol-gel precipitation method. International Journal of Nanoscience and Nanotechnology, 2010, 6(2), 104-113.
39. Chiang, Y. D., Lian, H. Y., Leo, S. Y., Wang, S. G., Yamauchi, Y., Wu, K. C. W. Controlling particle size and structural properties of mesoporous silica nanoparticles using the Taguchi method. The Journal of Physical Chemistry C, 2011, 115(27), 13158-13165.
40. Vallet-Regi, M., Rámila, A., Del Real, R. P., Pérez-Pariente, J. A new property of MCM-41: drug delivery system. Chemistry of Materials, 2001, 13(2), 308-311.
41. Beck, J. S., Vartuli, J. C., Roth, W. J., Leonowicz, M. E., Kresge, C. T., Schmitt, K. D., Chu, C. T-W., Olson, D. H., Sheppard, E. W., McCullen, S. B., Higgins, J. B., Schlenker, J. L. A new family of mesoporous molecular sieves prepared with liquid crystal templates. Journal of the American Chemical Society, 1992, 114(27), 10834-10843.
42. Cai, Q., Luo, Z. S., Pang, W. Q., Fan, Y. W., Chen, X. H., & Cui, F. Z. Dilute solution routes to various controllable morphologies of MCM-41 silica with a basic medium. Chemistry of Materials, 2001, 13(2), 258-263.
43. Huang, R., Shen, Y. W., Guan, Y. Y., Jiang, Y. X., Wu, Y., Rahman, K., Luan, X. Mesoporous silica nanoparticles: Facile surface functionalization and versatile biomedical applications in oncology. Acta Biomaterialia, 2020, 116, 1-15.
44. Gao, P., Liang, Z., Zhao, Z., Wang, W., Yang, C., Hu, B., Cui, F. Enhanced adsorption of steroid estrogens by one-pot synthesized phenyl-modified mesoporous silica: Dependence on phenyl-organosilane precursors and pH condition. Chemosphere, 2019, 234, 438-449.
45. Putz, A. M., Almásy, L., Len, A., Ianăşi, C. Functionalized silica materials synthesized via co-condensation and post-grafting methods. Fullerenes, Nanotubes and Carbon Nanostructures, 2019, 27(4), 323-332.
46. Wang, G., Otuonye, A. N., Blair, E. A., Denton, K., Tao, Z., Asefa, T. Functionalized mesoporous materials for adsorption and release of different drug molecules: A comparative study. Journal of Solid State Chemistry, 2009, 182(7), 1649-1660.
47. Zhang, W., Zheng, N., Chen, L., Xie, L., Cui, M., Li, S., Xu, L. Effect of shape on mesoporous silica nanoparticles for oral delivery of indomethacin. Pharmaceutics, 2018, 11(1), 4.
48. Ritter, H., Nieminen, M., Karppinen, M., Brühwiler, D. A comparative study of the functionalization of mesoporous silica MCM-41 by deposition of 3-aminopropyltrimethoxysilane from toluene and from the vapor phase. Microporous and mesoporous materials, 2009, 121(1-3), 79-83.
49. Narum, S. M., Le, T., Le, D. P., Lee, J. C., Donahue, N. D., Yang, W., Wilhelm, S. Passive targeting in nanomedicine: fundamental concepts, body interactions, and clinical potential. In Nanoparticles for biomedical applications. Elsevier, 2020, 37-53.
50. Carmeliet, P., Jain, R. K. Principles and mechanisms of vessel normalization for cancer and other angiogenic diseases. Nature reviews Drug discovery, 2011, 10(6), 417-427.

51. Fromen, C. A., Rahhal, T. B., Robbins, G. R., Kai, M. P., Shen, T. W., Luft, J. C., DeSimone, J. M. Nanoparticle surface charge impacts distribution, uptake and lymph node trafficking by pulmonary antigen-presenting cells. Nanomedicine: Nanotechnology, Biology and Medicine, 2016, 12(3), 677-687.
52. Bertrand, N., Wu, J., Xu, X., Kamaly, N., Farokhzad, O. C. Cancer nanotechnology: the impact of passive and active targeting in the era of modern cancer biology. Advanced Drug Delivery Reviews, 2014, 66, 2-25.
53. Lin, Y. S., Lee, M. Y., Yang, C. H., Huang, K. S. Active targeted drug delivery for microbes using nano-carriers. Current topics in medicinal chemistry, 2015, 15(15), 1525-1531.
54. Tripathi, A. D., Labh, Y., Katiyar, S., Singh, A. K., Chaturvedi, V. K., Mishra, A. Folate-Mediated Targeting and Controlled Release: PLGA-Encapsulated Mesoporous Silica Nanoparticles Delivering Capecitabine to Pancreatic Tumor. ACS Applied Bio Materials, 2024.
55. Díaz-García, D., Fischer-Fodor, E., Vlad, C. I., Méndez-Arriaga, J. M., Prashar, S., Gómez-Ruiz, S. Study of cancer cell cytotoxicity, internalization and modulation of growth factors induced by transferrin-conjugated formulations of metallodrug-functionalized mesoporous silica nanoparticles. Microporous and Mesoporous Materials, 2021, 323, 111238.
56. Hou, L., Hou, Y., Liang, Y., Chen, B., Zhang, X., Wang, Y., Zhou, K., Zhong, T., Long, B., Wang, L., Han, X., Li, L., Xu, C., Gross, I., Gaiddon, C., Fu, W., Yao, H., Meng, X. Anti-tumor effects of P-LPK-CPT, a peptide-camptothecin conjugate, in colorectal cancer. Communications Biology, 2022, 5(1), 1248.
57. Lee, S. H., Park, O. K., Kim, J., Shin, K., Pack, C. G., Kim, K., Ko, G., Lee, N., Kwon, S-H., Hyeon, T. Deep tumor penetration of drug-loaded nanoparticles by click reaction-assisted immune cell targeting strategy. Journal of the American Chemical Society, 2019, 141(35), 13829-13840.
58. Zhang, J., Shang, J., Tang, X., Xu, X. TfR Aptamer-Functionalized MSNs for Enhancing Targeted Cellular Uptake and Therapy of Cancer Cells. ACS Omega, 2023, 8(51), 48975-48983.
59. Zhu, S., Gao, H., Li, W., He, X., Jiang, P., Xu, F., Jin, G., Guo, H. Stimuli-Responsive Aptamer-Drug Conjugates for Targeted Drug Delivery and Controlled Drug Release. Advanced Healthcare Materials, 2024, 2401020.
60. Ulbrich, K., Hola, K., Subr, V., Bakandritsos, A., Tucek, J., Zboril, R. Targeted drug delivery with polymers and magnetic nanoparticles: covalent and noncovalent approaches, release control, and clinical studies. Chemical Reviews, 2016, 116(9), 5338-5431.
61. Mi, P. Stimuli-responsive nanocarriers for drug delivery, tumor imaging, therapy and theranostics. Theranostics, 2020, 10(10), 4557.
62. Jia, R., Teng, L., Gao, L., Su, T., Fu, L., Qiu, Z., Bi, Y. Advances in multiple stimuli-responsive drug-delivery systems for cancer therapy. International journal of nanomedicine, 2021, 1525-1551.
63. Mura, S., Nicolas, J., Couvreur, P. Stimuli-responsive nanocarriers for drug delivery. Nature materials, 2013, 12(11), 991-1003.
64. Fu, D., Wang, Y., Xu, J., Wu, H. Hydrazone modified nanoscale metal-organic frameworks as pH responsive nanoplatforms for cancer therapy. Journal of Solid State Chemistry, 2022, 310, 123029.

65. Liao, S. C., Ting, C. W., Chiang, W. H. Functionalized polymeric nanogels with pH-sensitive benzoic-imine cross-linkages designed as vehicles for indocyanine green delivery. Journal of colloid and interface science, 2020, 561, 11-22.
66. Jin, Y., Song, L., Su, Y., Zhu, L., Pang, Y., Qiu, F., Tong, G., Yan, D., Zhu, B., Zhu, X. Oxime linkage: a robust tool for the design of pH-sensitive polymeric drug carriers. Biomacromolecules, 2011, 12(10), 3460-3468.
67. Luo, F., Fan, Z., Yin, W., Yang, L., Li, T., Zhong, L., Li, Y., Wang, S., Yan, J., Hou, Z., Zhang, Q. pH-responsive stearic acid-O-carboxymethyl chitosan assemblies as carriers delivering small molecular drug for chemotherapy. Materials Science and Engineering: C, 2019, 105, 110107.
68. Gannimani, R., Walvekar, P., Naidu, V. R., Aminabhavi, T. M., Govender, T. Acetal containing polymers as pH-responsive nano-drug delivery systems. Journal of controlled release, 2020, 328, 736-761.
69. Bruyère, H., Westwell, A. D., Jones, A. T. Tuning the pH sensitivities of orthoester based compounds for drug delivery applications by simple chemical modification. Bioorganic & Medicinal Chemistry Letters, 2010, 20(7), 2200-2203.
70. Li, Y., Wang, S., Song, F. X., Zhang, L., Yang, W., Wang, H. X., Chen, Q. L. A pH-sensitive drug delivery system based on folic acid-targeted HBP-modified mesoporous silica nanoparticles for cancer therapy. Colloids and Surfaces A: Physicochemical and Engineering Aspects, 2020, 590, 124470.
71. Kong, J., Park, S. S., & Ha, C. S. pH-sensitive polyacrylic acid-gated mesoporous silica nanocarrier incorporated with calcium ions for controlled drug release. Materials, 2022, 15(17), 5926.
72. Zhang, C., Xie, H., Zhang, Z., Wen, B., Cao, H., Bai, Y., Che, Q., Guo, J., Su, Z. Applications and biocompatibility of mesoporous silica nanocarriers in the field of medicine. Frontiers in pharmacology, 2022, 13, 829796.
73. Hao, N., Liu, H., Li, L., Chen, D., Li, L., Tang, F. In vitro degradation behavior of silica nanoparticles under physiological conditions. Journal of nanoscience and nanotechnology, 2012, 12(8), 6346-6354.
74. Li, X., Zhang, L., Dong, X., Liang, J., Shi, J. Preparation of mesoporous calcium doped silica spheres with narrow size dispersion and their drug loading and degradation behavior. Microporous and Mesoporous Materials, 2007, 102(1-3), 151-158.
75. Pohaku Mitchell, K. K., Liberman, A., Kummel, A. C., Trogler, W. C. Iron (III)-doped, silica nanoshells: a biodegradable form of silica. Journal of the American Chemical Society, 2012, 134(34), 13997-14003.
76. Cauda, V., Argyo, C., Bein, T. Impact of different PEGylation patterns on the long-term bio-stability of colloidal mesoporous silica nanoparticles. Journal of Materials Chemistry, 2010, 20(39), 8693-8699.
77. Choi, E., Kim, S. How can doxorubicin loading orchestrate in vitro degradation behaviors of mesoporous silica nanoparticles under a physiological condition? Langmuir, 2017, 33(20), 4974-4980.
78. Hong, X., Zhong, X., Du, G., Hou, Y., Zhang, Y., Zhang, Z., Gong, T., Sun, X. The pore size of mesoporous silica nanoparticles regulates their antigen delivery efficiency. Science advances, 2020, 6(25), eaaz4462.
79. He, Q., Zhang, Z., Gao, F., Li, Y., & Shi, J. In vivo biodistribution and urinary excretion of mesoporous silica nanoparticles: effects of particle size and PEGylation. Small, 2011, 7(2), 271-280.
80. Nabeshi, H., Yoshikawa, T., Arimori, A., Yoshida, T., Tochigi, S., Hirai, T., Akase, T., Nagano, K., Abe, Y., Kamada, H., Tsunoda, S., Itoh, N., Yoshioka, Y., Tsutsumi, Y. Effect

of surface properties of silica nanoparticles on their cytotoxicity and cellular distribution in murine macrophages. Nanoscale Research Letters, 2011, 6, 1-6.

81. Liu, T., Li, L., Teng, X., Huang, X., Liu, H., Chen, D., ren, J., Tang, F. Single and repeated dose toxicity of mesoporous hollow silica nanoparticles in intravenously exposed mice. Biomaterials, 2011, 32(6), 1657-1668.
82. Longmire, M., Choyke, P. L., Kobayashi, H. Clearance properties of nano-sized particles and molecules as imaging agents: considerations and caveats. Nanomedicine, 2008, 3(5), 703-717.
83. Niroumand, U., Firouzabadi, N., Goshtasbi, G., Hassani, B., Ghasemiyeh, P., Mohammadi-Samani, S. The effect of size, morphology and surface properties of mesoporous silica nanoparticles on pharmacokinetic aspects and potential toxicity concerns. Frontiers in Materials, 2023, 10, 1189463.
84. Frickenstein, A. N., Hagood, J. M., Britten, C. N., Abbott, B. S., McNally, M. W., Vopat, C. A., Patterson, E. G., MacCuaig, W. M., Jain, A., Walters, K. B., McNally, L. R. Mesoporous silica nanoparticles: Properties and strategies for enhancing clinical effect. Pharmaceutics, 2021, 13(4), 570.
85. Zhao, Z., Ukidve, A., Krishnan, V., & Mitragotri, S. Effect of physicochemical and surface properties on in vivo fate of drug nanocarriers. Advanced Drug Delivery Reviews, 2019, 143, 3-21.
86. Al-Ahmady, Z. S., Hadjidemetriou, M., Gubbins, J., Kostarelos, K. Formation of protein corona in vivo affects drug release from temperature-sensitive liposomes. Journal of controlled release, 2018, 276, 157-167.
87. Tan, Y., Yu, D., Feng, J., You, H., Bai, Y., He, J., Cao, H., Che, Q., Guo, J., Su, Z. Toxicity evaluation of silica nanoparticles for delivery applications. Drug Delivery and Translational Research, 2023, 13(9), 2213-2238.
88. Li, J., Shen, S., Kong, F., Jiang, T., Tang, C., Yin, C. Effects of pore size on in vitro and in vivo anticancer efficacies of mesoporous silica nanoparticles. RSC Advances, 2018, 8(43), 24633-24640.

Chapter 1

ENGINEERED MESOPOROUS SILICA-BASED NANOPARTICLES AS SMART CHEMOTHERAPY NANODEVICE FOR BORTEZOMIB ADMINISTRATION

M. De Santo, A. Giovinazzo, M. Fava, E. Mazzotta, I. E. De Napoli, M. Greco, A. Comandé, A. Nigro, P. Argurio, I. Perrotta, M. Davoli, A. Tagarelli, R. Elliani, T. Granato, G. Nicolini, A. Chiorazzi S. Semperboni, E. Ballarini, C. Crocamo, G. Cavaletti, D. Lombardo, D. Sisci, C. Morelli, A. Leggio and L. Pasqua

Published on: *Materials Chemistry Frontiers,* **2023**, 7, 216–229

DOI: 10.1039/D2QM01009G.

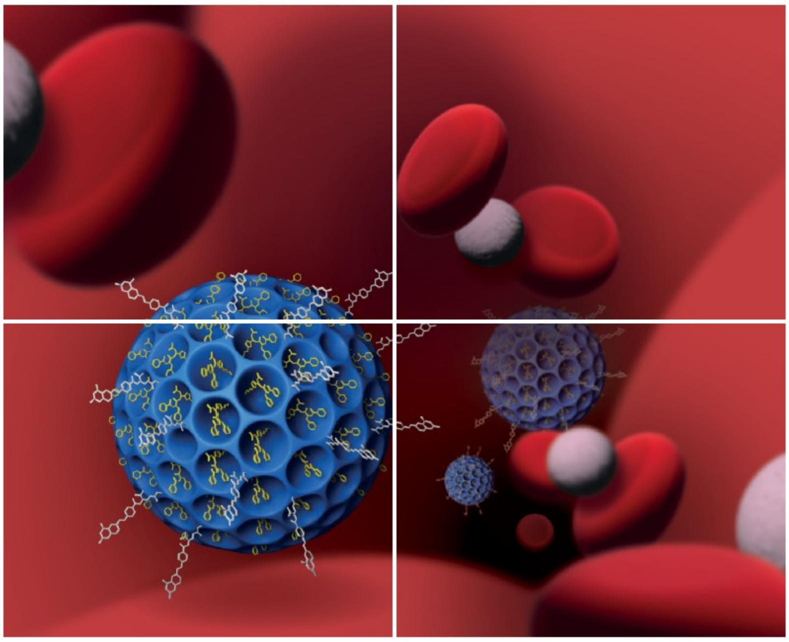

1.1 Introduction

Multiple myeloma (MM) is a hematologic malignancy characterized by abnormal proliferation of clonal plasma B cells in bone marrow, leading dysregulation of osteoblasts and activation of osteoclasts, and causing malignant bone lesions, kidney injury, anemia, infections, hypercalcemia, and pathological fractures [1]. It accounts for

1% of all cancers and 10% of all hematologic malignancies with a 5-year survival rate of approximately 60% [2-4]. Unlike normal plasma cells that produce immunoglobulins formed by a heavy and a light chain, malignant plasma cells secrete an excess of either intact immunoglobulins or free light chains of a single type, called monoclonal proteins (M-proteins) [5]. Therefore, the measurement of M-proteins could be useful for the diagnosis of MM, the monitoring of response to treatment, and detecting relapse [6, 7].

MM choice therapy depends on several parameters regarding patient age and health status. The approach to treatment is based on two factors: risk stratification and eligibility for stem cell transplantation [8]. Several drugs and numerous regimes involving these active drugs, have been shown activity in MM, and are accessible for clinical use. They include alkylating agent (melphalan, cyclophosphamide), corticosteroids (dexamethasone, lenalodomide, pomalidomide), and proteasome inhibitors (bortezomib, carfilzomib, ixazomib). Over the last twenty years, the immunomodulatory drugs (IMiDs) and proteasome inhibitors (PIs) significantly changed the therapeutic outcomes of MM patients [9, 10]. However, relapse and refractory dramatically occur. In order to address the unmet clinical requirement in MM therapies, new advanced agents have been introduced in the past decade [11]. Daratumumab and Isatuximab are two monoclonal antibodies targeting CD38, a transmembrane protein expressed at high level in malignant plasma cells [12, 13]. Next generation of PIs and IMiDs, as well as regimen with anti-CD38 antibodies, have been promoted. With new approval treatments, including B-cell mutation antigen (BCMA)-targeting antibody-drug conjugates, bispecific antibodies, and chimeric receptor T-cell (CAR-T) therapies, patient can achieve long-term remissions, but relapse appears [14, 15]. Richerdson *et al.* proposed a novel immunomodulatory drug and cereblon E3 ubiquitin ligase modulator, Mezigdomide, in combination with dexamethasone, showing potent anti-proliferative and immune-stimulatory effects in patients with relapsed or refractory MM. More recently, G protein-coupled receptor class C group 5 member D (GPRC5D) has emerged as a validated therapeutic target against MM, showing efficacy and manageable safety in early phase I that need to be confirmed in phase 3 trials [16].

Bortezomib (trade name Velcade) (Figure 1) is the first-in-class proteasome inhibitor approved by US FDA in 2005 for the treatment of MM patients who have relapsed following front-line therapy and are refractory to their most recent therapy, and successively in 2006, for the treatment of progressive MM in patients who have received at least one prior therapy and who have already undergone or are unsuitable for stem cell transplantation [17].

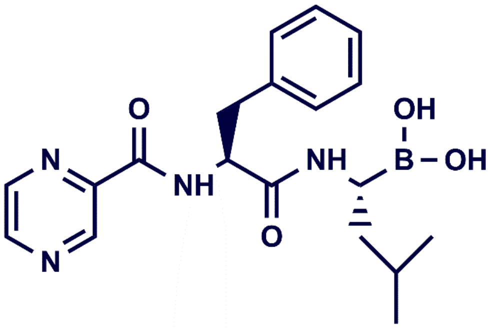

Figure 1. Chemical structure of BTZ.

Bortezomib (BTZ) acts in the ubiquitin-proteasome pathway of cellular protein homeostasis by inhibiting the activity of the proteasome 26S, consequently inducing the degradation of cellular proteins. Furthermore, BTZ rapidly stimulates osteoblast proliferation and differentiation *in vitro*, increasing bone matrix deposition [18]. Despite BTZ efficacy, resistance and relapse appear inevitable [19, 20].

The major adverse reactions induced by BTZ include thrombocytopenia, fatigue, neutropenia, and neuropathy [21]. Peripheral Neuropathy (PN) represents the most severe, intractable, and regimen-limiting non-hematological complication that occurs during BTZ-based therapy, with no recommended treatment to prevent or treating it [22]. Although the next generation of proteosome inhibitors (carfilzomib and ixazomib) shows less toxicity, their clinical efficacy and impact on the incidence of peripheral neuropathy (PN) still require confirmation [23].

Despite the significant progress in expanding treatment options and improving patient survival, MM remains treatable but generally not curable. The main limitation of chemotherapeutics in MM is their severe side effects, which affect the drugs' pharmacokinetics, safety, and efficacy. Traditional chemotherapy lacks specificity, has poor absorption and bioavailability, and causes systemic toxicity and adverse reactions. Nanoparticle-based drug delivery systems address these limitations by specifically targeting cancer cells, controlling drug release through specific triggers, and enhancing the safety and efficacy of treatments.

Advances in nanotechnology mark a new era in MM treatment, with recent nano-based strategies offering promising improvements.

Anderson *et al.* [24] encapsulated BTZ in FDA-approved biodegradable and biocompatible polymer PEG-PLGA nanoparticles, conjugating the anti-BCMA antibody on the external surface as targeting moiety. Their proposed nanodevice showed target-specific cytotoxicity against MM cell lines and primary tumor cells from MM patients. Furthermore, BTZ-based nanotherapy induced cell death more efficiently than non-targeted nanoparticles or free BTZ. In a murine xenograft model, it showed enhanced tumor reduction and prolonged host survival.

The Tiron-based liposomal BTZ formulation developed by Lee and coworkers demonstrated potent cytotoxicity *in vivo* and antitumor efficacy *in vivo*, prolonging plasma circulation time and retention compared to free BTZ. The findings reveal the promising therapeutic potential of the BTZ-based liposomal complex for patients who are resistant to currently available BTZ treatments [25].

A system for BTZ delivery was successfully fabricated by Su. and his team using hallow mesoporous silica nanospheres (HMSNs). Final BTZ@HMSN device limited cell proliferation and augmented apoptosis in lymphoma SNK-1 cells compared to free drug. In vivo investigations demonstrated significant reduction of tumor volume and weight if compared to conventional BTZ administration. Hence, nano-based therapy showed improved tumor-suppressing effect *in vitro* and *in vivo* [26].

A new system for administering BTZ (FOL-MSN-BTZ) based on mesoporous silica nanoparticles (MSNs) has been developed using the patented MSN technology of NanoSiliCal Devices, an innovative SME and spin-off from the University of Calabria, where I completed an 18-month internship during my doctoral studies.

The FOL-MSN-BTZ prototype was designed with the aim of improving the performance of conventional BTZ-based chemotherapies, increasing tumor selectivity, and reducing drug diffusion and deposit in healthy tissues.

This engineered MSU-type nanodevice, FOL-MSN-BTZ, selectively delivers BTZ to folate receptor-overexpressing multiple myeloma (FR+ MM) cells, ensuring controlled drug release. Folic acid (FOL), grafted on the external surface of the MSN, acts as a receptor-specific ligand, enabling tumor recognition and cell internalization. BTZ, linked to the internal pore surface through a covalent pH-sensitive bond, is released in the acidic tumor environment.

The choice of using folic acid as a targeting function comes from the well-documented evidence that the folate receptor is highly expressed in tumor cells, including MM cells, compared with normal cells. Moreover, folic acid has been largely acknowledged as an effective targeting function to be exploited in drug-delivery nanosystems.

An extensive optimization process for the device, focusing on drug release at different pH levels and toxicity to healthy cells, supported by a preliminary *in vitro* study [27], yielded a prototype with remarkable selectivity for FR+ cancer cells and no toxicity to FR- healthy cells.

A thorough analysis of the suspensions identified the optimal formulation for administration to myeloma-bearing mice. The *in vivo* results demonstrated improved therapeutic efficacy, reduced bortezomib toxicity when delivered via the nanodevices.

1.2 Synthesis and optimization of MSN-based nanodevice for the smart administration of Bortezomib

1.2.1 Results and Discussions

FOL-MSN-BTZ prototype consists of a targeting ligand, folic acid (FOL), covalently bonded, via an amide bond, to an aminopropyl group preferentially linked to the external surface of the nanoparticles, while bortezomib (BTZ) forms, with a diol linker mainly anchored to the internal pore silica surfaces, a pH sensitive cyclic boronate ester (Figure 2).

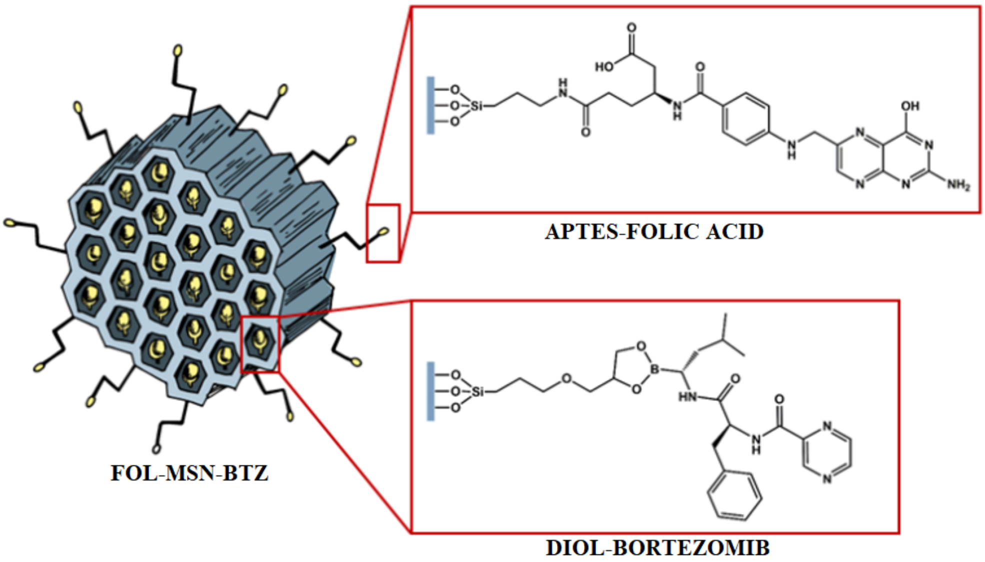

Figure 2. Graphical representation of FOL-MSN-BTZ structure.

A multistep procedure was employed to prepare FOL-MSN-BTZ prototype. This strategy involves the synthesis of the starting MSNs, the external functionalization for conjugating folic acid, surfactant removal from the inner pores of the MSNs, and subsequent modification of the inner pore surface to anchor BTZ via a pH-responsive bond.

The starting MSU-type mesoporous silica nanoparticles were obtained through a not-catalyzed biphasic synthetic procedure [28], following a modified synthetic protocol claimed in an international patent. Mesoporous silica nanoparticles were synthesized at room temperature, using cyclohexane as organic phase in which the silica source, tetraethyl orthosilicate (TEOS), was dissolved. Hydrolysis of TEOS occurred in presence of a neutral, low-cost, non-toxic, and biodegradable surfactant (Triton X-100) acting as structure-directing agent. So, silica condensed around surfactant micelles, assembling in an inorganic oxide framework.

The as-synthesized materials were functionalized before solvent extraction of the surfactant thus protecting the internal silica surface of the pores and, at the same time, preferentially addressing the modifying agent on the external surface of the mesoporous particles. According to this specific synthetic protocol a considerable pore volume was recovered after the surfactant extraction from the PEG-templated folic acid-functionalized hybrid mesoporous silica.

The obtained MSNs were then converted in aminopropyl-functionalized nanoparticles (AP-MSN) by covalent grafting of (3-aminopropyl)triethoxyxilane (APTES) on the MSN surface (Scheme 1). Then, folic acid-functionalized nanoparticles (FOL-MSN) were obtained by forming an amide bond between the amino group of AP-MSN and the carboxylic function of FOL (Scheme 1).

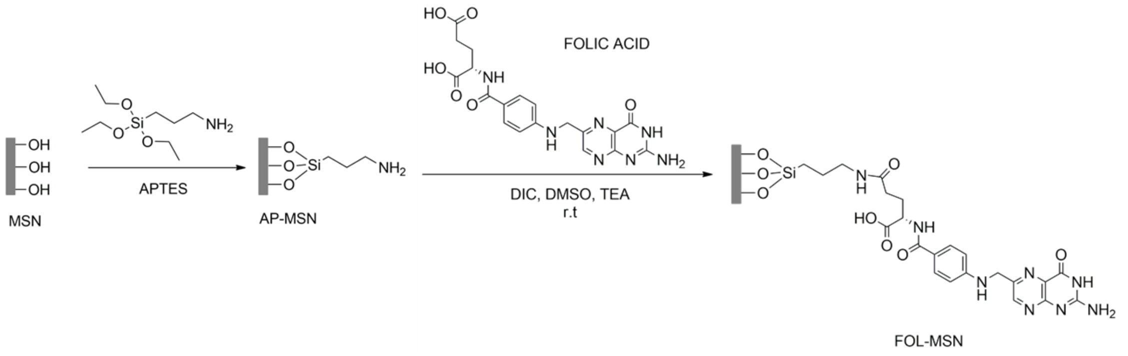

Scheme 1. Schematic representation of FOL conjugation to the external surface of surfactant – bearing MSNs.

After removing the surfactant with ultrapure water at room temperature, the inner pores of the extracted FOL-MSN (FOL-MSN-EXT) were functionalized with 3-glycidoxypropyltrimethoxysilane. Following hydrolysis, a DIOL ligand was formed (Scheme 2). This DIOL ligand is used to anchor BTZ to the nanoparticles by forming a pH-sensitive boronate ester between the diol groups of FOL-MSN and the boronic acid group of BTZ (Scheme 3).

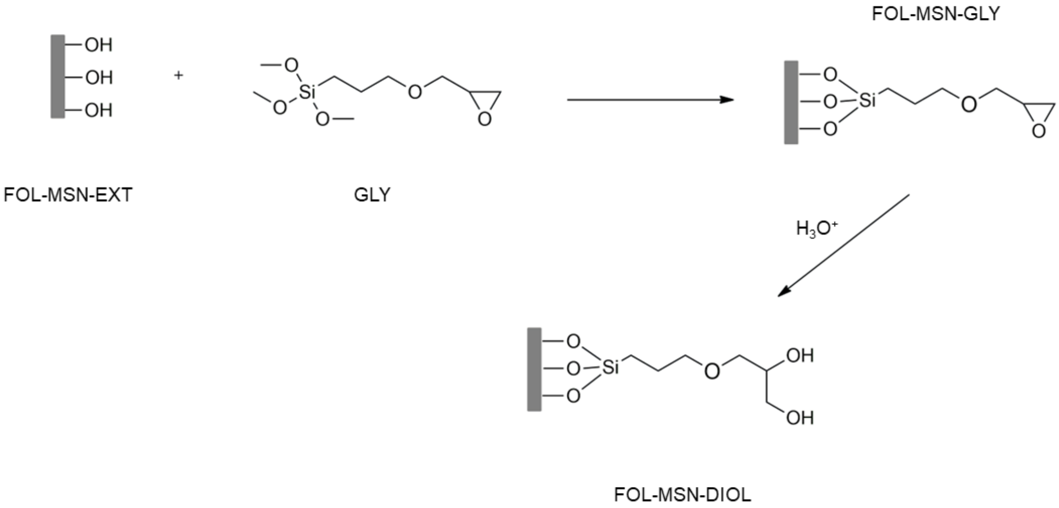

Scheme 2. Synthesis of FOL-MSN-DIOL.

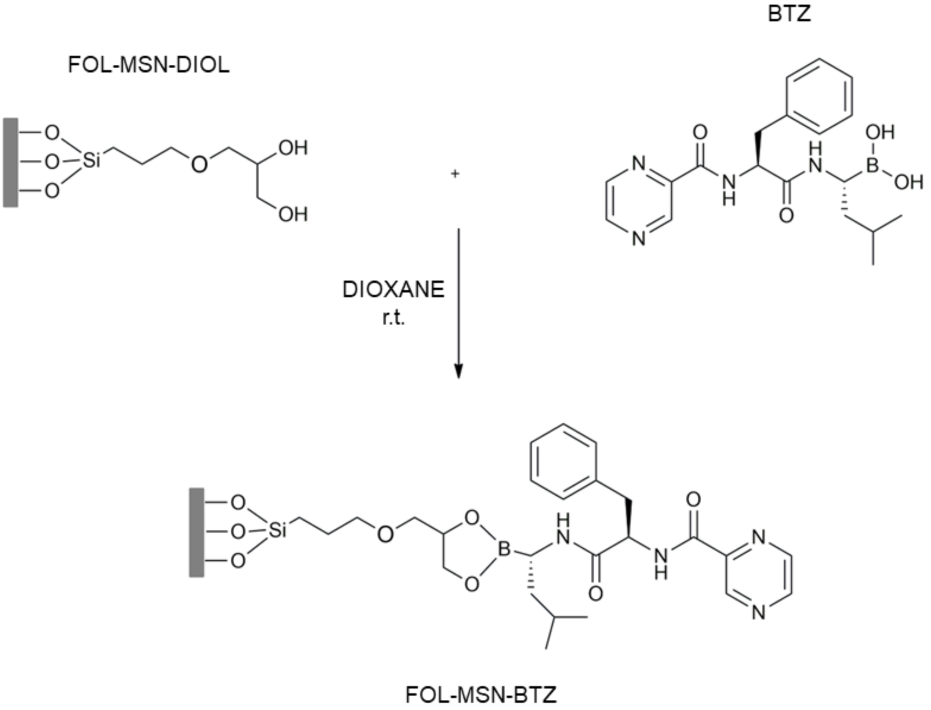

Scheme 3. Synthesis of FOL-MSN-BTZ.

The amount of BTZ (10.38%) in FOL-MSN-BTZ sample was determined by analyzing the boron content by Atomic Absorption Spectroscopy.

Solid-state ^{29}Si and ^{13}C NMR analysis of FOL-MSN-BTZ confirmed the conjugation of the organic ligands and BTZ to the silica nanostructure.

To enhance the efficacy and safety of FOL-MSN-BTZ, an accurate optimization process was carried out on the prototype. The experiments were addressed to increase the folic acid concentration on the external surface of MSNs: the higher concentration of FOL prevents the BTZ prodrug from positioning on the MSN's external surface. Additionally, a higher folic acid concentration could enhance the nanocarrier's specificity for cellular uptake via folate receptor-mediated endocytosis. The optimal prototype should be non-toxic to healthy cells and exhibit negligible BTZ release at physiological pH.

The drug release profiles of mesoporous silica nanoparticles (MSNs) functionalized with low (LF), medium (MF), and high (HF) folic acid content were studied using HPLC analysis across different pH values to assess their pH-sensitive performance. The LF, MF, and HF prototypes were incubated in phosphate (pH 7) and acetate (pH 5) buffers, to mimic physiological and acidic endolysosomal conditions, respectively. Additionally, drug release was analyzed at a highly acidic pH of 1.5. In vitro tests were also conducted to evaluate the toxicity of the three samples on BJhTERT normal cells.

The sample with the lowest folic acid content, LF-MSN-BTZ, exhibited significant *in vitro* toxicity on BJhTERT healthy cells (Figure 3), which was associated with undesirable BTZ release at pH 7 (Figure 4A). The MF-MSN-BTZ sample showed improved performance in terms of reduced toxicity and BTZ release (Figure 3 and Figure 4B). The HF-MSN-BTZ sample demonstrated the best performance, showing minimal toxicity to normal cells, negligible BTZ release (0.06%) at physiological pH, and over 90% drug release at pH 5 (Figures 3 and 4C).

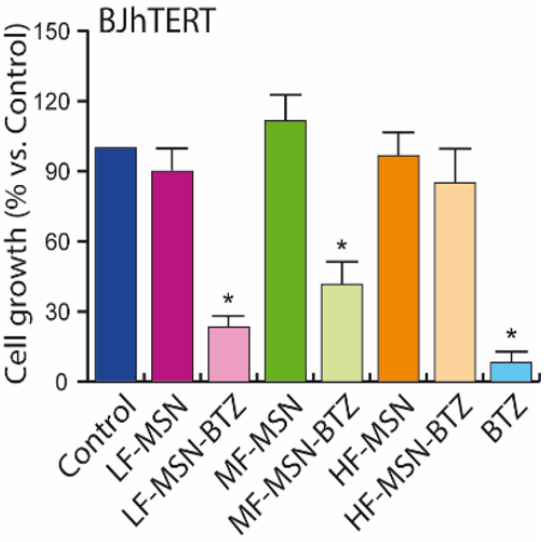

Figure 3. Toxicity evaluation of LF, MF, and HF samples on normal BJhTERT cells. Free BTZ was used as positive control. Viability was determined after 3 days. Statistical analysis was performed using One-way ANOVA and data were reports as the mean ± SD of 3 independent experiments, each performed in triplicates (* $p < 0.05$).

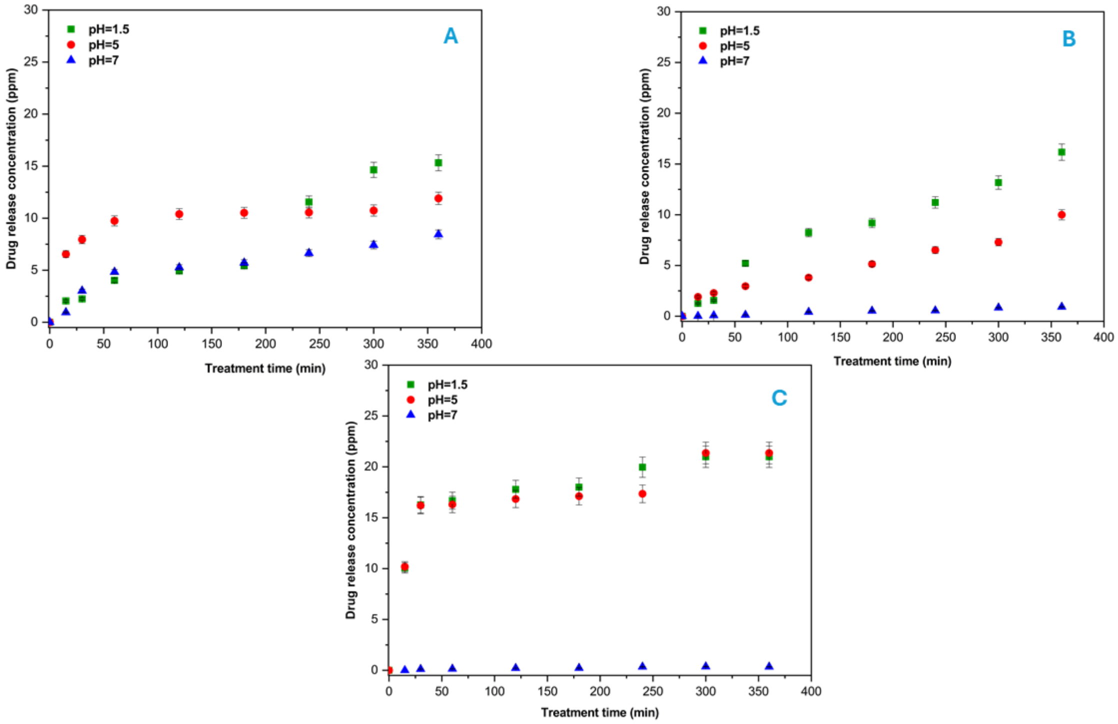

Figure 4. Bortezomib release as function of time at different pH values from LF- (A), MF- (B), and HF- (C) compositions of FOL-MSN-BTZ.

These results confirm that increasing the folic acid content on the external surface of mesoporous silica nanoparticles creates a continuous folic acid coating, which prevents the BTZ prodrug from attaching to the surface. The observed toxicity in lower folic acid MSN compositions may be attributed to the BTZ prodrug being grafted onto the external surface, making it less protected and more prone to hydrolysis. This is likely due to the catalytic role of the silica surface, which can accelerate the cleavage of the bond between BTZ and the nanoparticles by water molecules, even at neutral pH.

Energy dispersive X-ray analysis (EDAX) conducted on the surfaces of LF, MF, and HF samples supports these assumptions. In Figure 5, the red and green points indicate the presence of boron (B) and silicon (Si), respectively. As the folic acid concentration increased from low to high, the Si (green points) became more prominent while the B (red points) decreased. The HF-MSN-BTZ sample showed the lowest B/Si ratio, indicating a reduction in the BTZ prodrug content on the nanoparticle surfaces. This increase in folic acid concentration correlates with a significant reduction in drug release at neutral pH and decreased toxicity to healthy cells.

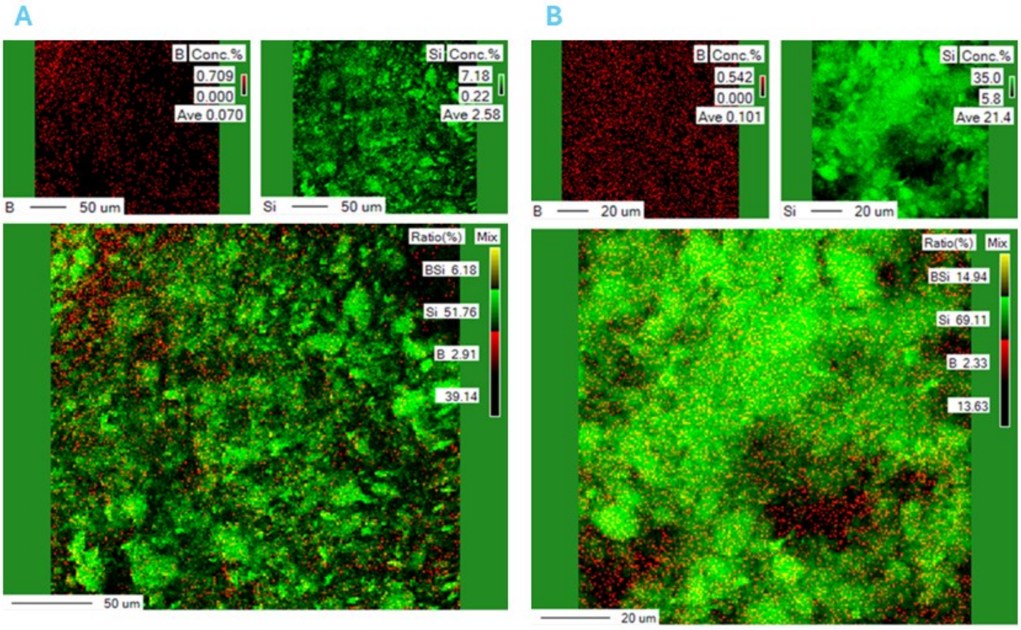

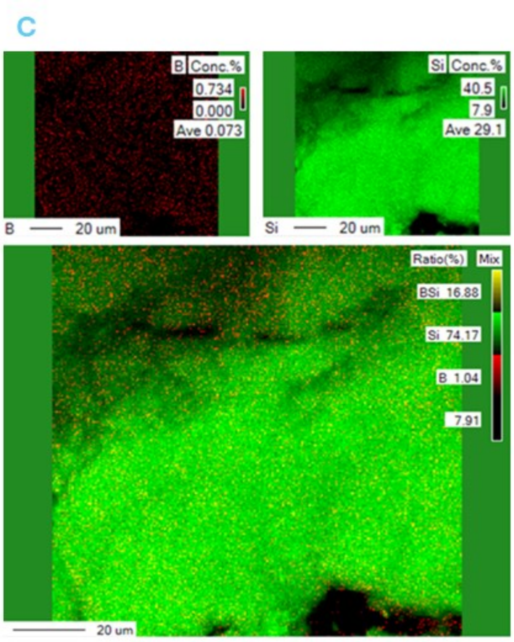

Figure 5. Polychromatic maps of Si and B contents in LF- (A), MF- (B), and HF- (C) samples surfaces.

Table 1 summarized the quantitative evaluation of silicon (Si) and boron (B) compositions on surface of the three analysed samples.

Sample	B [wt %]	Si [wt %]	B/Si ratio
LF-MSN-BTZ	0.070	2.58	**0.0271**
MF-MSN-BTZ	0.101	21.40	**0.0047**
HF-MSN-BTZ	0.073	29.10	**0.0025**

Table 1. Quantitative evaluation of silicon (Si) and boron (B) compositions, and B/Si ratio on surface of the three analysed samples.

Consequently, the optimized prototype HF-MSN-BTZ is now simply referred to as FOL-MSN-BTZ.

Transmission electron microscopy (TEM) images (Figure 6) reveal that both samples, MSN (Figure 6A) and FOL-MSN-BTZ (Figure 6B), display a mesoporous texture characteristic of materials of the MSU family, with primary dimensions of 80-120 nm.

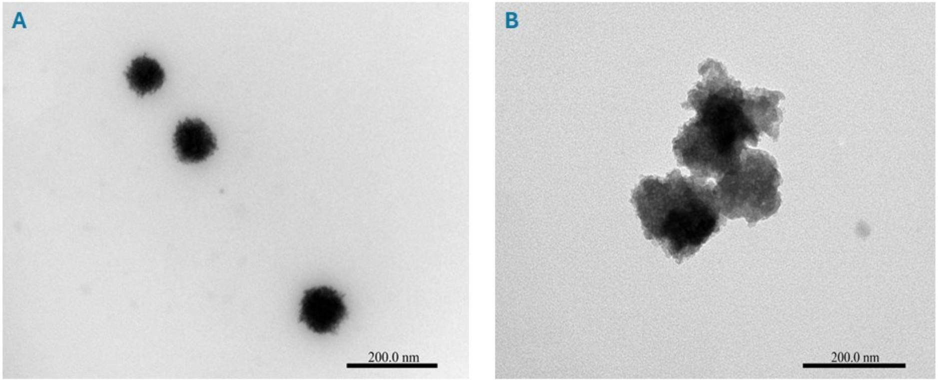

Figure 6. TEM images of starting MSNs (A) and FOL-MSN-BTZ (B) samples.

Scanning electron microscopy (SEM) images demonstrated that the synthesis and subsequent modification processes produced nanoscale particles. These particles lack a regular morphology and often form aggregates up to 300 nm in size (Figure 7A and 7B).

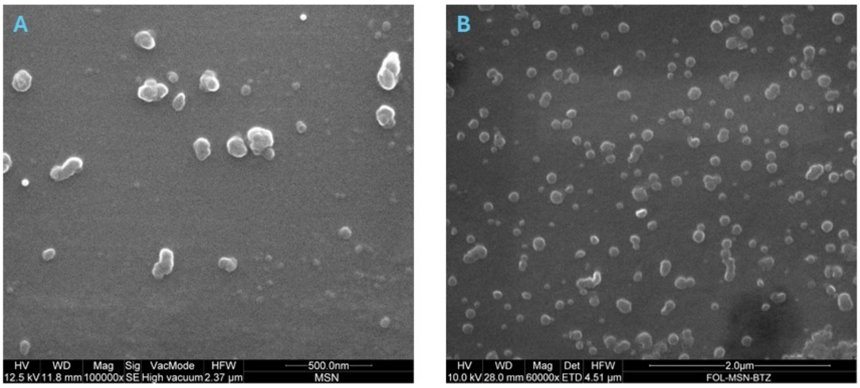

Figure 7. SEM images of starting MSNs (A) and FOL-MSN-BTZ (B) samples.

The XRD patterns of FOL-MSN, FOL-MSN-EXT, and FOL-MSN-BTZ nanoparticles (Figure 8) displayed a single broad diffraction peak. This indicates a lack of long-range crystallographic order, which is consistent with the characteristics observed in MSU materials [29].

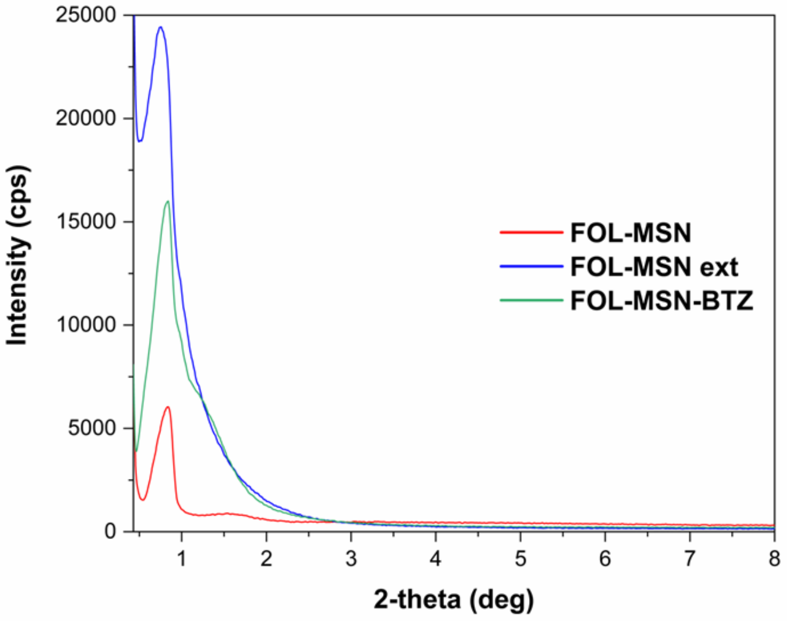

Figure 8. XRD power diffraction patterns of FOL-MSN, FOL-MSN-EXT and FOL-MSN-BTZ samples.

Furthermore, the nitrogen adsorption/desorption isotherms of all tested MSNs samples (Figure 9) exhibited IV type pattern.

FOL-MSN-EXT possessed higher pore volume and BET surface area resulting from the removal of surfactant from the inner pores of the MSN (Table 2). In contrast, FOL-MSN and FOL-MSN-BTZ exhibited similar BET surface area and pore volume values, due to the filling of the pores with surfactant and BTZ prodrug, respectively (Table 2).

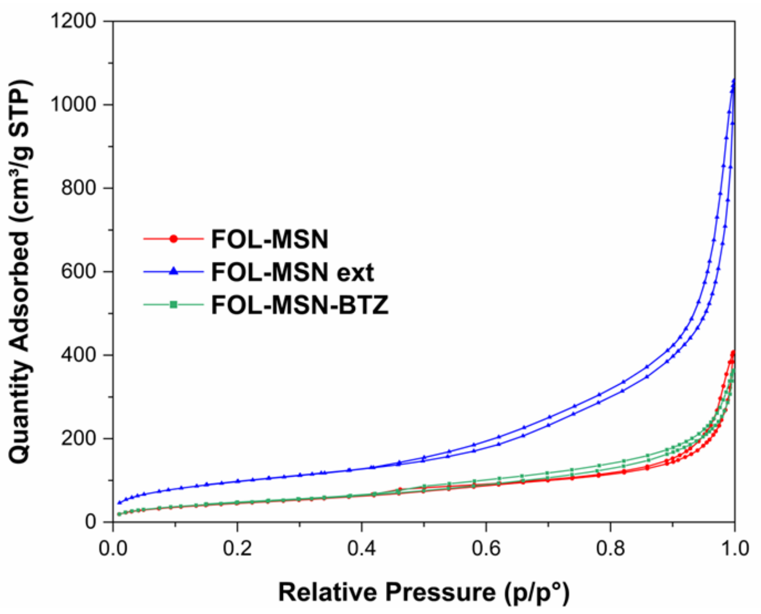

Figure 9. Nitrogen adsorption isotherms of FOL-MSN (red), FOL-MSN-EXT (blue), and FOL-MSN-BTZ (green).

Sample	BET Surface area [m^2/g]	Pore volume [cm^3/g]
FOL-MSN	170	0.30
FOL-MSN-EXT	377	0.88
FOL-MSN-BTZ	176	0.33

Table 2. BET surface area and pore volume values at $P/P^0 = 0.96$.

Zeta potential measurements of the MSN starting materials confirmed a negatively charged surface, around -30 mV, due to the presence of silanol groups. Notably, FOL-MSN-BTZ showed a positive zeta potential of +18 mV. This inversion to a positive value indicates successful functionalization of the nanoparticles' surface.

The effect of MSNs on cell proliferation was evaluated on FR- normal cell lines, BJhTERT and 3T3L-1, and on FR+ multiple myeloma (MM) cell lines, including RPMI, and U266B1, being BTZ the treatment of choice for this type of cancer. Interestingly, FOL-MSN-BTZ induced death or inhibited proliferation in all FR+ MM cells (Figure 9A and 9B) but not in FR- normal cells (Figure 9C and 9D). In contrast, BTZ resulted toxic for all tested cell lines (Figure 9). Moreover, *in vitro* tests showed that the vehicle alone, FOL-MSN, was safe for both normal and tumor cells (Figure 9).

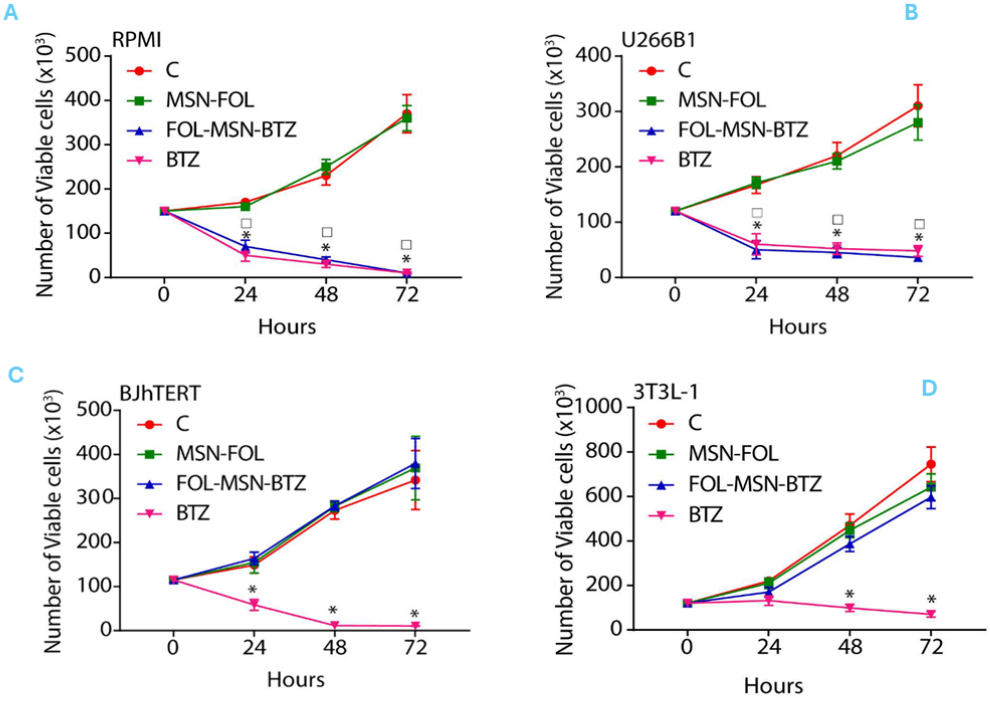

Figure 9. Cells were treated for 1h with FOL-MSN-BTZ or left untreated (C=control). MSN-FOL (vehicle alone) were used as negative control and the free drug (BTZ) as positive control. Cell viability was after 24, 48 and 72 h. Statistical analysis was performed using One-way ANOVA and the values represent the mean ± SD of 3 different triplicates experiments. * $p \leq 0.01$ BTZ vs untreated; * $p \leq 0.01$ FOL-MSN-BTZ vs untreated.

TEM observation on RPMI and BJhTERT cells treated with FOL-MSN-BTZ demonstrated that the uptake of MSNs occurred only in FR+ RPMI (Figure 10, upper panel) and not in FR- BJhTERT cells (Figure 10, lower panel), where they remained confined in the intercellular spaces.

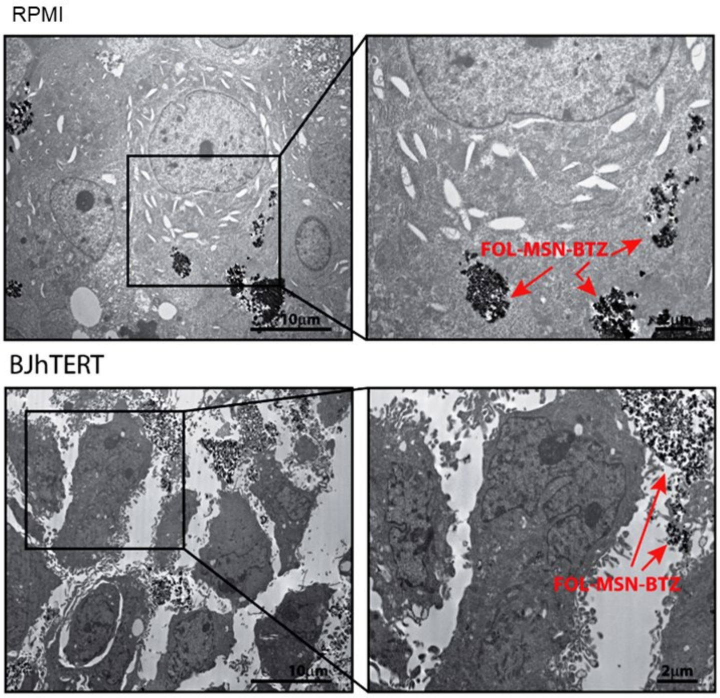

Figure 10. TEM investigation on cancerous RPMI and normal BJhTERT cells after 1 h treatment with FOL-MSN-BTZ.

Immunogold labelling experiments on RPMI confirmed that FOL-MSN-BTZ uptake occurred through FR-mediated endocytosis, showing FR recognition at the cell membrane on the left panel and sequestration in FR-immunopositive intracellular vesicles on the right panel (Figure 11).

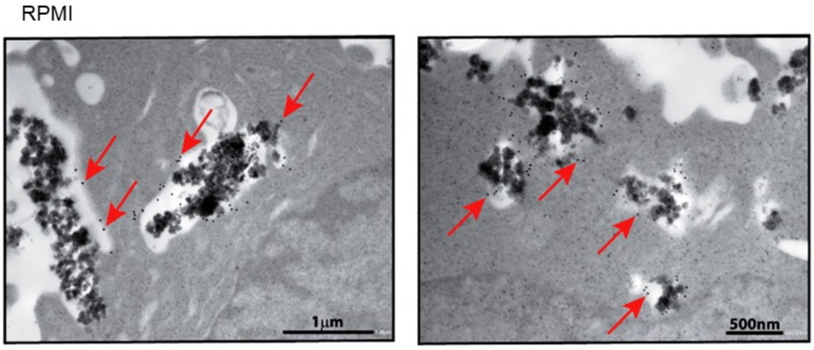

Figure 11. Colloidal-gold immunocytochemistry for FR-β (black dots indicated by arrows) in RPMI cells exposed to FOL-MSN-BTZ for 1 h.

For conducting *in vivo* investigations, it is crucial to consider the sedimentation behavior and stability of suspended nanoparticles in media. Nanoparticles dispersed in solution can sediment, diffuse, and aggregate based on their intrinsic properties and system characteristics. As a result, the concentration of drug-loaded nanoparticles in the suspension may decrease, altering the concentration of the loaded drug. To develop an effective *in vivo* administration protocol, the performance of three FOL-MSN-BTZ suspensions (FOL-MSN-BTZ1, FOL-MSN-BTZ2, FOL-MSN-BTZ3) was thoroughly studied. Known concentrations of these suspensions were stirred for 13 minutes. The supernatant from the upper half volume of each suspension was then immediately collected and analyzed for BTZ content using atomic absorption spectroscopy. The drug content in the liquid upper phase was found to be 65.9% ± 5.8% of the expected dose of suspended FOL-MSN-BTZ (Table 3).

Sample	BTZ sample/BTZ tot Measured [%]	BTZ sample/BTZ tot Theorical [%]	Sample recovery [%]
FOL-MSN-BTZ$_1$	32.2	50	64.4
FOL-MSN-BTZ$_2$	36.8	50	73.6
FOL-MSN-BTZ$_3$	29.9	50	59.8
Average	22.9	-	65.9
Standard deviation	3.5	-	5.8

Table 3. Evaluation of effective BTZ content in analyzed FOL-MSN-BTZ suspensions.

The No Observed Adverse Effect Level (NOAEL) study was initially conducted to determine the most effective dose of BTZ-loaded nanodevices for *in vivo* efficacy tests. Notably, animals well tolerated a double dose of BTZ (2 mg/kg, referred to the amount of BTZ bearing by MSNs, named BTZ EQ) when delivered via the MSN platform, compared to the free drug administration, for which the maximum tolerated dose is 1 mg/kg. This indicates a significant improvement in therapeutic efficacy with the developed nanodevice. Additionally, the vehicle alone, FOL-MSN, demonstrated good tolerability at all tested doses during the treatment period.

After identifying FOL-MSN-BTZ at 2 mg/kg (BTZ EQ) as the highest tolerated dose with no observed adverse events, we evaluated the efficacy of this nanodevice using an *in vivo* subcutaneous tumor model with female SCID mice implanted with RPMI 8226 cells. According to the *in vivo* RPMI 8226 human MM cell-derived xenograft mice model, mice were treated once a week for 5 weeks with FOL-MSN-BTZ 2 mg/kg (BTZ EQ), FOL-MSN 2 mg/kg (BTZ EQ), and BTZ 1 mg/kg as the reference drug [30].

All animals well tolerated the MSN-based treatment, since no significant body weight loss was observed throughout the experiment. In contrast, mice treated with free BTZ showed a significant reduction in body weight comparing either to untreated no-tumor and tumor-bearing groups (Figure 12).

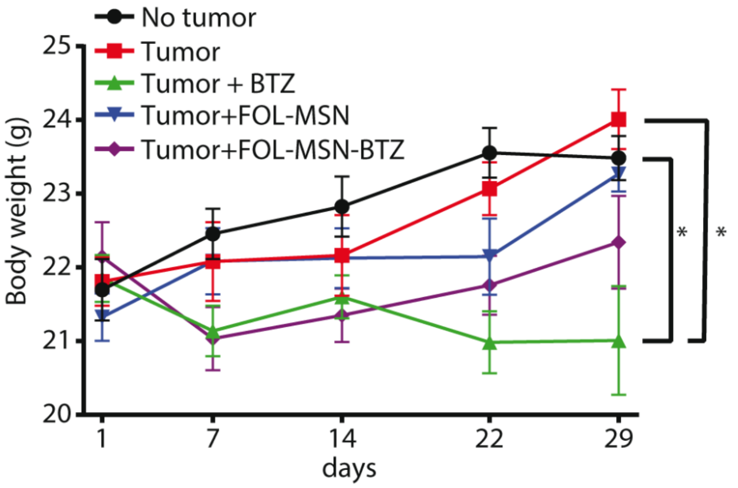

Figure 12. Body weight gains in mice throughout the treatment period. The results are expressed as mean ± SD and were statistically analyzed using the analysis of variance (ANOVA) and the Tukey–Kramer post-test (*p < 0.05).

Mice treated with free BTZ exhibited only a slight increase in tumor volume throughout the experiment, confirming the drug's anti-neoplastic effect (Figure 12). Notably, FOL-MSN-BTZ was able to completely stop the tumor growth immediately after the first administration and during the treatment period (Figure 12). These findings clearly demonstrate the superior efficacy of our delivery system compared to free BTZ.

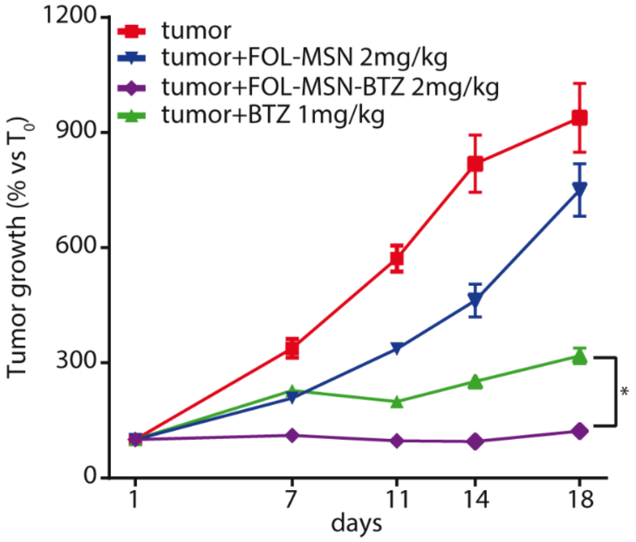

Figure 13. Percentage of increase (ratio between the tumor volume at each time point and the tumor volume at time 0) of tumor mass for each group. The results are expressed as mean ± SD and were statistically analyzed using the analysis of variance (ANOVA) and the Tukey–Kramer post-test (*p < 0.05).

Survival analysis indicated a dramatic mortality rate in untreated animals as compared to treated animals, especially considering FOL-MSN-BTZ (Figure 14).

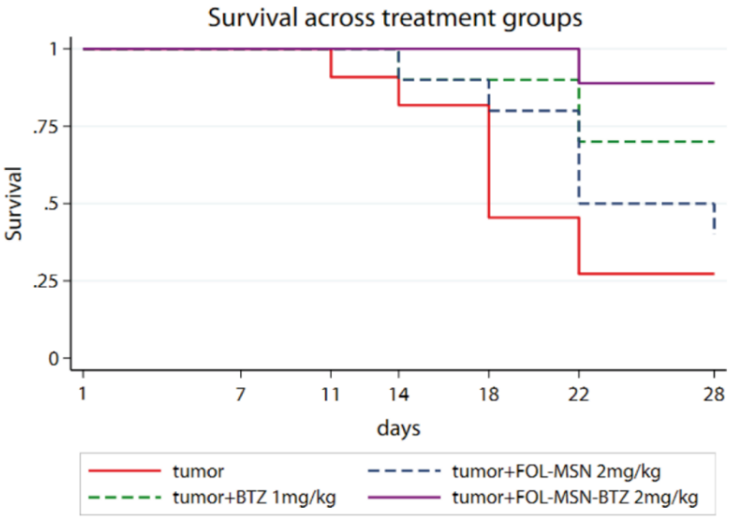

Figure 14. Kaplan–Meier curves for survival analysis according to different treatment groups. The results are expressed as mean ± SD and were statistically analyzed using the analysis of variance (ANOVA) and the Tukey–Kramer post-test (*$p < 0.05$).

Biodistribution analyses were performed using ICP-MS to measure boron from BTZ and silicon from MSNs in organs explanted from different groups of mice 48 h after the last administration.

FOL-MSN-BTZ showed a slightly higher accumulation in tumor tissue compared to free BTZ (Figure 15), which correlates with the enhanced *in vivo* antitumor efficacy of the nanosystem, very likely due to its targeting capacity. Noteworthy, FOL-MSN-BTZ showed lower distribution in the lungs than free BTZ (Figure 14), potentially reducing the risk of pulmonary toxicity.

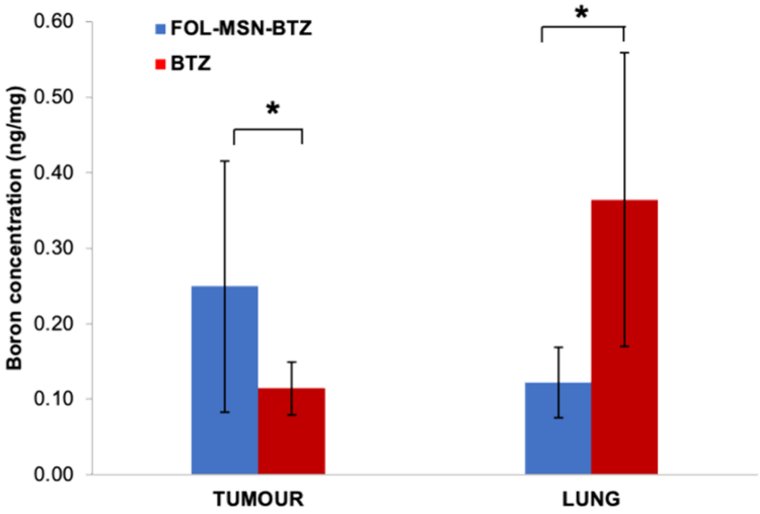

Figure 15. Comparison of Boron amounts in tumor and lung tissues of mice treated with FOL-MSN-BTZ and free BTZ, statistically analyzed using the non-parametric Mann-Whitney U test (* p<0.05).

A higher silicon accumulation was detected in the liver tissues of mice treated with FOL-MSN-BTZ compared to same tissues of mice treated with free BTZ (Figure 16) probably due to the role of liver as the primary organ for nanoparticle detoxification. In the kidneys (Figure 16), FOL-MSN-BTZ did not alter the natural silicon biodistribution [31].

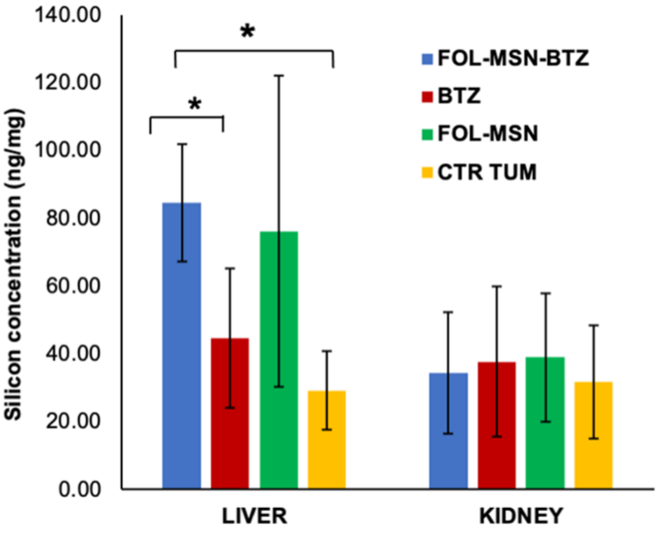

Figure 16. Comparison of silicon amounts in liver and kidney tissues of mice untreated (CTR TUM) and treated with FOL-MSN-BTZ, FOL-MSN, and free BTZ, statistically analyzed using the non-parametric Kruskal-Wallis test (* p<0.05).

Data on silicon and boron contents in tissues such as spleen, sternum, bladder, uterus, heart, and have not been reported since no statistical analysis could be conducted due to the very low or even undetectable levels of Si and B found. The silicon detected in the tissues of untreated mice (CTR TUM) and those treated with free BTZ corresponds to the natural presence of this element in various organs, as reported in the literature [31].

Finally, the experimental stability of FOL-MSN-BTZ and FOL-MSN suspensions (2 mg/kg BTZ EQ) in a physiological medium, was evaluated by Turbiscan analyzer, reproducing the *in vivo* administration conditions. The Turbiscan Stability Index (TSI) was used as the reference for quantifying stability: the lower the TSI, the more stable is the sample. Although a trend of decreasing stability over the time was observed (Figure 17 A), a TSI value of less than 4 was maintained for each sample during the first 10 minutes, ensuring proper administration of the studied doses (Figure 17 B, 17C, and 17D).

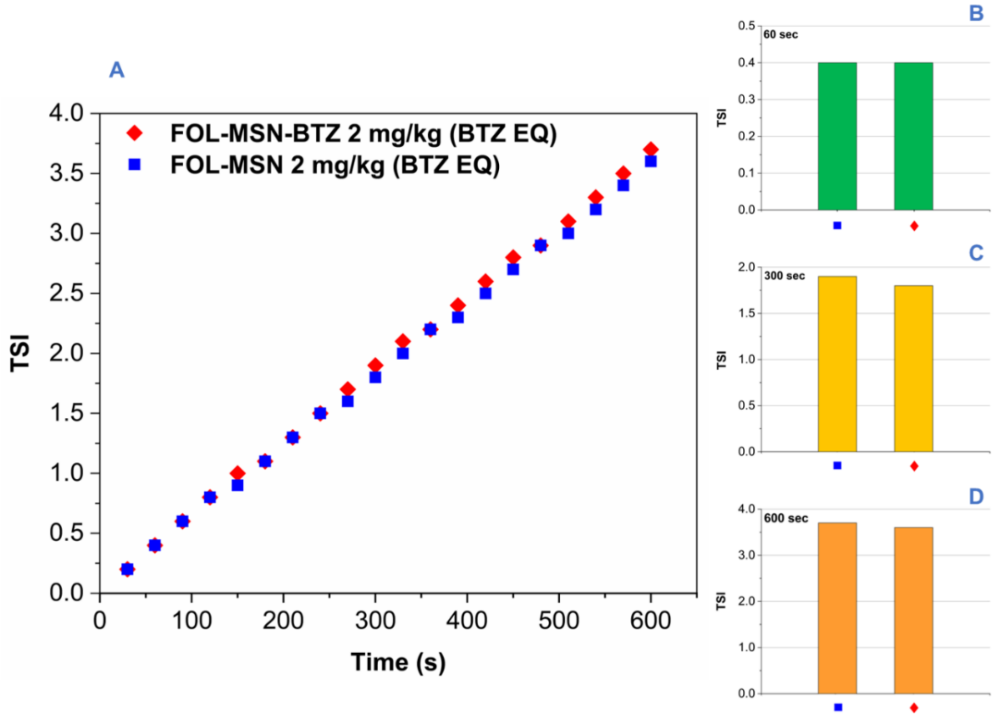

Figure 17. TSI value over time for FOL-MSN-BTZ and FOL-MSN (A); comparison of TSI value at 60 s (B), 300 s (C), and 600 s (D).

1.2.2 Experimental

MATERIALS AND METHODS

Chemicals and reagents

Reagents were commercially available with analytical grade and used as purchased without further purification. Solvents were purified according to well-known laboratory methods and freshly distilled prior to use. Triton X-100, neutral polyoxyethylene(10) octylphenyl ether, tetraethylorthosilicate (TEOS), (3-aminopropyl)-triethoxysilane (APTES), Folic acid (FOL), Diisopropylcarbodiimide (DIC), water (HPLC grade), Acetone (HPLC grade) were purchased by MERCK/Sigma-Aldrich (Milan, Italy). Bortezomib was purchased from LC Laboratories, Woburn, MA. Ethanol, Diethyl ether, 1,4-Dioxan, Dimethylformamide (DMF), Tetrahydrofuran (THF), trifluoroacetic acid (TFA), Acetic Acid from VWR. Dimethyl sulfoxide (DMSO) and Cyclohexane from Merck and Triethylamine from Carlo Erba. Ultrapure water was distilled with the MilliQ® water, Millipore.

Instruments

Thermogravimetric analysis (TGA) was carried out with a Netzsch STA 409 instrument between 20 °C and 850 °C at a ramp of 10 °C/min in air with a flow rate of 10 mL/min. The zeta potential values were determined using the Zetasizer ZS (Malvern Instruments Ltd., Malvern, U.K.) at 25.0 ±0.1 °C. The size and distribution of MSNs were determined, at 25.0 ± 0.1 °C, by Dynamic Light Scattering (DLS) analysis using a 90 Plus Particle Size Analyzer (Brookhaven Instruments Corporation, New York, USA).

NMR spectra have been obtained at 26.85 °C by means of a Bruker spectrometer Avance II 400 MHz.

^{29}Si {^{1}H} CP-MAS NMR spectra were recorded at 300 K on a Bruker spectrometer Avance II 400 MHz (9.4 T), operating at 79.4 MHz for ^{29}Si nuclide with a rotation rate of magic-angle of 6 KHz, 1000 scans, contact time 8 ms, a proton pulse of 5.1 ms and delay time of 5 s. Optimization of the Hartmann–Hahn condition was performed using a standard sample of Q8M8 ($Si[CH_3)_3]_8Si_8O_{20}$). ^{13}C{^{1}H} CP-MAS NMR spectra were obtained at 300 K and 100.63 MHz for nuclide ^{13}C with a rotation magic angle rate of 6 MHz, 4096 scans, a contact time of 2 ms, a proton pulse of 5.1 ms, and a delay time of 3 s. Optimization of the Hartmann–Hahn condition was performed using a standard adamantine sample. All the samples were pressed using a zirconia rotator of 4 mm with Kel-F caps.

Determination of Boron content was performed by Atomic Absorption Spectroscopy using Analytik Jena AG contrAA 700 - High-Resolution Continuum Source Atomic Absorption Spectrometer. HPLC analyses for release tests were performed on a Jasco HPLC analyzer using a flow rate of 1 mL/min. A 30/70% v/v of a solution nitrile acetate/water is used as mobile phase. A UV-VIS wavelength of 270 nm has been chosen to acquire the HPLC chromatograms.

Bortezomib release from FOL-MSN-BTZ has been monitored, as a function of time, after suspension in physiological solutions at pH 7 typical of haematic environment, pH 5 typical of intracellular organelles of cancer cells and pH 1.5, a strong acid pH whose study is useful for the evaluation of the amount of bortezomib not hydrolysed at pH 5 that could be considered retained in the nanoparticles.

SYNTHESIS OF FOL-MSN-BTZ PROTOTYPE

Synthesis of MSNs

MSU-type MSNs were synthesized through an assembly mechanism at neutral pH of non-ionic poly(ethylene oxide)-based surfactants and silica sources [28].

The surfactant Triton X-100 (21 g) was dissolved in ultrapure water (230 g) in about 4 h at room temperature. In order to create two phases, along the vessel it was slowly added a solution of TEOS (22 g) in cyclohexane (9.8 g) (molar composition TEOS: Cyclohexane: Triton X-100: H_2O 1: 1.08: 0.32: 120, respectively).

The synthesis was carried out at room temperature. The upper phase was removed, and the resulting precipitate was collected by filtration and washed three times with ultrapure water. Finally, the sample was dried in the oven at 70 °C for 24 h, thus a white powder was obtained.

Synthesis of AP-MSN

For the purpose, (3-aminopropyl)triethoxysilane (APTES) was used as amino-silane linker at two different APTES:MSN ratio: AP-MSN (1) was 2.03 g/g and AP-MSN (2) was 2.43 g/g. In a typical preparation, a solution containing APTES in ethanol (0.57 g/mL) was added to a suspension of (8 g) MSNs in ethanol (28.57 mL). The synthesis was left under stirring at room temperature for 48 h. The resulting suspension was filtered and washed once with ethanol and twice with ultrapure water. The resulting solid sample (AP-MSN) was then placed in an oven at 70 °C for 24 h.

Synthesis of FOL-MSN

Three different FOL-MSN samples were synthesized using different FOL/AP-MSN ratio, LF-FOL-MSN, MF-FOL-MSN and HF-FOL-MSN, equal to 0.11, 0.12 and 0.14 g/g respectively. Specifically, AP-MSN (1) was employed as starting material for LF-FOL-MSN, while AP-MSN (2) for MF-FOL- MSN and HF-FOL-MSN.

For the functionalization process, folic acid was used in combination with triethylamine (TEA) and N,N′-diisopropylcarbodiimide (DIC) in molar ratio 1:1.6:10.15 mmol, respectively.

Folic acid was completely dissolved in DMSO (0.04 g/mL). After that, TEA, DIC and finally AP-MSN were added. The so-obtained suspension was stirred at room temperature for 40 h. Finally, the mixture was filtered and washed with dimethylformamide (DMF), dioxane, diethyl ether and ultrapure water (once for each solvent). The resultant yellow powder (5 g) was dried and stored in sealed containers protected from light. Subsequently, the surfactant within the pores was removed at room temperature using 1 g of material in 0.33 L of ultrapure water. The number of extractions to perform to reach a complete surfactant removal was established monitoring (by TGA) the total mass loss of the sample subjected to subsequent extraction steps, until a constant value was reached. Then, the resulting FOL-MSN was washed with 1,4-dioxane and dried at 45 °C overnight.

CONJUGATION OF BTZ TO FOL-MSN

Functionalization of the inner pores

The inner pores of extracted FOL-MSN were functionalized with 3-glycidoxypropyltrimethoxysilane. To a suspension of extracted FOL-MSN (1 g) in 1,4-dioxane (30 mL), 3-glycidoxypropyltrimethoxysilane (2mL) was added. The reaction mixture was kept under stirring at room temperature for 18 h. Then, the mixture was washed with dioxane and THF and filtered, the resulting powder was dried at 45 °C. The recovered product was subsequently treated with a 0.001 N HCl solution (pH 2-3). The mixture was stirred at room temperature for 10 h. After this time, the reaction mixture was washed with ultrapure water and THF, filtered, and dried at 45 °C to afford FOL-MSN-DIOL.

Bortezomib loading

For FOL-MSN-BTZ preparation, bortezomib was loaded using a FOL-MSN-DIOL: BTZ molar ratio of 1:1.5 on the basis of the 1,2-diol linker content on extracted FOL-MSN, determined by TGA.

The reaction was carried out under inert atmosphere. FOL-MSN-DIOL was suspended in dry 1,4-dioxan then BTZ was added. The reaction mixture was gently stirred at room temperature for 24 h, then the nanoparticles were filtered and washed three times with dry dioxane and three times with dry dichloromethane. The recovered liquid phase was concentrated under reduced pressure and used for a second drug loading cycle. The second drug loading procedure was performed by adding 10% of the initially used amount of drug to the solution resulting from the first drug loading cycle. The reaction was left for 24 h at room temperature under gentle stirring. The final product (FOL-MSN-BTZ) was filtered and washed as previously described. The sample was then stored in sealed containers at -20 °C to preserve drug integrity.

Determination of bortezomib content in FOL-MSN-BTZ

The drug loading in FOL-MSN-BTZ was determined quantifying boron, exclusively present in BTZ molecule, by Flame Atomic Absorption (AAF). The BTZ content in FOL-MSN-BTZ resulted 10.38%.

The sample was treated as described in the following:

(1) dried at low temperature in a water bath (temperature heating plate 50 °C - bath temperature 38 °C); (2) transferred into plastic containers; (3) treated with 0.6 mL HF (complete dissolution of the MSN powder was observed); (4) treated with 0.1 mL HNO_3; (5) addition of 6.3 mL of ultrapure water (MilliQ-test 1) to reach the final 7 mL sample volume required for the spectrophotometric analysis. The obtained samples were analyzed by Atomic Absorption Spectroscopy (contrAA® 700, Analytikjena, Germany). The same technique and procedure were employed for the determination of the drug amount in the suspensions.

Polychromatic elemental maps

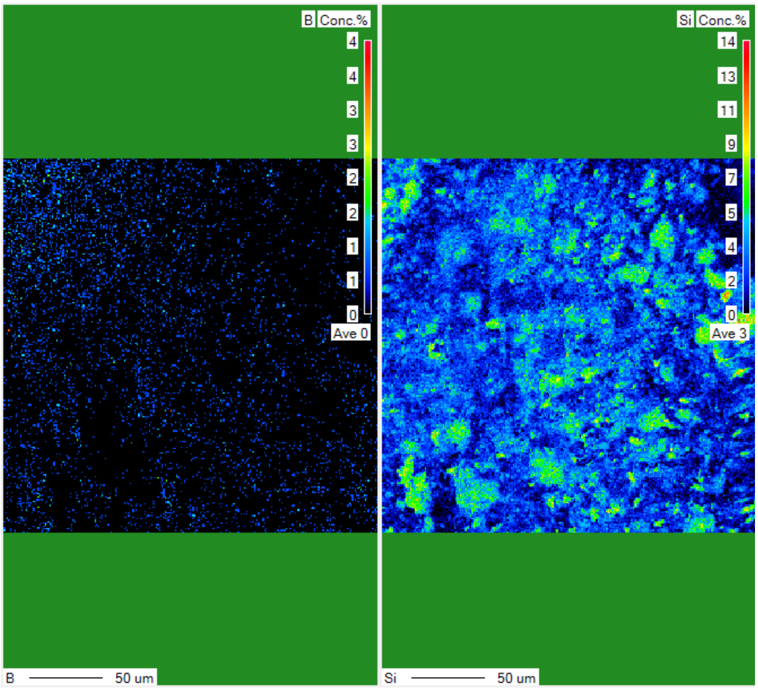

Figure 18. Polychromatic elemental maps of LF-MSN-BTZ sample.

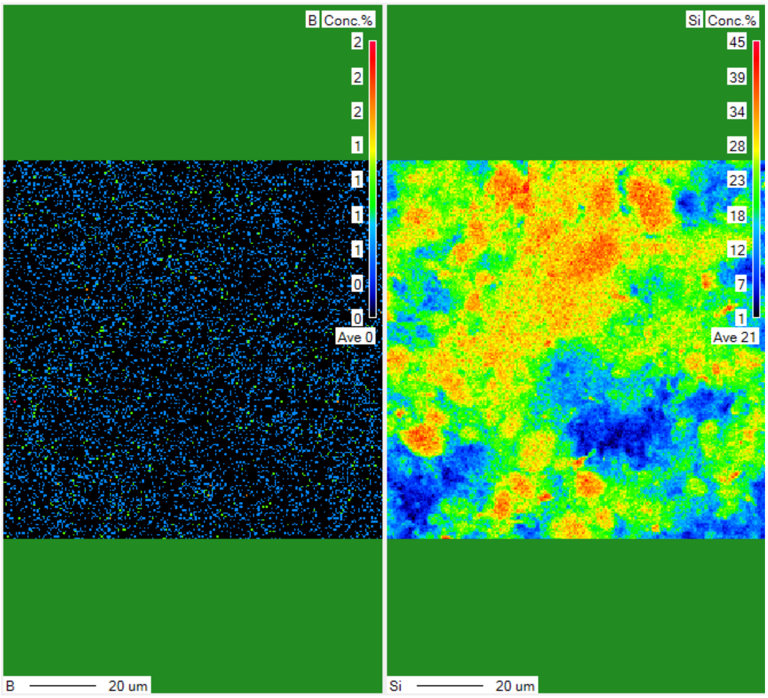

Figure 19. Polychromatic elemental maps of MF-MSN-BTZ sample.

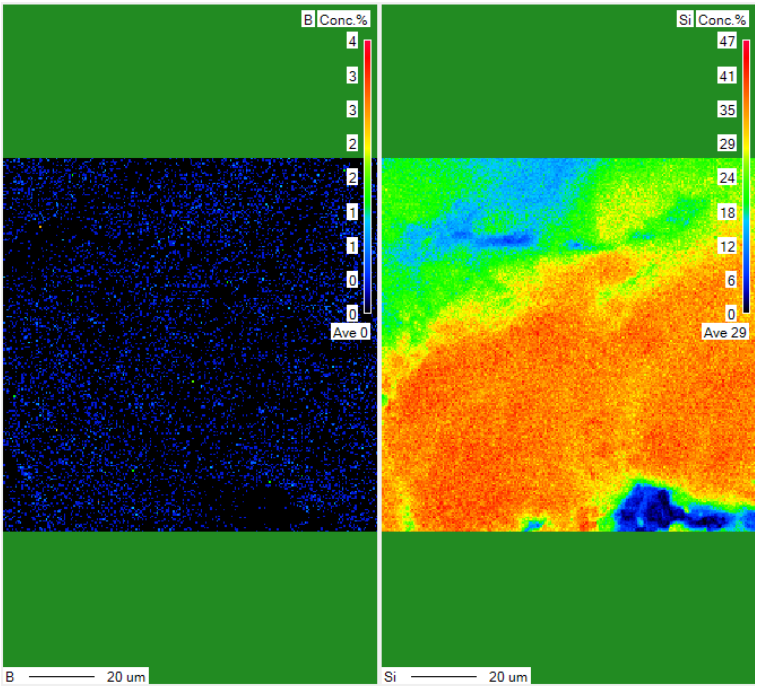

Figure 20. Polychromatic elemental maps of HF-MSN-BTZ sample.

Zeta potential and DLS characterizations

Sample	Hydrodynamic diameter [nm]	PdI	Zeta potential [mV]
MSN	344.13 ± 4.50	0.10	-30.21 ± 6.39
FOL-MSN-BTZ	373.15 ± 18.70	0.25	+18.13 ± 3.41

Table 4. Hydrodynamic diameter, polydispersity index (PdI) and zeta potentials of the starting MSN and the final FOL-MSN-BTZ; analysis were performed in triplicated, and the results are expressed as mean ± standard deviation.

NMR characterizations

Sample	ppm [$Si(OSi)_4$]	ppm [$Si(OSi)_3OH$]	ppm [$RSi(OSi)_3$]	ppm [$RSi(OSi)_2OH$]
FOL-MSN-BTZ	-109.79	-100.86	-65.84	-57.03

Table 5. Chemical shift of ^{29}Si NMR analysis.

Sample	ppm	ppm	ppm	ppm	ppm	ppm	ppm	ppm	ppm	ppm	ppm	ppm	ppm
FOL-MSN-BTZ	10.03	23.24	43.29	47.22	49.62	55.13	67.49	72.49	129.84	132.21	143.72	147.97	163.93

Table 6. Chemical shift of ^{13}C NMR analysis.

In vitro BTZ release studies

Experimental release tests were carried out as following: 15 ml of phosphate and acetate buffer, and HCl solutions (pH 7, 5 and 1.5) were homogenized at 50 rpm and 0.004 g of each FOL-MSN-BTZ sample (LF, MF and HF) were added. Homogenization is maintained for 30 s to allow a complete dispersion of the solid in the buffer solutions.

At pre-established times, starting from 15 min, 20 µL of the release medium of each experiment were withdrawn, replaced with fresh medium, and analyzed by HPLC using a standard calibration curve of BTZ prepared under the same conditions.

HPLC analyses were carried out using a flow rate of 1 ml/min. A 30/70% v/v of a solution acetonitrile /water is used as mobile phase. A UV-VIS wavelength of 270 nm has been chosen to acquire the HPLC chromatograms. Experiments were performed in triplicate.

Cell cultures and treatments

Human FR+ MM RPMI-8226 (RPMI) and FR- normal foreskin fibroblast BJhTERT were purchased from ATCC where they were authenticated. Cells were stored according to supplier's instructions and used within 6 months after frozen aliquots resuscitations. RPMI cells were cultured in RPMI-1640 medium and BJhTERT in Dulbecco's Modified Eagle's Medium (DMEM), both containing 10% Fetal Bovine Serum (FBS), 100 IU ml-1 penicillin/streptomycin (pen/strep) and 0.2 mM L-Glutamine. All culture media and additives were from Gibco™ (Life Technologies, Monza MB, Italy). Trypsin-EDTA solution 10x, formaldehyde, ethanol, tween80 and NP-40 by MERCK/Sigma-Aldrich (Milan, Italy). Mycoplasma negativity was tested monthly (PlasmoTest, Invivogen). For cells treatments, a ratio of 1 μg MSNs /10^5 cells was used on the basis of titration experiments. Free BTZ was added as positive control in amounts corresponding to the percentage of BTZ carried by FOL-MSN-BTZ.

Cell proliferation assays

MSNs effect on cell proliferation was assessed by trypan blue exclusion assay. Cells were seeded in triplicates for each condition, synchronized in serum free media (SFM) for 24 h and then treated for 1h with MSNs. Cells were then switched to fresh growing medium plus 1% FBS and counted after 72 h. Cell viability was determined by Countess® II Automated Cell Counter (Invitrogen, Life Technology, IT), according to supplier's instructions.

Transmission electron microscopy (TEM) and electron immunocytochemistry

For conventional TEM analysis and electron immunocytochemistry, cells were treated as described for growth experiments and harvested after 1 h of treatment to detect MSN uptake. All samples were routinely fixed, dehydrated, and resin-embedded using heat polymerization.

For indirect immunolabeling, grids were floated on drops of 1% bovine serum albumin (BSA) in PBS containing 0.02-M glycine at RT for 30 minutes to reduce nonspecific binding. Sections were then incubated with a rabbit polyclonal antibody against FR-b (1:10) (Invitrogen, cat#PA5-45768) at 4 °C overnight. The grids were then transferred to 50 mL drops of secondary antibody conjugated to 10 nm gold particles for 1 h, at room temperature. Observations were performed under a Jeol JEM-1400 Plus electron microscope (Jeol Ltd, Tokyo, Japan) operating at 80 kV.

Smart Chemotherapy Administration

The intravenous administration of the nanoparticles needed the preliminary development of a FOL-MSN-BTZ suspension preparation protocol for obtaining a well-known suspension volume/bortezomib amount ratio. To reach this level of knowledge, the suspension obtained from FOL-MSN-BTZ in 0.9% physiological solution was carefully examined to evaluate the real drug concentration during the administration phase. Three different suspensions (FOL-MSN-BTZ$_{1\text{-}3}$) of known concentration were prepared by magnetic stirring for 13 minutes, and the supernatant, equivalent to the upper half volume of the suspension, was immediately collected and analyzed by Atomic Absorption Spectroscopy, to evaluate the effective boron concentration that is equimolar to bortezomib in FOL-MSN-BTZ.

BTZ EQ concentration [mg/kg]	FOL-MSN-BTZ concentration [mg/kg]	FOL-MSN concentration [mg/kg]
1.0	14.6	13.1
1.5	21.9	19.6
2.0	29.2	26.2
2.5	36.5	32.7
3.0	43.8	39.3

Table 7. Corresponding FOL-MSN-BTZ and FOL-MSN concentrations for *in vivo* drug administrations.

In vivo studies

The *in vivo* studies were conducted by the Experimental Neurology Unit, Department of Medicine and Surgery of the University of Milano Bicocca (Monza, Italy).

MSN biodistribution

Metal concentrations in tissues were measured by Inductively Coupled Plasma-Mass spectrometry (ICP-MS) analysis. The determinations were carried out utilizing an Elan DRC-e ICP-MS instrument (Perkin-Elmer SCIEX, Canada) and the sample delivery system consisted of a PerkinElmer autosampler model AS-93 Plus with peristaltic pump and a cross-flow nebulizer with a Scott type spray chamber. The ICP torch was a standard torch (Fassel type torch) with platinum injector. A solution containing Rh, Mg, Pb, Ba, and Ce (10 µg/L, Merck) was used to optimize the instrument in terms of sensitivity, resolution, and mass calibration.

An Anton Paar Multiwave 3000 with programmable power control (maximum power 1400 W) and rotor XF100 (operating pressure up to 120 bar maximum; operating temperature, 260 °C maximum; construction material, PTFE-TFM for the liner) was used for the microwave digestion of samples. The digestion was achieved by adding 4 mL of

HNO_3 and 2 mL H_2O_2 into vessels containing 100 mg of tissue with a power ramp from 0 to 600 W in 15 min, a 10 min hold step at 600 W and a cooling step for 10 min. After digestion, the extracts were quantitatively transferred to a graduated polypropylene test tube, diluted with ultrapure water to 50 mL and then analyzed by ICP-MS.

Single element solutions of B, and Si (100 mg/L, Merck) were used for the preparation of aqueous calibration standard solutions after appropriate dilution. For the quantitative analysis, external calibration curves were built on seven different concentrations in a calibration range of 0.2-500 μg/L.

The comparison between the boron concentration values detected in tumor tissues of mice treated with free BTZ and FOL-MSN-BTZ was made by applying the non-parametric Mann-Whitney U test. The same statistical approach was applied to compare the boron concentrations found in lung tissues.

Statistical evaluation

Kaplan-Meier method was used to firstly assessed survival of animals in different treatment groups. Kruskal-Wallis test was performed to test any differences in terms of animals' tumor volume at baseline. Body weight was statistically analyzed using a 2-step approach involving a nonparametric One-way ANOVA test and the Kruskall-Wallis post-test (significance level set at $p<0.05$). Data analysis was carried out using the GraphPad 4.0 software (GraphPad Software, Inc., San Diego, California).

1.3 Conclusion

An MSN-based nanodevice was engineered for the targeted delivery of a chemotherapeutic agent. Designed to be internalized by myeloma cells, this system releases BTZ at slightly acidic pH, keeping the drug inactive at physiological pH, thereby sparing healthy cells. The balance of functionalities on the MSN surfaces was optimized for effective targeted therapy.

These nanodevices, administered as injectable suspensions, can deliver up to twice the maximum dose of bortezomib in a multiple myeloma animal model, leading to significantly enhanced therapeutic efficacy compared to the free drug. This increased efficacy is accompanied by lower toxicity, as treated animals showed improved survival, stable weight, and no marrow aplasia. The nanodevice preferentially accumulates BTZ in tumors, contributing to its higher efficacy and reduced distribution to other tissues.

These findings highlight the specificity of FOL-MSN-BTZ for FR-expressing myeloma cells, superior *in vivo* antitumor efficacy, and a better safety profile compared to conventional bortezomib formulations. This suggests that FOL-MSN-BTZ holds promise for future MSN-based treatments for multiple myeloma.

References

1. Antoine-Pepeljugoski, C., & Braunstein, M. J. Management of newly diagnosed elderly multiple myeloma patients. Current Oncology Reports, 2019, 21, 1-11.
2. Cancer stat facts: myeloma. 2024. https://seer.cancer.gov/statfacts/html/mulmy.html.
3. Globocan 2022 world fact sheet: world 2022. https://gco.iarc.who.int/media/globocan/factsheets/populations/900-world-fact-sheet.pdf.
4. He, J., Schmerold, L., Van Rampelbergh, R., Qiu, L., Potluri, R., Dasgupta, A., Li, Y., Hu, P., Nemat, S., Smugar, S.S., Zelter, O., Appiani, C., Li, Q., Mehre, M., Richarz, U. Treatment pattern and outcomes in newly diagnosed multiple myeloma patients who did not receive autologous stem cell transplantation: a real-world observational study: treatment pattern and outcomes in patients with multiple myeloma. Advances in Therapy, 2021, 38, 640-659.
5. Rao, M., Lamont, J. L., Chan, J., Concannon, T. W., Comenzo, R., Ratichek, S. J., Avendano, E.E. Serum Free Light Chain Analysis for the Diagnosis, Management, and Prognosis of Plasma Cell Dyscrasias: Future Research Needs: Identification of Future Research Needs From Comparative Effectiveness Review No. 73 [Internet]. Rockville (MD): Agency for Healthcare Research and Quality (US); 2012 Sep. Report No.: 12-EHC135-EF. PMID: 23678513.
6. Anderson, K. C., Alsina, M., Bensinger, W., Biermann, J.S., Chanan-Khan, A., Cohen, A.D., Devine, S., Djulbegovic, B., Gasparetto, C., Huff, C.A., Jagasia, M., Medeiros, B.C., Meredith, R., Raje, N., Schriber, J., Singhal, S., Somlo, G., Stockerl-Goldstein, K., Tricot, G., Vose, J. M., Weber, D., Yahalom, J., Yunus, F.; National Comprehensive Cancer Network. NCCN clinical practice guidelines in oncology: multiple myeloma. J Natl Compr Canc Netw. 2009, 7(9), 908-942.
7. Palumbo, A., Rajkumar, S. V., San Miguel, J.F., Larocca, A., Niesvizky, R., Morgan, G., Landgren, O., Hajek, R, Einsele, H., Anderson, K. C., Dimopolous, M. A., Richardson, P- G., Cavo, M., Spencer, A., Stewart, A. K., Shimizu, J., Lonial, S., Sonneveld, P., Durie, B. G. M., Moreau, P. International Myeloma Working Group consensus statement for the management, treatment, and supportive care of patients with myeloma not eligible for standard autologous stem-cell transplantation. J. Clin. Oncol. 2014, 32(6), 587-600.
8. Goel, U., Usmani, S., & Kumar, S. Current approaches to management of newly diagnosed multiple myeloma. American Journal of Hematology, 2022, 97, S3-S25.
9. Binder, M., Nandakumar, B., Rajkumar, S. V., Kapoor, P., Buadi, F. K., Dingli, D., lacy, M. Q., Gertz, M. A., Hayman S. R., Leung, N., Fonder, A., Hobbs, M., Hwa, Y. L., Muchtar, E., Warsame, R., Kourelis, T. V., Gonsalves, W. I., Russel, S., Lin, Y., Siddiqui, M., Kyle, R. A., Dispenzieri, A., Kumar, S. K. Mortality trends in multiple myeloma after the introduction of novel therapies in the United States. Leukemia, 2022, 36(3), 801-808.
10. Costa, L. J., Brill, I. K., Omel, J., Godby, K., Kumar, S. K., & Brown, E. E. Recent trends in multiple myeloma incidence and survival by age, race, and ethnicity in the United States. Blood Advances, 2017, 1(4), 282-287.
11. Moreau, P. The future of therapy for relapsed/refractory multiple myeloma: emerging agents and novel treatment strategies. In Seminars in hematology, 2012, Vol 49, S33-S46. WB Saunders.
12. Zhu, C., Song, Z., Wang, A., Srinivasan, S., Yang, G., Greco, R., Theilhaber, J., Shehu, E., Wu, L., Yang, Z-Y., Passe-Coutrin, W., Fournier, A., Tai, Y-T., Anderson, K. C., Wiederschain, D., Bahjat, K., Adrian, F. J., Chiron, M. Isatuximab acts through Fc-

dependent, independent, and direct pathways to kill multiple myeloma cells. Frontiers in immunology, 2020, 11, 1771.

13. Abramson, H. N. Immunotherapy of multiple myeloma: promise and challenges. ImmunoTargets and Therapy, 2021, 343-371.
14. Paul, B., Rodriguez, C., & Usmani, S. Z. BCMA-targeted biologic therapies: the next standard of care in multiple myeloma therapy. Drugs, 2022, 82(6), 613-631.
15. Rajkumar, S. V. Multiple myeloma: 2022 update on diagnosis, risk stratification, and management. American Journal of Hematology, 2022, 97(8), 1086-1107.
16. Rodriguez-Otero, P., van de Donk, N. W., Pillarisetti, K., Cornax, I., Vishwamitra, D., Gray, K., Hilder, B., Tolbert, J., Renaud, T., Masterson, T., Heuck, C., Kane, C., Verona, R., Moreau, P., Bahlis, N., Chari, A. GPRC5D as a novel target for the treatment of multiple myeloma: a narrative review. Blood Cancer Journal, 2024, 4(1), 24.
17. Health Canada. Approval of Velcade with conditions [letter to health professionals] Ottawa, ON: Health Canada; 2006. Available online at: https://www.hc-sc.gc.ca/dhp-mps/alt_formats/hpfb-dgpsa/pdf/prodpharma/velcade_dhcpl_lapds_2006_098077-eng.pdf.
18. Lund, T., Søe, K., Abildgaard, N., Garnero, P., Pedersen, P. T., Ormstrup, T., Delaissé, J-M., Plesner, T. First-line treatment with bortezomib rapidly stimulates both osteoblast activity and bone matrix deposition in patients with multiple myeloma, and stimulates osteoblast proliferation and differentiation in vitro. European Journal of Haematology, 2010, 85(4), 290-299.
19. O'Connor, R., Ooi, M. G., Meiller, J., Jakubikova, J., Klippel, S., Delmore, J., Richardson, P., Anderson, K., Clynes, M., Mitsiades, C. S., O'Gorman, P. The interaction of bortezomib with multidrug transporters: implications for therapeutic applications in advanced multiple myeloma and other neoplasias. Cancer Chemotherapy and Pharmacology, 2013, 71, 1357-1368.
20. Mynott, R. L., Wallington-Beddoe, C. T. Drug and solute transporters in mediating resistance to novel therapeutics in multiple myeloma. ACS Pharmacology & Translational Science, 2021, 4(3), 1050-1065.
21. Moore, D. C., Arnall, J. R., Harvey, R. D. Incidence and management of adverse events associated with Panobinostat in the treatment of relapsed/refractory multiple myeloma. Journal of Oncology Pharmacy Practice, 2019, 25(3), 613-622.
22. Yamamoto, S., & Egashira, N. Pathological mechanisms of bortezomib-induced peripheral neuropathy. International journal of molecular sciences, 2021, 22(2), 888.
23. Velasco, R., Alberti, P., Bruna, J., Psimaras, D., Argyriou, A. A. (2019). Bortezomib and other proteosome inhibitors—induced peripheral neurotoxicity: From pathogenesis to treatment. Journal of the Peripheral Nervous System, 2019, 24, S52-S62.
24. Dutta, D., Liu, J., Wen, K., Kurata, K., Fulciniti, M., Gulla, A., Hideshima, T., Anderson, K. C. BCMA-targeted bortezomib nanotherapy improves therapeutic efficacy, overcomes resistance, and modulates the immune microenvironment in multiple myeloma. Blood Cancer Journal, 2023, 13(1), 184.
25. Zhang, C., Kuo, J. C. T., Huang, Y., Hu, Y., Deng, L., Yung, B. C., Zhao, X., Zhang, Z., Pan, J., Ma, Y., Lee, R. J. Optimized Liposomal Delivery of Bortezomib for Advancing Treatment of Multiple Myeloma. Pharmaceutics, 2023, 15(12), 2674.
26. Shen, J., Wang, R., Wang, Q., Zhang, M., Liu, C., Tao, Z., Su, G. The improved anticancer effects of Bortezomib-loaded hollow mesoporous silica nanospheres on lymphoma development. Aging (Albany NY), 2021, 13(1), 411.
27. Nigro, A., Frattaruolo, L., Fava, M., De Napoli, I., Greco, M., Comandè, A., De Santo, M., Pellegrino, M., Ricci, E., Giordano, F., Perrotta, I., Leggio, A., Pasqua, L., Sisci, D.,

Cappello, A. R., Morelli, C. Bortezomib-loaded mesoporous silica nanoparticles selectively alter metabolism and induce death in multiple myeloma cells. Cancers, 2020, 12(9), 2709.

28. Garofalo, N., Comandé, A., Perrotta, I., Davoli, M., Niceforo, G., Pasqua, L. Synthesis and Characterization of Large Pore MSU-Type Mesoporous Silica. Advanced Science Letters, 2017, 23(6), 6026-6028.
29. Bagshaw, S. A., Prouzet, E., Pinnavaia, T. J. Templating of mesoporous molecular sieves by nonionic polyethylene oxide surfactants. Science, 1995, 269(5228), 1242-1244.
30. Meregalli, C., Carozzi, V. A., Sala, B., Chiorazzi, A., Canta, A., Oggioni, N., Rodriguez-menendez, V., Ballarini, E., Ceresa, C., Nicolini, G., Crippa, L., Orciani, M., Cavaletti, G., Marmiroli, P. Bortezomib-induced peripheral neurotoxicity in human multiple myeloma-bearing mice. Journal of Biological Regulators and Homeostatic Agents, 2015, 29(1), 115-124.
31. Zaksas, N. P., Soboleva, S. E., Nevinsky, G. A. Twenty Element Concentrations in Human Organs Determined by Two-Jet Plasma Atomic Emission Spectrometry. The Scientific World Journal, 2019, 2019(1), 9782635.

Chapter 2

FUNCTIONALIZED MESOPOROUS SILICA-BASED NANOFRAMEWORKS FOR SMART DELIVERY OF DOXORUBICIN TO CANCER CELLS

2.1 Introduction

Doxorubicin (DOXO), an anthracycline antibiotic isolated from the bacterium Streptomyces peucetius var. caesius [1], has been extensively employed as an antineoplastic agent in the treatment of various tumors and hematological malignancies for over 40 years.

Following its FDA approval, DOXO, either alone or in combination with other chemotherapeutics, has been widely used as a first-line therapy for numerous solid and metastatic tumors such as leukemia, neuroblastoma, breast, ovaria, thyroid, multiple myeloma, bladder, lung, AIDS-related Kaposi’s sarcoma [2].

The precise mechanism of action of this anticancer drug is not yet fully understood, but it is believed to involve the intercalation of DOXO between DNA base pairs. This intercalation inhibits the activity of topoisomerase II, an enzyme critical for DNA replication and repair, thereby blocking DNA synthesis and causing fragmentation of the polynucleotide structure [3,4].

Despite its wide use, the clinical application of DOXO is significantly limited due to its dose-dependent severe toxicity to various organs.

The most dangerous side effect is cardiomyopathy, a condition that can advance to congestive heart failure [5]. When combined with other drugs including paclitaxel, trastuzumab, docetaxel, and even radiotherapy, the risk of cardiotoxicity is increased [6].

Furthermore, DOXO exposure has been associated with neurotoxicity, especially impacting synaptic processes linked to hippocampal neurotransmission [7].

Moreover, DOXO-based chemotherapy often leads to myelosuppression, necessitating rigorous monitoring of hematological function [8]. These interconnected toxicities underscore the importance of careful management in DOXO treatment protocols.

To enhance efficacy and mitigate toxicity, significant efforts have been undertaken to address these challenges, including the exploration of low-dose regimens [9, 10], concurrent administration with cardioprotective agents [11, 12], and the development of novel anthracycline analogues [11, 13].

Over the last few decades, various drug delivery systems (DDSs) based on biocompatible nanomaterials have been investigated. These systems are designed with the primary objective of achieving targeted delivery and controlled release of anticancer drugs. The utilization of DDSs offers a promising strategy for enhancing the safety and efficacy of chemotherapeutic administration. By exploiting the targeting capabilities of DDSs, the risk of harm to healthy tissues can be minimized while maximizing the delivery of therapeutic agents to cancer cells [14].

The use of nano-based delivery systems indeed offers significant advantages in reducing toxicity, improving solubility, and enhancing both pharmacokinetic and pharmacodynamic profiles, while also protecting the drug from inactivation [15]. A large number of nanocarriers for DOXO have been developed, demonstrating better therapeutic effects compared to traditional chemotherapy. One of the most common methods involves encapsulating DOXO in liposomal nanoformulations. Doxil®, a liposomal doxorubicin formulation, was the first FDA-approved nanomedicine in 1995 and remains one of the most successful nanotechnology-based drugs. It is used for the treatment of metastatic ovarian cancer, AIDS-related Kaposi's sarcoma and multiple myeloma [16]. Since then, three other FDA-approved liposomal DOXO formulations have been developed: LipoDox®, Myocet®, and ThermoDox® [17, 18]. While these liposomal formulations have improved the safety profile of DOXO, their therapeutic efficacy has not surpassed conventional DOXO chemotherapy. This is due to limitations such as poor drug release, reduced bioavailability, and off-target distribution [17].

Significant efforts are being made to develop new doxorubicin carriers that address the limitations associated with liposomal formulations.

Mesoporous silica nanoparticles have been extensively exploited as efficient drug delivery systems, especially for DOXO administration, thanks to their unique chemical and physical properties. The large surface area of MSNs allows for high drug loading capacity, making them particularly suitable for doxorubicin delivery [19]. Functional groups can be anchored on external surface of MSNs to enable targeted drug delivery, thereby enhancing therapeutic efficacy [20, 21]. Moreover, the mesoporous structure of MSNs is tuneable, allowing for adjustments to fit various drug delivery needs [22]. Importantly, both *in vivo* and *in vitro* studies have demonstrated the good biodegradability and biocompatibility of MSNs, making them safe for medical applications [23].

Peng *et al.* developed a hybrid nanocarrier composed of MSNs and hydroxyapatite (HAP) for DOXO delivery. This nanocarrier was coated with hyaluronic acid (HA) and oligo HA to selectively target the CD44 receptor. Studies on tumor-bearing mouse model demonstrated that oligo HA-DOXO@MSNs/HAP significantly enhanced anticancer effects due to the more effective CD44 targeting by oligo HA compared to HA [24].

Recently, Bandyopadhyaya and coworkers developed mesoporous silica nanoparticles (MSNs) for DOXO delivery by incorporating amine groups, PEGylation, and specific functionalizations to improve their effectiveness. Folic acid (FA) and hyaluronic acid (HA) were used as targeting ligands. *In vivo* studies showed that the pH-sensitive nanocarriers MSN–NH_2–DOXO-PEG-FA and MSN–NH_2–DOXO-PEG-HA not only inhibited tumor growth from the beginning of treatment but also significantly extended the mice's survival time while reducing side effects compared to free DOXO [25].

Among different stimuli responsive strategies, pH-sensitive DDs are gaining popularity for their ability to provide controlled and precise drug delivery, thereby enhancing therapeutic efficacy. Abnormal pH levels are a key marker of cancer, making pH-responsive nanocarriers valuable for cancer therapy. These carriers undergo structural modifications in response to slight pH changes, enhancing targeting and drug uptake by tumor cells. A common approach in designing drug delivery systems is to use acid-sensitive bonds to attach the drug to the carrier.

In contrast to the neutral pH of approximately 7.4 found in normal tissues and blood, the tumor microenvironment typically exhibits a more acidic pH, ranging from 6.0 to 7.0 in extracellular regions [26]. This acidity is even more pronounced in subcellular compartments such as endosomes and lysosomes, where the pH can drop to between 5.5 and 6.0 in endosomes and to 4.5-5.0 in lysosomes [27].

This pH difference can be utilized to design systems that release anticancer drugs only after being internalized by cells through endocytosis. In these systems, the drug is linked to the nanoparticles with a bond that remains stable at the physiological pH of 7.4 but breaks easily in the acidic conditions of the endosomal compartments.

Hydrazone bond is a type of chemical linkage that finds large application in drug delivery systems. [28-30]. This acid-labile hydrazone linkage undergoes rapid hydrolysis in acidic microenvironments, such as those found in endosomes, ensuring the effective release of the therapeutic payloads. At the same time, hydrazone bonds remain stable under physiological pH conditions preventing premature release of the drug and ensuring it reaches its target effectively.

Doxorubicin features various functional groups in its structure (Figure 1), including carbonyl, hydroxyl, and amino groups, which can be harnessed to form acid-sensitive bonds.

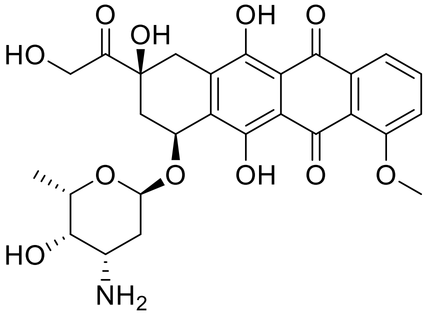

Figure 1. Doxorubicin chemical structure.

Notably, the hydroxymethylketone function in doxorubicin can be converted into a hydrazone group, which underscores its potential in developing pH-sensitive drug delivery systems. This conversion occurs through the reaction of the carbonyl group with a hydrazine derivative.

As part of my PhD research activity, a mesoporous silica-based nanodevice (FOL-MSN-BTZ), able to selectively deliver the antineoplastic drug bortezomib (BTZ) to folate receptor overexpressing multiple myeloma (FR þ MM) cells has been developed [31]. The nanodevice employs folic acid (FOL), grafted onto its external surface, as a targeting ligand, which facilitates tumor recognition and cell internalization. BTZ is covalently linked to the internal pore surfaces via a pH-sensitive bond, enabling its release specifically in the acidic environment of the tumor. These features make the mesoporous silica-based nanodevices highly suitable for designing targeted cancer therapies.

Building on this achievement, our research focused on creating a similar mesoporous silica-based device for the targeted delivery of doxorubicin, resulting in the development of FOL-MSN-DOXO. In this system, folic acid is used as the targeting molecule on the external surface of the mesoporous silica nanoparticles (MSNs), while doxorubicin is conjugated to the internal pore walls through an acid-labile hydrazone bond. This bond allows the drug to remain protected in the bloodstream and to be released only within the acidic intracellular compartments of tumor cells. This design ensures that doxorubicin acts specifically on cancer cells without affecting surrounding healthy tissues. Folic acid is widely used as a targeting ligand because the folate receptor is a valuable target for tumor-specific drug delivery [32].

This system, which incorporated DOXO linked to MSN pores via a hydrazone bond, served as the basis for developing a new prototype: HER2PEP-MSN-DOXO. In this innovative design, folic acid on the external surface of the MSNs was replaced with a peptide ligand specifically designed to target the HER2 receptor.

The HER2 receptor is a crucial therapeutic target in the treatment of HER2-overexpressing (HER2+) breast cancer, which is recognized as one of the most aggressive subtypes [33].

We successfully identified, synthesized, and conjugated the appropriate amino acid sequence to the MSNs outer surface to ensure effective interaction with the HER2 receptor. Furthermore, we evaluated the impact of HER2PEP-MSN-DOXO on the proliferation of HER2+ and HER2- cell lines and examined its uptake and localization within cells using transmission electron microscopy (TEM).

2.2 Synthesis and in vitro evaluation of FOL-MSN-DOXO prototype

Article being prepared

2.2.1 Results and Discussion

We achieved the development of the mesoporous silica-based nanosystem, FOL-MSN-DOXO, using MSU-type mesoporous silica nanoparticles.

The antineoplastic drug doxorubicin was anchored to the nanocarrier pore walls through an acid-sensitive hydrazone bond using a hydrazide-containing linker. The MSU-type mesoporous silica nanoparticles were obtained through a biphasic synthetic procedure carried out at room temperature, without the use of a mineralizing agent. We employed tetraethyl orthosilicate (TEOS) as the silica source and the surfactant Triton X-100 as structure-directing agent.

TEM and SEM analyses (Figure 2) were performed on nanoparticles to examine their morphology. The results revealed that MSNs exhibited a uniform diameter size ranging from 80 to 120 nm and showed a porous texture consistent with mesoporous silica materials.

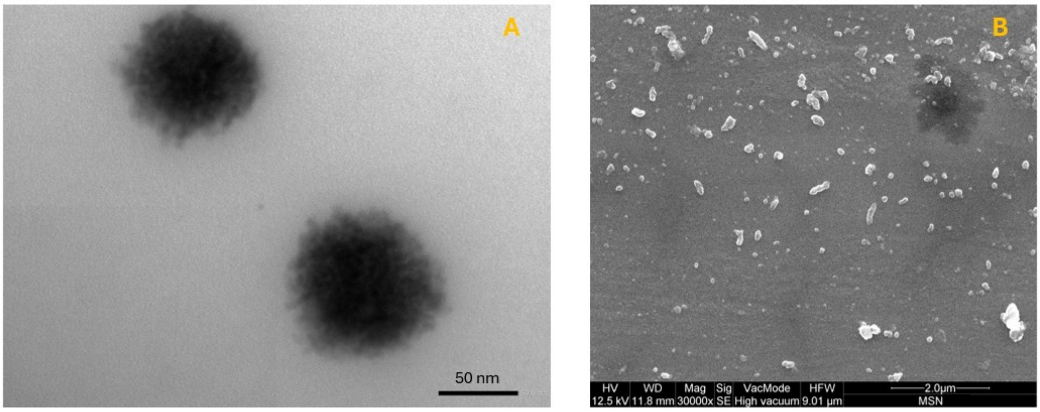

Figure 2. TEM (A) and SEM (B) micrographs of starting MSNs.

The external surface of as-synthesized MSNs was firstly functionalized with (3-Aminopropyl)triethoxysilane (APTES), resulting in amine-functionalized nanoparticles (AP-MSN). Then, folic acid (FOL), the targeting molecule, was covalently conjugated to the nanoparticles (FOL-MSN) through the formation of amide bonds between the amino groups of AP-MSN and the carboxylic function of folic acid (Scheme 1).

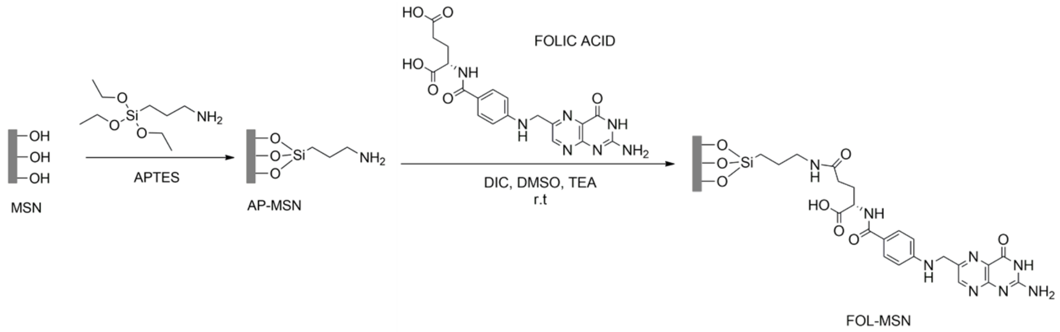

Scheme 1. Synthesis of FOL-MSN.

Thermogravimetric analysis of the sample before and after functionalization with FOL showed an increment of the organic compound mass on the sample by 12.20%.

Importantly, to prevent a substantial reduction in pore volume, MSNs were externally functionalized before surfactant extraction. This approach ensured that a significant pore volume was maintained after surfactant removal, with the folic acid targeting molecule predominantly anchored on the external surface, thereby facilitating efficient drug loading.

Surfactant within the pores of FOL-MSN was then efficiently removed by solvent extraction using ultrapure water, resulting in FOL-MSN-EXT.

The next steps involved synthesizing a hydrazide-functionalized linker and inserting it into the pores of the extracted FOL-MSN system (FOL-MSN-EXT). This process is crucial for anchoring DOXO via an acid-sensitive hydrazone bond.

First, the inner pores of FOL-MSN-EXT were modified with amino groups by grafting APTES, resulting in FOL-MSN-APint. Next, a hydrazide-containing linker (SAH) was prepared by reacting succinic anhydride with hydrazine monohydrate at room temperature. This linker was incorporated into FOL-MSN-AP$_{int}$ by forming an amide bond with the amino groups on the pore walls, using DIC (N,N′-diisopropylcarbodiimide) as the condensing agent and triethylamine (TEA) as the base (Scheme 2).

Finally, DOXO was conjugated to the hydrazide-modified nanoparticles (FOL-MSN-HYD) via a hydrazone bond between the hydrazide's amino group and DOXO hydroxymethyl ketone, creating FOL-MSN-DOXO (Scheme 2).

The amount of drug loaded (3.5%) in FOL-MSN-DOXO was determined by thermogravimetric analysis (TGA) and UV-VIS analysis (λabs = 481 nm).

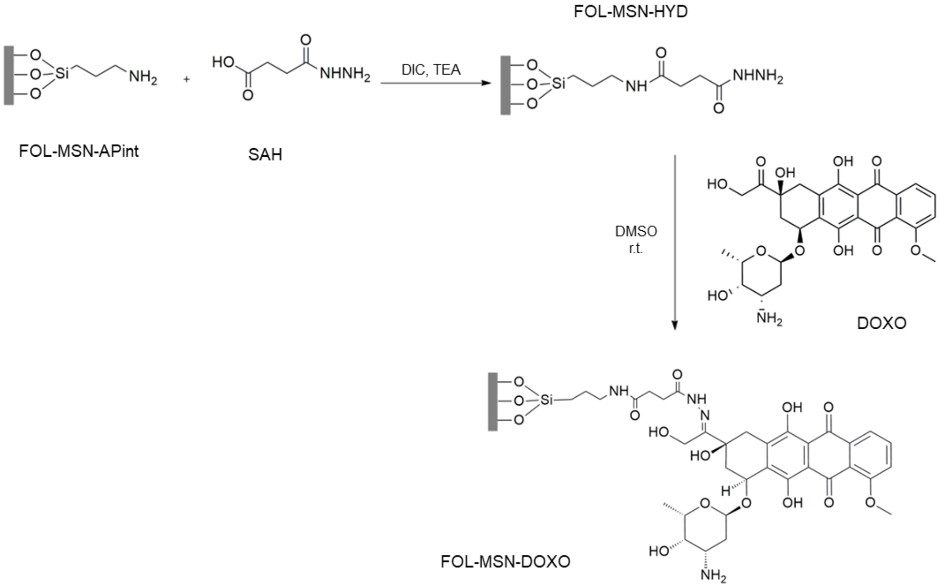

Scheme 2. Synthesis of FOL-MSN-DOXO.

The N_2 adsorption-desorption isotherms for all synthesized MSN systems exhibited type IV behaviour as shown in Figure 3. According to IUPAC classification, this confirms the mesoporous feature of the materials.

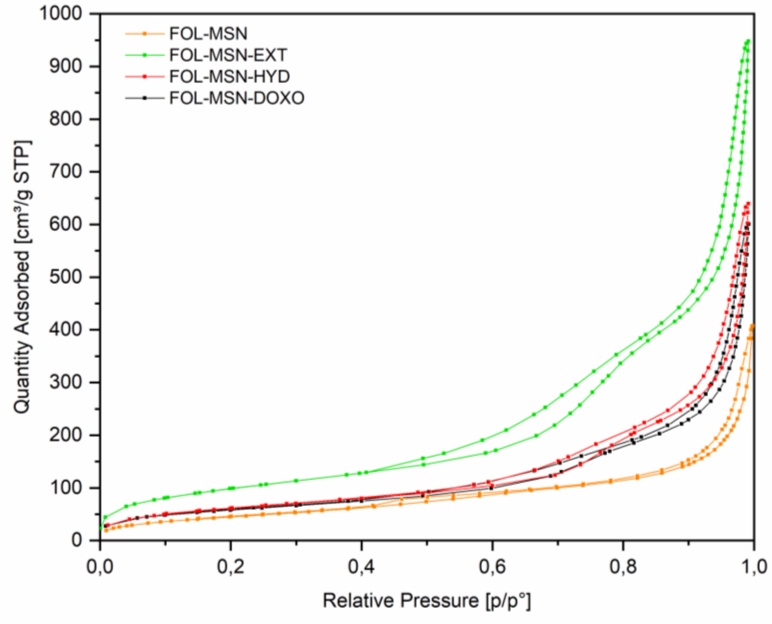

Figure 3. Nitrogen adsorption-desorption isotherms of FOL-MSN (orange), FOL-MSN-EXT (green), FOL-MSN-HYD (red) and FOL-MSN-DOXO (black).

The BET (Brunauer-Emmett-Teller) surface area and pore volume values, determined using the BJH (Barrett-Joyner-Halenda) method, are presented in Table 1. The removal of surfactant from the inner pores of FOL-MSN led to an increase in the BET surface area, from 170 m^2/g before extraction to 364 m^2/g for FOL-MSN-EXT. Similarly, the pore volume increased to 0.89 cm^3/g in the extracted FOL-MSN. However, subsequent surface modification resulted in a progressive decrease in both BET surface area and pore volume. Specifically, the BET surface area decreased to 212 m^2/g and the pore volume decreased to 0.49 cm^3/g in the FOL-MSN-DOXO sample.

Sample	BET Surface area [m^2/g]	Pore volume [cm^3/g]
FOL-MSN	170	0.32
FOL-MSN-EXT	364	0.89
FOL-MSN-APint	295	0.71
FOL-MSN-HYD	226	0.57
FOL-MSN-DOXO	212	0.49

Table 1. BET surface area and pore volume values at $P/P^0 = 0.96$ of the MSN systems obtained in the FOL-MSN-DOXO development process.

The zeta potential values for MSNs, FOL-MSN-APint, FOL-MSN-HYD and final FOL-MSN-DOXO were determined and are shown in Table 2. The MSNs exhibited a negative zeta potential of -30.2 mV due to the negatively charged silanol groups on their external surface.

Sample	Zeta potential [mV]
MSN	-30.2
FOL-MSN-APint	+18.4
FOL-MSN-HYD	+16.9
FOL-MSN-DOXO	+39.9

Table 2. Zeta potentials of MSNs, FOL-MSN-APint, FOL-MSN-HYD and FOL-MSN-DOXO samples.

FOL-MSN-APint showed a positive zeta potential of +18.4 mV, which is attributed to the positively charged aminopropyl groups attached to the internal surfaces of the nanoparticles when suspended in water. Functionalization with the hydrazide linker resulted in a similar zeta potential of +16.9 mV. After encapsulation of DOXO, the zeta potential of FOL-MSN-DOXO reached the value of +39.9 mV, due to the DOXO loading. This value is consistent with the presence of the protonated amino group attached to the pyran moiety of DOX.

The positive zeta potential of FOL-MSN-DOXO indicates a higher potential for cellular uptake. This is due to the electrostatic attraction between the positively charged nanoparticles and the negatively charged cell membrane [34].

XRD analysis was performed on the initial MSN sample, as well as on AP-MSN, FOL-MSN-EXT, and finally FOL-MSN-DOXO (Figure 4). In all MSN samples, a singular diffraction peak was observed within the range of $2\theta = 0.75°-0.83°$, indicative of the absence of long-range crystallographic order, a characteristic feature of MSU-family mesoporous materials (Figure 4). The comparison of the diffraction patterns of the different systems shows that the functionalization and modifications carried out to obtain the final nanocarrier, FOL-MSN-DOXO, did not alter the material structure.

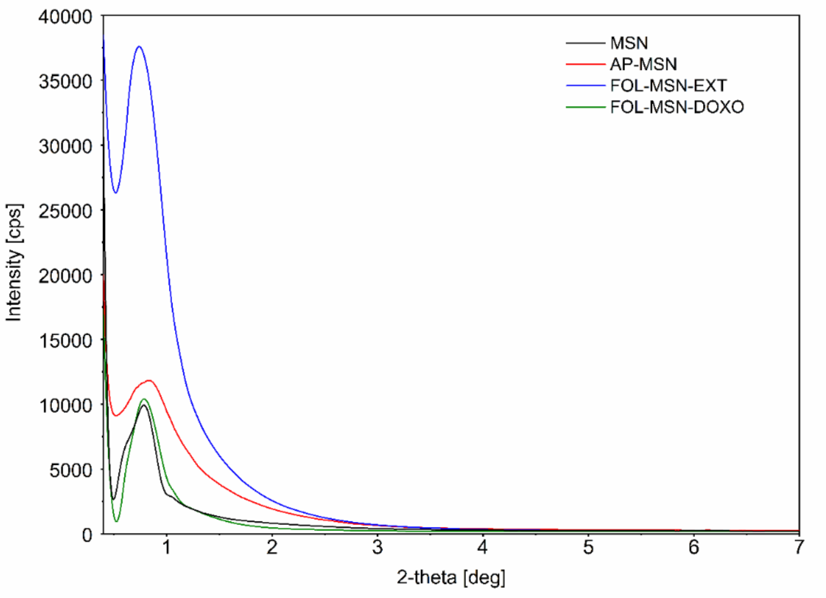

Figure 4. Comparison of XRD diffraction patterns for MSN (black), AP-MSN (red), FOL-MSN-EXT (blue), and FOL-MSN-DOXO (green).

In the FT-IR spectrum of final prototype FOL-MSN-DOXO (Figure 5, black curve), the characteristic absorption bands for the stretching vibration of hydrazone bond (C=N) and the amide carbonyl group (C=O) of the linker overlap in the range 1650-1560 cm^{-1}. The IR spectrum of DOXO (Figure 5, blue curve) shows a band at 1731 cm^{-1}, characteristic of the stretching vibration (C=O) of the hydroxymethylcarbonyl group. This band is not detectable in the spectrum of FOL-MSN-DOXO, indicating the conversion of the carbonyl group to the hydrazone form. The conjugation of DOXO through the formation of the hydrazone bond is further confirmed by the appearance of a broad band centered at 1617 cm^{-1} in the FT-IR spectrum of FOL-MSN-DOXO, attributable to the stretching vibration of the C=N bond, which overlaps with the stretching vibration of the quinone carbonyl of DOXO (1580 cm^{-1}). Additionally, absorption bands in the range of 2845-2465 cm^{-1} and 2022-1987 cm^{-1} are observed in the FT-IR spectrum of FOL-MSN-DOXO, showing a pattern similar to that present in the same range in the FT-IR spectrum of DOXO [35].

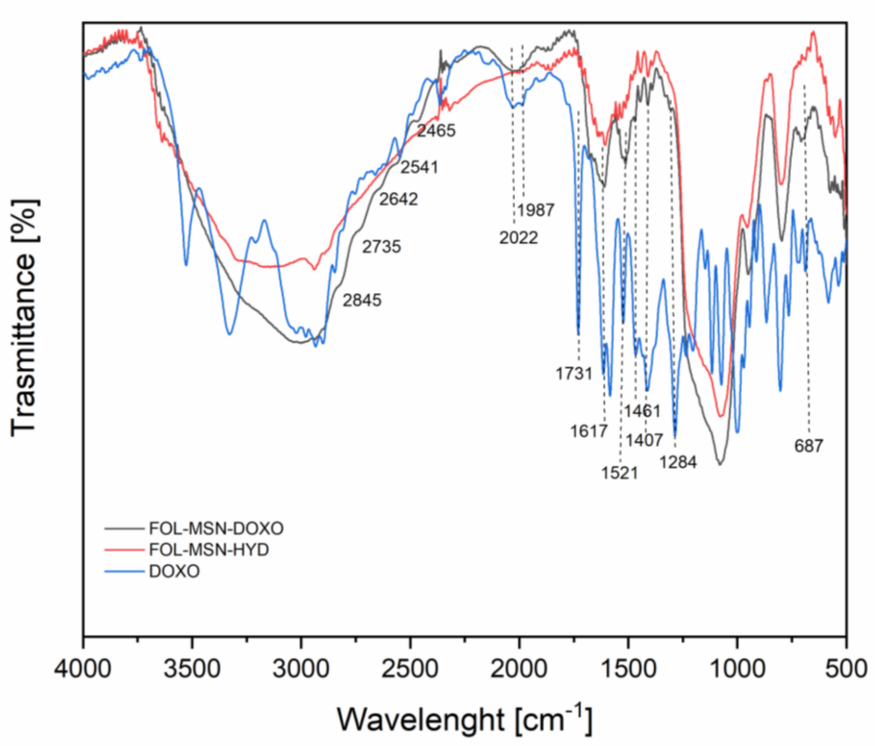

Figure 5. FT-IR spectra of FOL-MSN-DOXO (black), its precursor FOL-MSM-HYD (red), and DOXO (blue).

To study the pH dependence of doxorubicin release from the nanosystem, a series of experiments were conducted at different pH values. Buffer solutions with pH values of 7.4 (mimicking systemic circulation), and 5 (mimicking the tumor microenvironment), were used as release media.

In each experiment, 10 mg of FOL-MSN-DOXO were dispersed in 15 mL of buffer solution at the desired pH and stirred at room temperature. After 24 hours, the suspension was filtered and centrifuged, and the supernatant was collected for analysis. The DOXO content in the supernatant was measured using UV-Visible spectroscopy at an absorbance of 481 nm. The drug concentration was determined using standard calibration curves for DOXO UV absorbance at each pH level.

The results, shown in Figure 6, indicate that pH significantly affects DOXO release. At pH 7.4, only 7% of DOXO was released, suggesting a slow hydrolysis and a good retention of DOXO within the MSN-based nanosystem. At pH 5, corresponding to the acidic tumor environment, 43% of DOXO was released after 24 hours, demonstrating the pH-responsive behaviour of the nanovehicle.

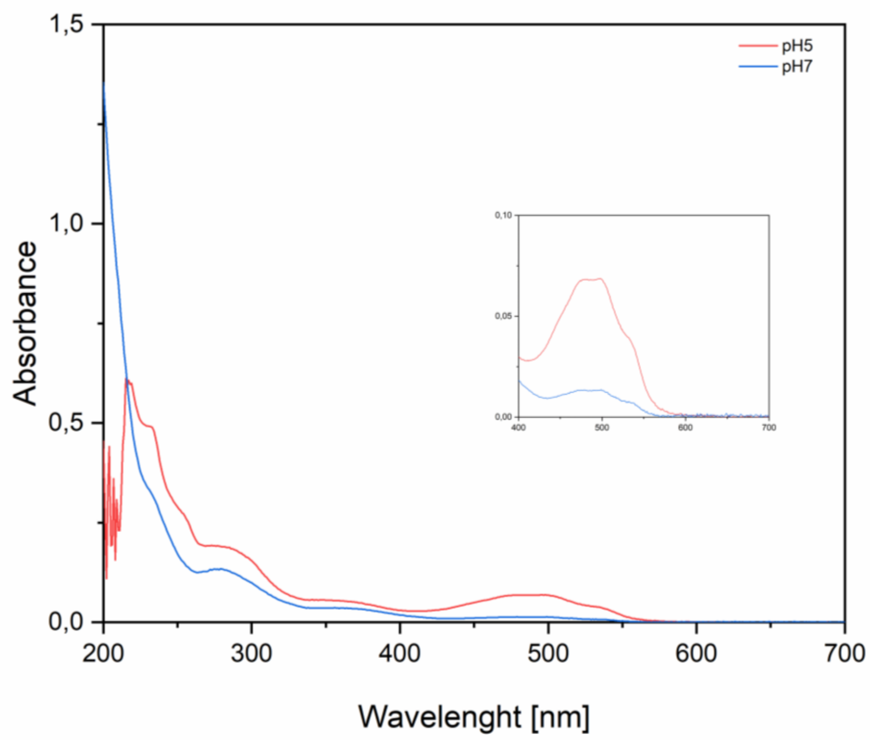

Figure 6. UV-Vis analysis of DOXO release after 24 h, at pH 7.4 (blue) and pH 5 (red). The insert box shows a zoom of the region between 400 nm and 700 nm.

The biocompatibility and efficacy of FOL-MSN-DOXO and vehicle alone (FOL-MSN) were first investigated on tumor and normal cell models, expressing or not FRα. The effect of MSNs on cell proliferation was evaluated on human FRα+ HeLa (cervix carcinoma) and T47D (breast cancer) cell lines. The FRα- 3T3L1 (mouse embryonic) and

BJhTERT (human neonatal) fibroblasts were used as normal cell models, not expressing FRα (Figure7A).

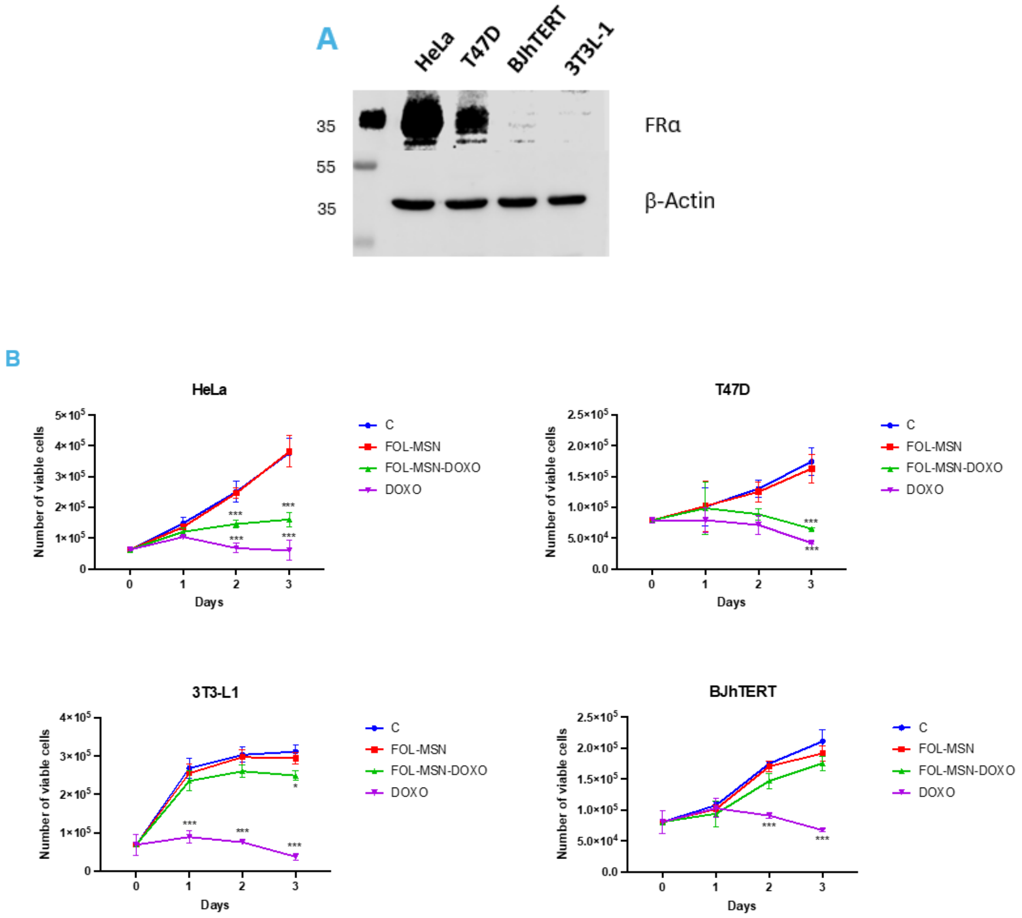

Figure 7. FOL-MSN-DOXO kills FRα+ cancer cells but not FRα- normal cells. (A) 50 μg of proteins from total lysates of indicated cell lines were loaded and subjected to WB analysis for FRα detection. β-actin was used as loading control. (B) FRα+ HeLa and T47-D cancer cells and FRα- 3T3L1 and BJhTERT normal cells were treated for 1h with FOL-MSN-DOXO or left untreated (C = control). MSN-FOL was used as negative control and the free drug DOXO as positive control (* $p \leq 0.05$, *** $p \leq 0.001$).

Strikingly, FOL-MSN-DOXO was able to selectively induce death only in FRα+ HeLa and T47-D cancer cells, but not in FRα- 3T3L1 and BJhTERT normal cells, while free DOXO was not selective and was toxic for all cell lines tested, independently of their FRα expression (Figure 7B). Our observations clearly show that, when loaded into MSNs, DOXO loses its toxicity on normal cells. Moreover, it is worth mentioning that the vehicle per se (FOL-MSN) was not toxic to either normal or cancer cells (Figure 7B). As confirmed by TEM observations, these results might directly stem from the evidence that FOL-MSN-DOXO selectively enter FRα expressing cells, while negligible uptake occurs in FRα- cells (red arrows in Figure 8A), thus preserving them from doxorubicin toxic effect. Immunogold labelling experiments on HeLa cells clearly show that FOL-MSN-DOXO uptake occurs through FRα-mediated endocytosis (Figure 8B).

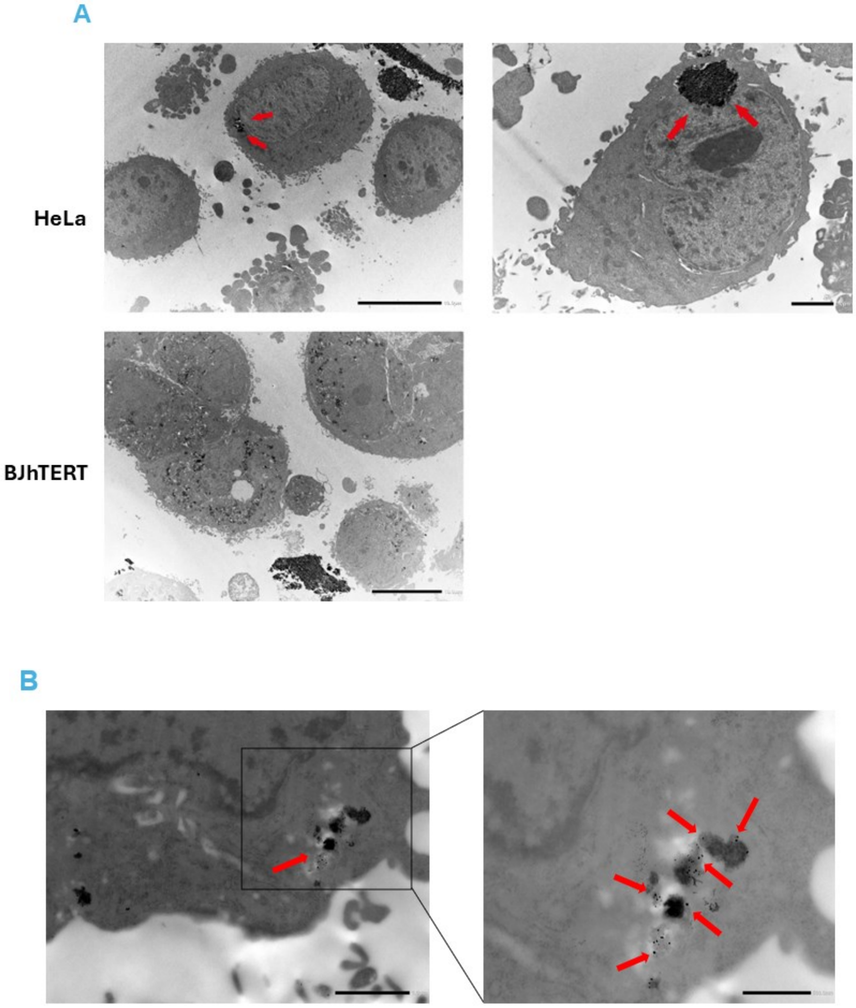

Figure 8. FOL-MSN-DOXO enter FRα+ cancer cells but not FRα- normal cells. (A) HeLa (upper panels) and BJhTERT (lower panels) were processed for TEM analysis. MSNs are indicated by red arrows. Images were taken at 1200x magnification, scale bars 10 µm (left panels) and at 3000x magnification (right panels, scale bars 2 µm). (B) Colloidal-gold immunocytochemistry for FRα (black dots indicated by arrows) in HeLa cells exposed to FOL-MSN-DOXO for 1h. MSNs sequestration in FRα-immunopositive intracellular vesicles are shown. Scale bars: 1 µm (left panel) and 500nm (right panel).

2.2.2 Experimental

MATERIAL AND METHODS

Chemicals and reagents

Reagents were commercially available with analytical grade and used as purchased without further purification. Solvents were purified according to well-known laboratory methods and freshly distilled before use. Ultrapure water was distilled with the MilliQ® water, Millipore.

The following chemicals were obtained from Sigma Aldrich: neutral polyoxyethylene(10)octylphenyl ether (Triton X-100), tetraethyl orthosilicate (TEOS), (3-aminopropyl)triethoxysilane (APTES), folic acid (FOL), diisopropylcarbodiimide (DIC), doxorubicin hydrochloride (European Pharmacopoeia (EP) Reference Standard), hydrazine monohydrate, succinic anhydride, 4-dimethylaminopyridine (DMAP), HPLC grade water, and HPLC grade acetone.

Ethanol, diethyl ether, 1,4-dioxane, dimethylformamide (DMF), tetrahydrofuran (THF), trifluoroacetic acid (TFA), and acetic acid were purchased from VWR. Dimethyl sulfoxide (DMSO) and cyclohexane were sourced from Merck, while triethylamine (TEA) was obtained from Carlo Erba.

Minimum Essential Medium (MEM), RPMI 1640 (1×) Medium, Dulbecco’s Modified Eagle’s Medium (DMEM), DMEM Nutrient Mixture F-12 (DMEM/F-12) and Fetal Bovine Serum (FBS) were from Gibco™ (Life Technologies, Monza MB, Italy). Trypsin-EDTA solution 10×, L-Glutamine, penicillin/streptomycin (pen/strep), D-Glucose, Hepes, Sodium Pyruvate, Non-Essential Amminoacids, Insulin and phosphate-buffered saline (PBS) were from Sigma Aldrich (Merck Spa, Milano MI, Italy).

Instruments

Thermogravimetric analysis (TGA) was carried out using a Netzsch STA 409 instrument between 20 °C and 850 °C with a heating rate of 10 °C/min in air with a flow rate of 10 mL/min.

The zeta potential values of MSNs were measured using a Zetasizer ZS (Malvern-Panalytical, U.K.), at pH 7.1 (25.0 °C ± 0.1 °C). The zeta potential values were calculated by the instrument software, using the Helmholtz–Smoluchosky equation.

Fourier transform infrared (FTIR) spectra were recorded using a FT/IR-4600 FT-IR spectrometer (Jasco, Germany). The ordered mesoporous framework of the synthesized materials was examined by small-angle powder X-ray diffraction (XRD) on a MiniFlex 600 Rigaku diffractometer, operating at 40 kV and 15 mA, employing Ni-filtered Cu Kα radiation in the 2θ range of 0.3–7° with a scan speed of 0.3 deg/min.

N_2 adsorption−desorption isotherms at 77 K were collected using a Tristar II Plus 3.02 porosimeter (Micromeritics, Norcross, GA) under continuous adsorption conditions. A 300 UV-Vis Evolution spectrophotometer (Thermo Fisher Scientific, Waltham, MA, USA) was used to evaluate doxorubicin amount. Full absorption spectra of DOXO were measured in the range 200-700 nm, with the maximum absorption peak at 481 nm. Standard solutions with DOXO concentrations ranging from 0.5 ppm to 50 ppm were tested. Three parallel samples were measured to gain the average value.

^1H and ^{13}C NMR spectra were recorded on a Bruker Avance 300 instrument at 300 MHz and 75 MHz, respectively. Chemical shifts (δ) are reported in ppm. Coupling constants (*J*) are reported in Hertz (Hz).

SYNTHESIS OF FOLIC ACID-FUNCTIONALIZED MESOPOROUS SILICA NANOPARTICLES (FOL-MSN)

Synthesis of Mesoporous Silica Nanoparticles (MSNs)

The surfactant Triton X-100 (21 g) was dissolved in ultrapure water (230 g) at room temperature, with stirring for about 4 h. To create two phases, a solution of TEOS (22 g) in cyclohexane (9.8 g) was slowly added along the vessel (molar composition TEOS: Cyclohexane: Triton X-100: H2O was 1: 1.08: 0.32: 120, respectively).

The synthesis was carried out at room temperature. The upper phase was removed, and the resulting precipitate was collected by filtration and washed three times with ultrapure water. Finally, the sample was dried in the oven at 70 °C for 24 h, resulting in a white powder was obtained.

Synthesis of Amine Functionalized MSNs (AP-MSN)

The nanoparticles' surface was coated with aminopropyl groups using (3-aminopropyl)triethoxysilane (APTES).

A solution of APTES in ethanol (33 mL, 0.85 g/mL) was added to a suspension of MSNs (8 g) in ethanol (27.85 mL). The mixture was stirred at room temperature for 48 h. Afterward, the suspension was filtered and washed once with ethanol and twice with ultrapure water. The resulting sample (AP-MSN) was dried in an oven at 70° C for 24 h.

Synthesis of FOL-MSN

Folic acid (1.11 g, 2.51 mmol) was dissolved in DMSO (19.30 mL). Triethylamine (0.554 mL, 3.9 mmol), DIC (1.11 mL, 7 mmol), and AP-MSN (5.50 g) were added to the solution. The obtained suspension was stirred at room temperature for 40 h. Afterward, the mixture was filtered and washed sequentially with dimethylformamide, dioxane, diethyl ether, and ultrapure water. The resulting yellow powder (6.98 g) was dried and stored in sealed, light-protected containers.

To remove the surfactant within the pores, 1 g of the material was suspended in 0.33 L of ultrapure water at room temperature. The number of extractions required for complete surfactant removal was determined by monitoring the total mass loss of little amounts of samples via thermogravimetric analysis (TGA) after each extraction step until a constant value was reached. Finally, the solution from the last extraction was filtered, and the obtained nanoparticles (FOL-MSN-EXT) were washed with 1,4-dioxane and dried at 45 °C overnight.

CONJUGATION OF DOXO TO FOL-MSN USING PH-SENTITIVE HYDRAZONE BOND

Synthesis of FOL-MSN-DOXO

Synthesis of FOL-MSN-APint

FOL-MSN-EXT was suspended in 1,4-dioxane at a concentration of 0.05 g/mL. APTES (2.2 g per gram of MSNs) was then added to the suspension. After stirring for 18 h, the mixture was filtered, and the solid residue was washed with 1,4-dioxane and THF. The resulting nanoparticles (FOL-MSN-APint) were dried overnight at 45 °C.

Synthesis of Succinic Acid Monohydrazide Linker

Succinic anhydride (1 g, 10 mmol) and DMAP (10 mg, 0.08 mmol) were dissolved in DCM (50 mL). Subsequently, a solution containing hydrazine monohydrate (0.320 g, 6 mmol) in DCM (10 mL) was added to the mixture dropwise under vigorous stirring at room temperature. After 10 h, the solvent was evaporated under reduced pressure, resulting in a white solid (1.1 g).

^{1}**H NMR** (300 MHz, DMSO-d6) δ: 11.80 (sbroad, 1H, COOH), 9.76 (s, 1H, CONH), 2.48-2.40 (m, 2H, (CH2COOH), 2.40-2.28 (m, 2H, (CH2CONHNH2).
^{13}**C NMR** (75 MHz, DMSO-d6) δ: 173.95, 170.36, 29.32, 28.51.

Synthesis of FOL-MSN-HYD

Succinic acid monohydrazide (0.218 g, 1.65 mmol) was dissolved in DMSO (20 mL), then DIC (0,256 mL, 1.65 mmol) and triethylamine (0,230 mL, 1.65 mmol) were added. After 1 h, a suspension of FOL-MSN-APint in DMSO (0.03 g/mL) was added to the reaction mixture. The reaction was stirred at room temperature for 24 h. Following this, the reaction mixture was filtered, and a second loading cycle was performed under the same conditions for another 24 h at room temperature. The mixture was then filtered, and the recovered powder was washed with DMSO and diethyl ether yielding FOL-MSN-HYD (1.65 g).

Drug Loading

A 20 mL solution of doxorubicin hydrochloride in DMSO (0.013 g/mL) was added to a 30 mL suspension of FOL-MSN-HYD in DMSO (0.017 g/mL). The pH was adjusted to approximately 5 by adding a few drops of acetic acid. The reaction mixture was stirred at room temperature under an inert atmosphere for 24 h. Subsequently, the nanoparticles were filtered and washed with DMSO. To achieve a higher drug loading, the resulting solid was resuspended in DMSO, and a second drug loading was carried out under the same conditions. Then, the reaction mixture was filtered and thoroughly washed with DMSO, dry dioxane, and dry dichloromethane. The obtained nanomaterial, FOL-MSN-DOX, was stored in sealed containers at -20 °C, under anhydrous conditions and protected from light. The amount of doxorubicin loaded (3.5%) in FOL-MSN-DOX was determined by TGA and UV-VIS spectroscopy (λabs = 481 nm).

Cell Cultures and Treatments

Human FR positive (FR+) cervix adenocarcinoma HeLa and breast cancer T47D cell lines, and FR negative (FR−) normal mouse embryonic fibroblasts 3T3-L1 were purchased from ATCC, where they were authenticated. Cells were stored according to supplier's instructions and used within 6 months after frozen aliquot resuscitations. Normal foreskin fibroblast BJhTERT cells were kindly provided by Michael Lisanti, University of Salford, Manchester (UK). Cells were purchased from ATCC and transferred to our laboratory at passage n = 3 and handled as described above.

HeLa were cultured in MEM supplemented with 1% of non-essential amino acids, and 1% sodium pyruvate. T47D cells were grown in RPMI containing 2.5 g/mL glucose, 1% Na-Pyruvate, 10 nM Hepes, and 0.2 U/mL insulin. BJhTERT and 3T3-L1 were grown in DMEM. All media contained 10% FBS, 100 IU/mL pen/strep and 0.2 mM L-Glutamine (all from Gibco, Thermo Fisher Scientific Inc.). All the other listed reagents were purchased from Sigma-Aldrich (Merck KGaA, Darmstadt, Germany).

Mycoplasma negativity was tested monthly (PlasmoTest, Invivogen, Aurogene, Rome, Italy). For cell treatments, MSNs were resuspended in serum-free media (SFM) on a magnetic stirrer, and a ratio of 1 μg MSNs/10^5 cells was used on the basis of titration experiments and added to the cells for 1 h. Free DOXO was added, as positive control, in amounts (in μg) corresponding to the % (in weight) of DOXO carried by FOL-MSN-DOXO (3.5%).

Cell Proliferation Assays

MSNs effect on cell proliferation was assessed by trypan blue exclusion assay. Cells were seeded in triplicates for each condition, synchronized in SFM for 24 h and then treated for 1 h with 1 μg MSNs/10^5 cells. Cells were then switched to fresh growth medium (GM) plus 1% FBS and counted after 72 h. Cell viability was determined by Countess® II Automated Cell Counter (Invitrogen, Life Technology), according to supplier's instructions.

Western Blotting (WB) Assay

FR proteins expression was assessed by WB using total protein lysates from tested cell lines. 50 μg of non-denatured (for FR detection) proteins were run on an 10% polyacrylamide gel. The following primary Abs were employed: FOLR1 (MAB5646, R&D Systems Inc., Minneapolis, MN, USA), β-Actin (sc-69879, Santa Cruz Biotechnology, Inc.). IRDye (LI-COR Corporate, NE, USA) were used as secondary Abs. Images were acquired with the Odyssey FC Imaging System (LI-COR Corporate).

Transmission electron microscopy (TEM) and electron immunocytochemistry

Conventional TEM analysis and electron immunocytochemistry were conducted as previously described [31]. Cells were treated as described for growth experiments and harvested after 1h of treatment to detect MSNs uptake. Samples have been routinely fixed, dehydrated, and resin embedded using heat polymerization. Ultrathin sections were collected on copper grids and contrasted using both lead citrate and uranyl acetate.

For indirect immunolabeling, grids were floated on drops of 1% bovine serum albumin (BSA) in PBS containing 0.02-M glycine at room temperature for 30 min to reduce nonspecific binding. Sections were then incubated with a rabbit polyclonal antibody against FOLR1 (MAB5646, R&D Systems Inc., Minneapolis, MN, USA) at 4 °C overnight. The grids were then transferred to 50 μL drops of secondary antibody conjugated to 10-nm gold particles for 1 h, at room temperature. Observations were performed under a Jeol JEM-1400 Plus electron microscope (Jeol Ltd., Tokyo, Japan) operating at 80 kV.

2.3 Synthesis of HER2-targeted mesoporous silica nanoparticles for DOXO delivery in breast cancer (HER2PEP-MSN-DOXO)

2.3.1 Results and Discussion

The *in vitro* experimentations on FOL-MSN-DOXO prototype show promising results for using MSN-based nanocarriers as smart delivery systems for Doxorubicin. The engineered nanosystem, which incorporate DOXO via pH-sensitive bond and target the folate receptor (FR) exhibit high selectivity towards FR+ cancer cells, reducing toxicity in normal cells compared to doxorubicin alone.

Furthermore, TEM and colloidal immunocytochemistry confirm that MSNs are selectively taken up by receptor-specific endocytosis in cancer cells, causing cancer cell death, with no internalization observed in FR-low normal cells. These results indicate that the system provides both selective drug release and efficient intracellular uptake, enhancing therapeutic outcomes.

Building on these encouraging results, a new MSN-based DOXO delivery system has been developed. This system features a more selective peptide ligand grafted onto the external surface to better recognize overexpressed receptors on tumor cells, specifically targeting the Human growth factor receptor HER2.

The overexpression of the HER2 gene is a key factor in breast cancer development and is often associated with a poor prognosis. While HER2 positivity occurs in other cancers, it is a crucial therapeutic target for treating HER2-positive (HER2+) breast cancer, one of the most aggressive subtypes [33]. This subtype has a higher risk of recurrence, increased early-stage mortality, and drug resistance.

HER2 belongs to the epidermal growth factor receptor (EGFR) family of tyrosine kinase, which also includes HER1, HER3 and HER4. All family members mainly consist of three domains: an extracellular ligand-binding domain, a transmembrane domain, and an intracellular region. Ligand-induced homo- or hetero-dimerization of HER proteins triggers the activation of many intracellular signals, playing a crucial role in many human cancers by regulating cell proliferation, growth, survival, and differentiation [36]. As opposite to the other EGF receptors, HER2 has no identifiable ligands and cannot assemble into ligand-dependent homodimerization. It can form heterodimers with other ligand-activated HER proteins or self-assemble into ligand-independent homodimer in overexpression condition, such as in cancer [37, 38]. The most active and tumor-promoting combination is thought to be HER2 heterodimer with HER3 [39].

Deregulation of HER2, whether through mutation or overexpression, can lead to oncogenesis [40-42]. This condition has been discovered in many cancers, including breast, colorectal, bladder, gastric, oesophageal, endometrial, and ovarian cancers [43], highlighting the role of HER2 in tumor diagnosis and treatment [44]. These findings highlight the importance of HER2 as a prognostic and predictive marker for the development of advanced technologies for targeted breast cancer therapy. Several strategies have been employed to target HER2, including monoclonal antibodies, tyrosine kinase inhibitors, antibody-drug conjugates, small molecules. Recently, the use of HER2-targeting peptides has shown significant improvements in treating HER2-positive breast cancer [45].

Monoclonal antibodies, such as Herceptin (Trastuzumab), have been developed to specifically target and inhibit the growth of HER2-overexpressing cancer cells. Herceptin, a recombinant monoclonal antibody against HER2, has been successfully used in treating metastatic breast cancer that overexpresses this receptor [46, 47].

Herceptin binds to the C-terminal portion of domain IV on HER2. This interaction involves three regions on HER2: residues 557-561 (loop 1), residues 570-573 (loop 2) and residues 593-603 (loop 3). The interactions with loop 1 and loop 3 are mainly electrostatic, while loop 2 makes mostly hydrophobic contacts [48]. These electrostatic and hydrophobic interactions between HER2 and Herceptin can be blocked by small peptide molecules or peptidomimetics targeting HER2 extracellular domain IV.

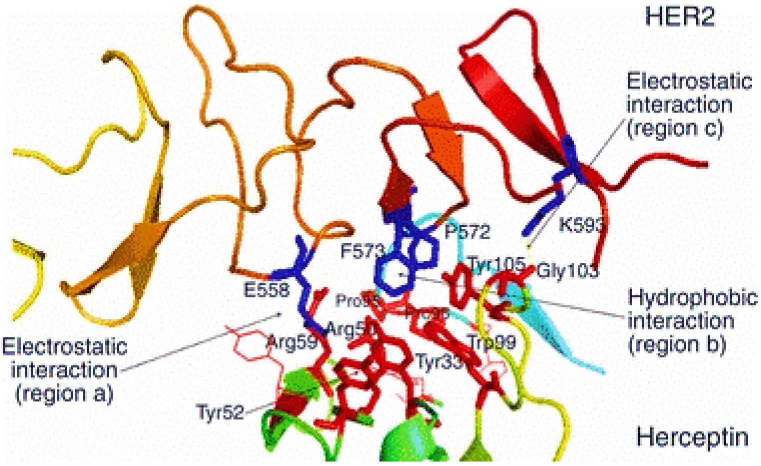

Figure 9. Crystal structure of HER2-herceptin complex showing part of domain IV of HER2 interacting with Herceptin. Residues involved in hydrogen bonding and hydrophobic interactions within the HER2-Herceptin binding pocket are shown. Herceptin residues are represented as red sticks, and HER2 domain IV residues are shown in blue. Herceptin amino acids are labeled with a three-letter code, while HER2 residues are labeled with a single letter code [49].

Based on the HER2-Herceptin binding site and the interactions between the involved amino acid residues [49], we designed short peptides to specifically target HER2.

The interactions of the designed peptides with HER2 have been studied and evaluated using computational methodologies based on molecular docking and molecular dynamics (MD) simulations, crucial for understanding the physical and chemical basis of molecular recognition at both static and dynamic levels. The computational investigations were conducted by the PROMOCS laboratory (Prof. Marino) at the Department of Chemistry and Chemical Technologies, University of Calabria.

Through these studies, an amino acid sequence with strong affinity for the HER2 receptor was identified and named HER2PEP. This sequence was used as a targeting molecule in the MSN-based nanocarrier for doxorubicin delivery. The amino acid sequence of the peptide is not disclosed due to confidentiality clauses associated with the project results, as these findings may be included in a future patent application. Consequently, the amino acid sequence in HER2PEP is represented as R$_5$-R$_4$-R$_3$-R$_2$-R$_1$, with the N-terminal residue (R$_5$) on the left, and the C-terminal residue (R$_1$) on the right.

Particular attention was focused on regions A (residues 557-561), B (residues 570-573), and C (residues 593-603) of HER2, where HER2PEP was targeted, resulting in three different complexes (Figure 10).

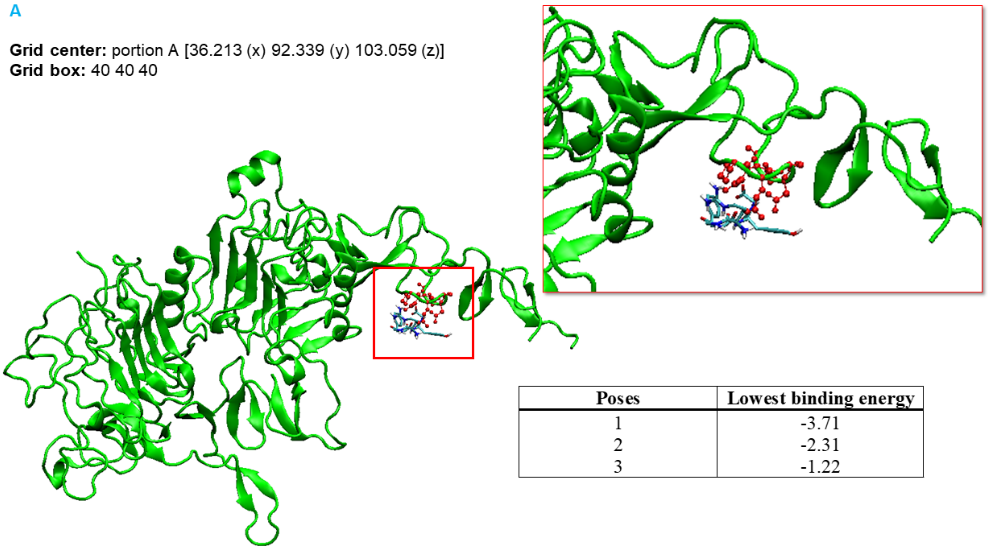

Poses	Lowest binding energy
1	-3.71
2	-2.31
3	-1.22

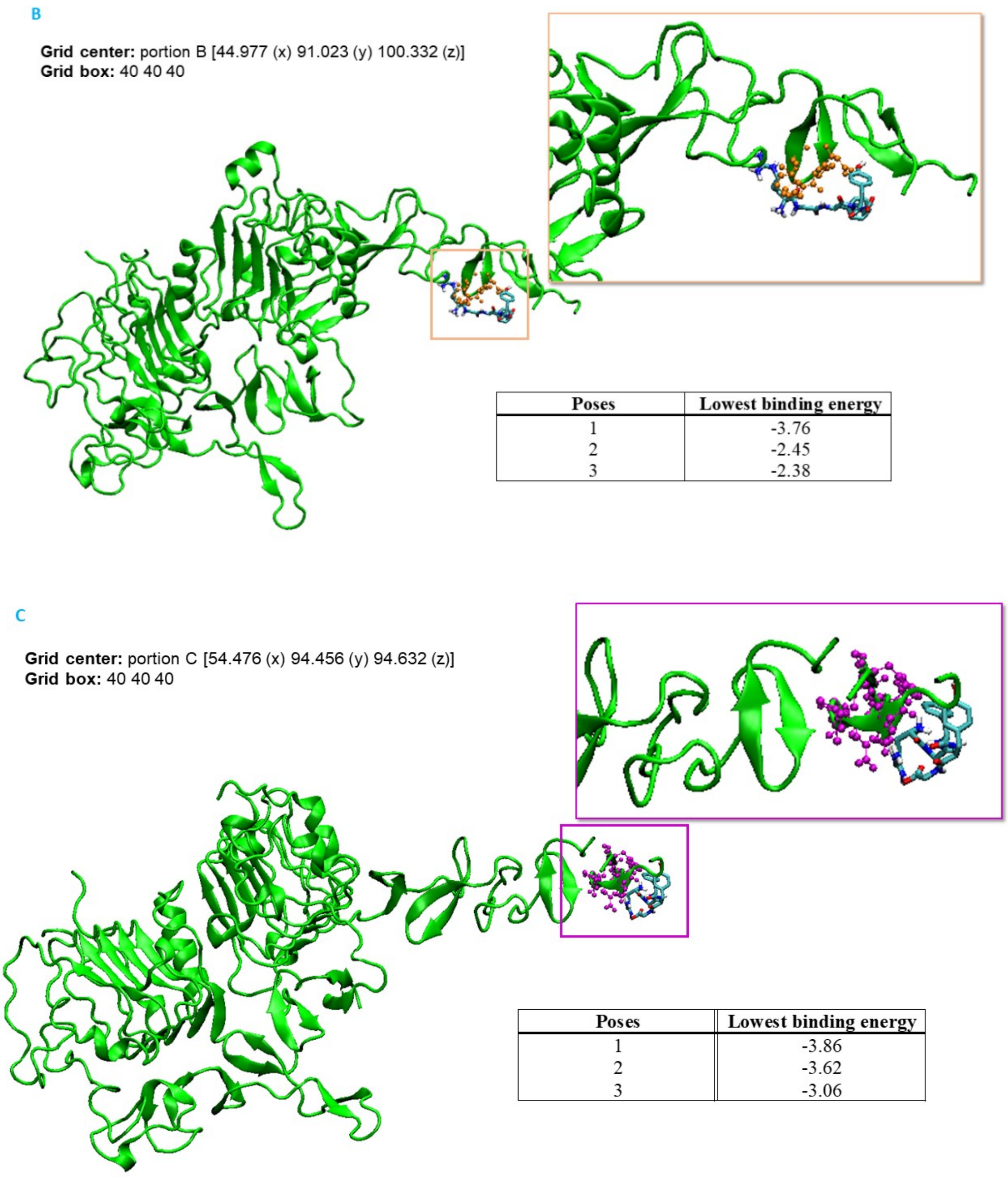

Grid center: portion B [44.977 (x) 91.023 (y) 100.332 (z)]
Grid box: 40 40 40

Poses	Lowest binding energy
1	-3.76
2	-2.45
3	-2.38

Grid center: portion C [54.476 (x) 94.456 (y) 94.632 (z)]
Grid box: 40 40 40

Poses	Lowest binding energy
1	-3.86
2	-3.62
3	-3.06

Figure 10. The best docked poses for each targeted region of HER2, A. B, and C. The conditions of the molecular docking and the three considered docked poses are reported.

Based on the binding energies from molecular docking, the HER2PEP pentapeptide exhibited the highest affinity in region C, followed by region B, and then region A (Figure 10). MD simulations were performed for all the threes poses and the results in terms of RMSD (root-mean-square deviation), an indicator of the stability of the protein-complex, are depicted in Figure 11.

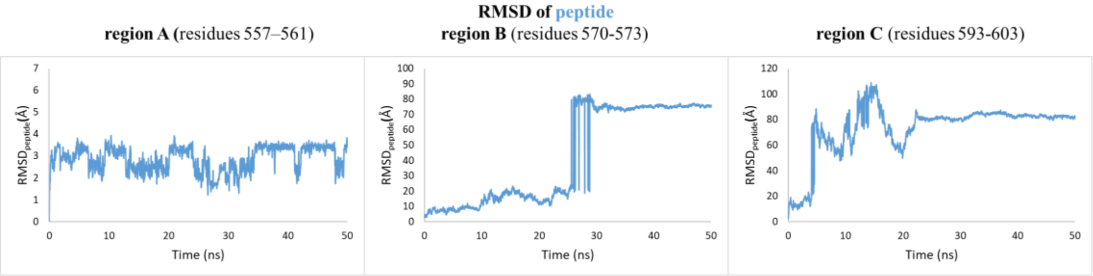

RMSD of peptide

region A (residues 557–561) **region B** (residues 570-573) **region C** (residues 593-603)

Figure 11. RMSD (in Å) of HER2PEP peptide during the MD of HER2:HER2PEP.

Examining the RMSD of HER2PEP reveals distinct dynamic behaviors in the different regions. In region B, the peptide starts to move away after about 30 ns, while in region C, detachment occurs at the beginning of the MD simulation. These findings indicate a low affinity of HER2PEP for regions B and C, despite their higher affinities observed in docking studies.

From RMSD of the MD of HER2:HER2PEP complex in region A reveals a distinct behavior (Figure 11). Specifically, the mobility of peptide in this region is reduced, with oscillations within 3.5 Å. This oscillation is due to the high flexibility of the peptide, promoted by two residues of the amino acid R_4. MD simulations indicate that region A plays a crucial role in stabilizing the peptide within HER2. Consequently, a detailed analysis of the interactions between HER2PEP and the target will be focused on region A.

Figure 12A shows the most representative structure from the cluster analysis of the MD trajectory for the HER2:HER2PEP complex, highlighting the amino acid residues of the binding region A. Figure 12B displays the non-covalent interactions (NCI) plot, helpful to establish the nature of specific interactions.

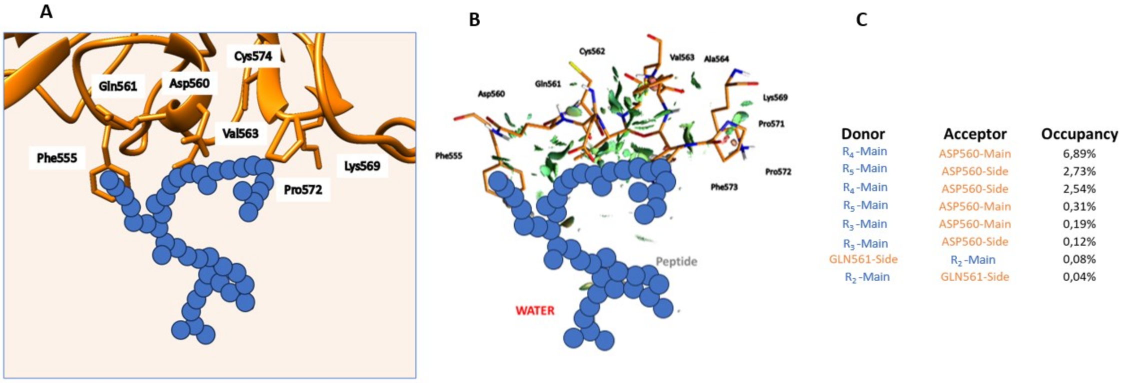

Donor	Acceptor	Occupancy
R_4-Main	ASP560-Main	6,89%
R_5-Main	ASP560-Side	2,73%
R_4-Main	ASP560-Side	2,54%
R_5-Main	ASP560-Main	0,31%
R_3-Main	ASP560-Main	0,19%
R_3-Main	ASP560-Side	0,12%
GLN561-Side	R_2-Main	0,08%
R_2-Main	GLN561-Side	0,04%

Figure 12. A) Zoom on the binding region A of HER2PEP, highlighting the interacting amino acid residues. B) Non-covalent interaction (NCI) surface around the HER2PEP ligand in binding region A of HER2, showing only intermolecular interactions. C) Donor-Acceptor hydrogen bond details of HER2:HER2PEP from MD simulation with the occupancy of each hydrogen bond.

The protein−ligand binding, indeed, depends upon a balance of stabilizing and destabilizing noncovalent interactions that contribute to the net thermodynamics. Most interactions (green isosurfaces) are non-covalent and mainly involve the R_5 and R_4 residues of HER2PEP with Gln561, Cys562, Val563 and Ala564 of HER2. The R_3 residue of HER2PEP interacts with Phe555 of HER2, while the remaining residues are exposed to water molecules. No relevant repulsive interactions were observed.

Based on the equilibrium MD trajectories, MM-PBSA (Molecular Mechanics Poisson-Boltzmann Surface Area) calculations were carried out to determine the binding affinity between HER2 and HER2PEP. The results are reported in Figure 13. The binding free energy of the ligand to HER2 is -15.13 kcal/mol, indicating a favorable stabilizing role of binding region toward the peptide. The binding affinity was computed using the whole production trajectory of MD simulation.

The per-residue decomposition analysis (Figure 13), useful to identify the key energetic contributors to the binding free energy, indicates that three residues (Glu558, Asp560, Gln561), among the five ones of region A, are the primary contributors to the binding of

HER2PEP to HER2. Additionally, the MM-PBSA decomposition of peptide shows that the R_5 residue is the most significant contributor to the overall binding energy.

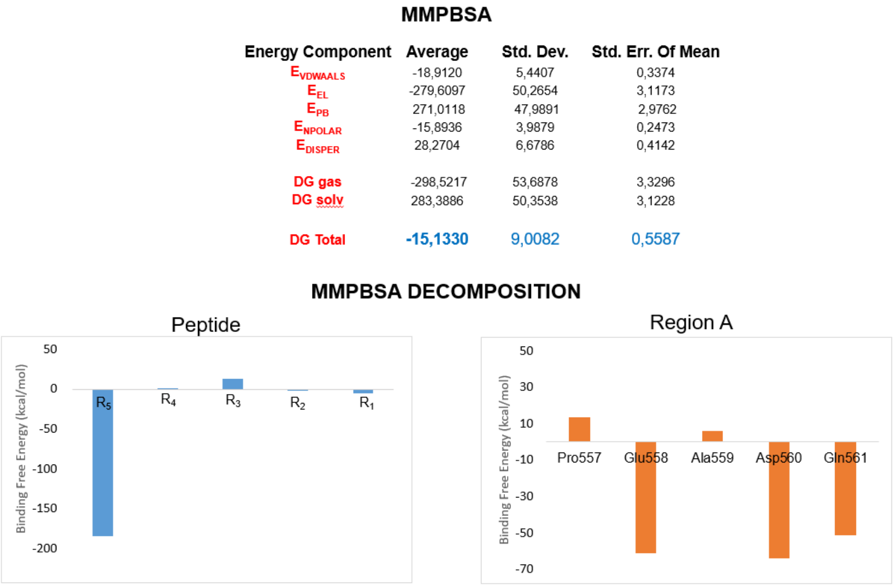

MMPBSA

Energy Component	Average	Std. Dev.	Std. Err. Of Mean
$E_{VDWAALS}$	-18,9120	5,4407	0,3374
E_{EL}	-279,6097	50,2654	3,1173
E_{PB}	271,0118	47,9891	2,9762
E_{NPOLAR}	-15,8936	3,9879	0,2473
E_{DISPER}	28,2704	6,6786	0,4142
DG gas	-298,5217	53,6878	3,3296
DG solv	283,3886	50,3538	3,1228
DG Total	-15,1330	9,0082	0,5587

MMPBSA DECOMPOSITION

Figure 13. MMPBSA results in kcal/mol and binding free energy (kcal/mol) decomposition per residue, for peptide and for region A of HER2.

In confirmation of the findings from MM-PBSA analysis, distance plots from the center of mass (COM) of the R_5 residue of HER2PEP to the COM of each amino acid residue in region A (557-561) (Figure 14) reveal that only the distance to Asp560 in region A (orange line) remains within 5.5 Å, suggesting that the interaction between Asp560 and the R_5 residue of the ligand is maintained throughout the MD simulations.

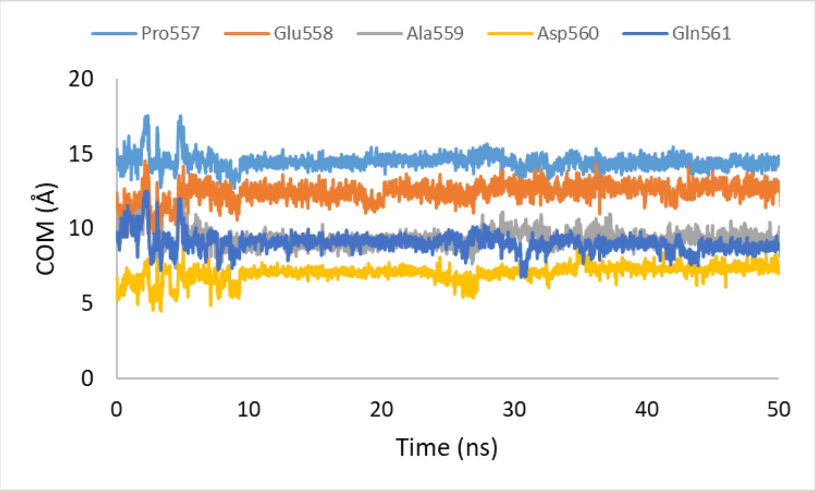

Figure 14. Distance plots from the center of mass (COM) of R_5 of peptide HER2PEP to the center of mass of each residue of the region A (sequence 557-561).

The simulations indicate that the peptide interacts specifically with the selected HER2 target, with the primary binding site located in region A. This behavior is likely supported by the reduced mobility of residues 557-561 in region A, compared to the more flexible regions B and C.

The HER2PEP pentapeptide was synthetized using solid-phase synthesis methodologies with reagents and strategies of Fmoc chemistry, using an automatic synthesizer. The synthesis started with the N-Fmoc-protected C-terminal amino acid, anchored to Wang resin (0.1 mmoles, loading 0.6 mmoles/g), using HBTU (N,N,N′,N′-Tetramethyl-O-(1H-benzotriazol-1-yl)uronium hexafluorophosphate) as the coupling agent.

Coupling reactions of N-Fmoc-L-amino acids were performed in DMF, in presence of HBTU (5 equivalents) and DIPEA (10 equivalents) for 20 min at 75 °C. The Fmoc-protecting groups were removed by treating the resin with a 20% solution of piperidine in DMF at 75 °C. This deprotection step was carried out for all amino acids in the sequence except for the N-terminal amino acid. Cleavage and removal of side-chain protecting groups were achieved using a mixture of TFA (95% v/v), water (2.5% v/v), and TIS (2.5% v/v) by microwave heating for 30 minutes at 38 °C (Figure 15).

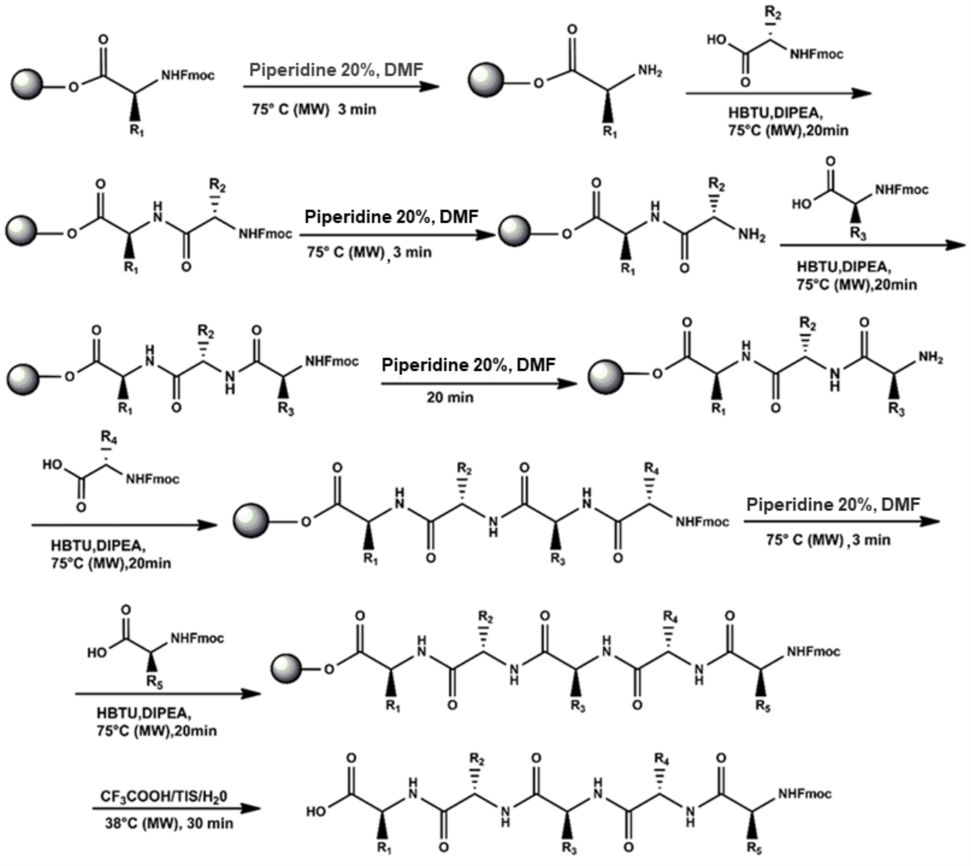

Figure 15. Synthesis of Fmoc-HER2PEP.

After cleavage, the peptide Fmoc-HER2PEP was obtained by precipitation with cold diethyl ether in 75% yield and high purity, as confirmed by HPLC analysis (Figure 16, rt = 8.214 min.). The peptide was characterized using ^{1}H NMR, ^{13}C NMR, FT-IR and HPLC-ESI-QTOF-MS analysis. The spectroscopic data confirmed the peptide's structure. The amino acid sequence of the peptide and its characterization details are not disclosed due to confidentiality clauses associated with the project results, as these findings may be included in a future patent application.

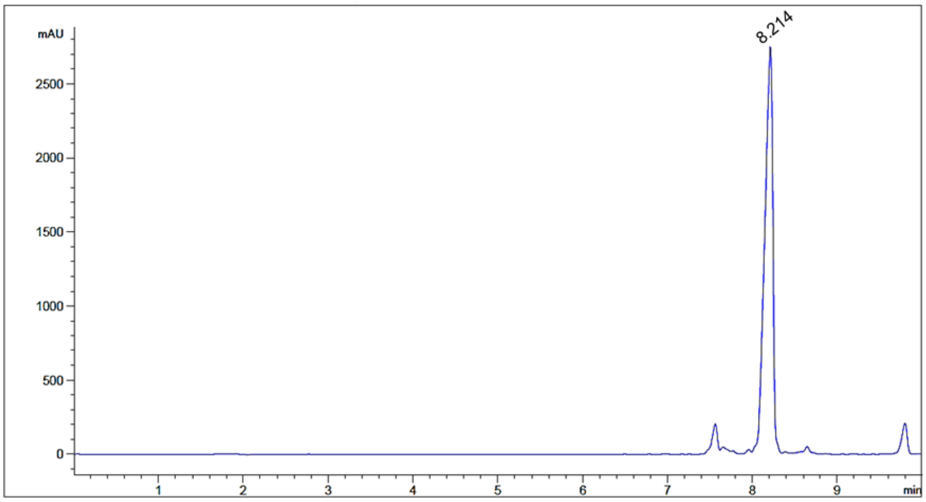

Figure 16. HPLC analysis of Fmoc-HER2PEP.

The synthesized Fmoc-HER2PEP peptide was used as a targeting ligand, replacing folic acid, to develop a new prototype, HER2PEP-MSN-DOXO, specifically engineered for targeting the HER2 receptor. Peptides are known for their high specificity and targeting ability, as well as their low immunogenicity and toxicity. Additionally, they offer efficient membrane internalization and are straightforward to chemically synthesize and modify [50-54].

To synthesize HER2PEP-MSN-DOXO, we utilized MSU-type nanoparticles as the starting materials, synthesizing them following the previously described procedure, using Triton-X as surfactant and TEOS as the silica source. Following the characterization of the synthesized MSNs through SEM, XRD, and TGA, the external surfaces of the mesoporous silica nanoparticles (MSNs) were functionalized with APTES to introduce aminopropyl groups (AP-MSN). These groups facilitated the conjugation of the targeting peptide through the formation of an amide bond, which occurred between the amino group on the nanoparticle surface and the carboxyl group of the C-terminal residue of the peptide.

Fmoc-HER2PEP-MSN was obtained by reacting Fmoc-HER2PEP with AP-MSN in a 1:1 (v/v) mixture of dichloromethane and DMF, using DIC as the condensing agent and DIPEA as the base (Scheme 3).

The peptide was anchored to the nanoparticles in two loading steps to ensure a more efficient functionalization of the MSN external surface with HER2PEP.

Thermogravimetric analysis of the sample before and after functionalization with Fmoc-HER2PEP showed a 12.91% increase in the organic compound mass.

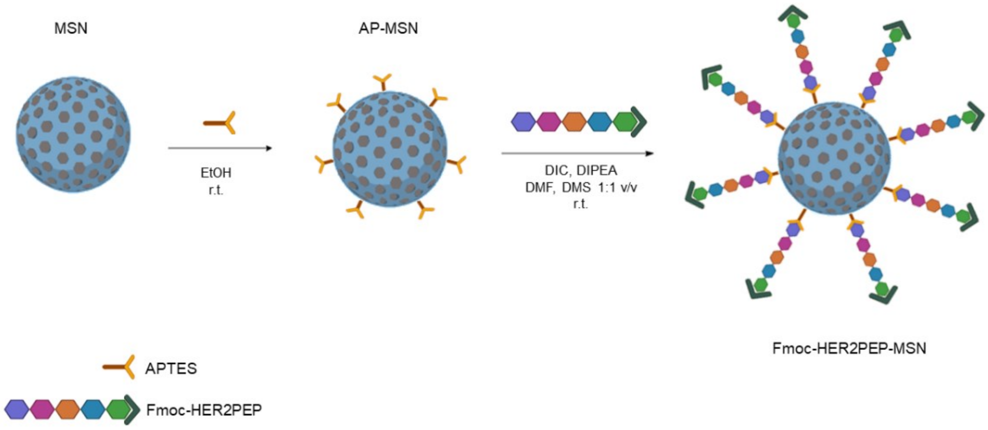

Scheme 3. Synthesis of Fmoc-HER2PEP-MSN.

In the FT-IR spectrum of Fmoc-HER2PEP-MSN (red curve, Figure 17), a broad band at 1668 cm^{-1} indicates the stretching of carbonyl groups of both the peptide amide bonds and the amide bond linking the peptide to the MSN surface. Additionally, bands at 1539 cm^{-1} and 1451 cm^{-1} were observed, corresponding to N-H bending and C-N stretching, respectively. This pattern is consistent with the spectrum of the Fmoc-HER2PEP peptide (black curve, Figure 17) and is not visible in the AP-MSN spectrum (blue curve, Figure 17). Moreover, in the range of 3000-3100 cm^{-1}, both spectra (Fmoc-HER2PEP-MSN and Fmoc-HER2PEP) display similar bands, indicating the stretching of Csp^2-H bonds in the aromatic systems of the Fmoc group and amino acids with aromatic side chains. The presence of these bands confirms the successful loading of the peptide onto the external surface of the mesoporous silica nanoparticles.

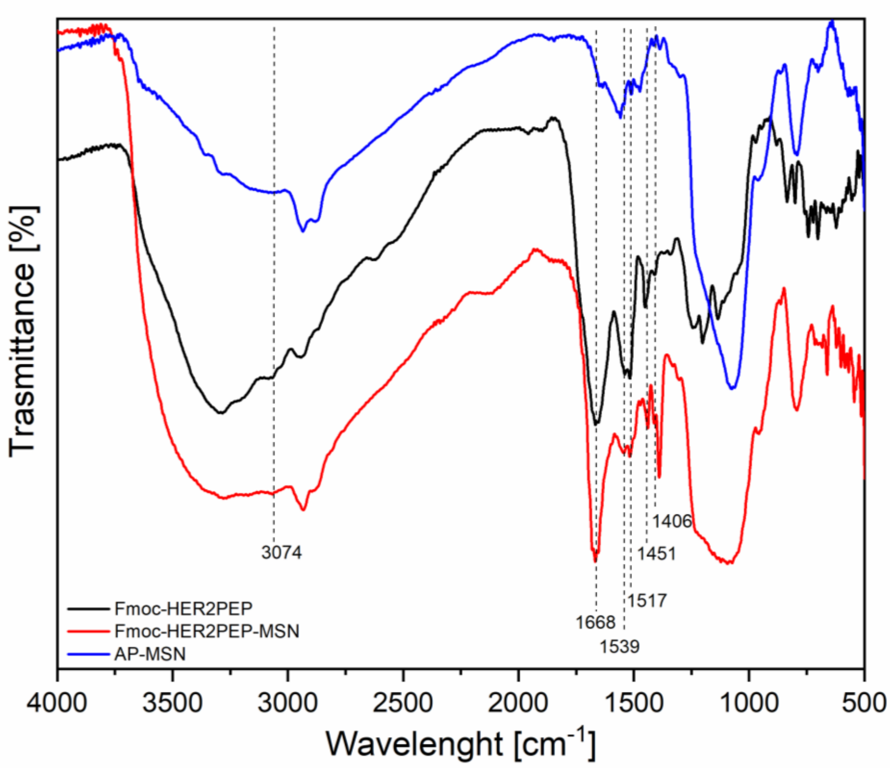

Figure 17. FT-IR spectra of Fmoc-HER2PEP (black), Fmoc-HER2PEP-MSN (red), and AP-MSN (blue).

In the next step, the surfactant was removed from the internal pores of the nanoparticles by extraction with distilled water, resulting in the Fmoc-HER2PEP-MSN-EXT sample. This sample was then functionalized with APTES to introduce amino groups onto the inner pore walls of the MSNs, enabling the conjugation of the succinic acid hydrazide linker (SAH) through an amide bond (Scheme 4).

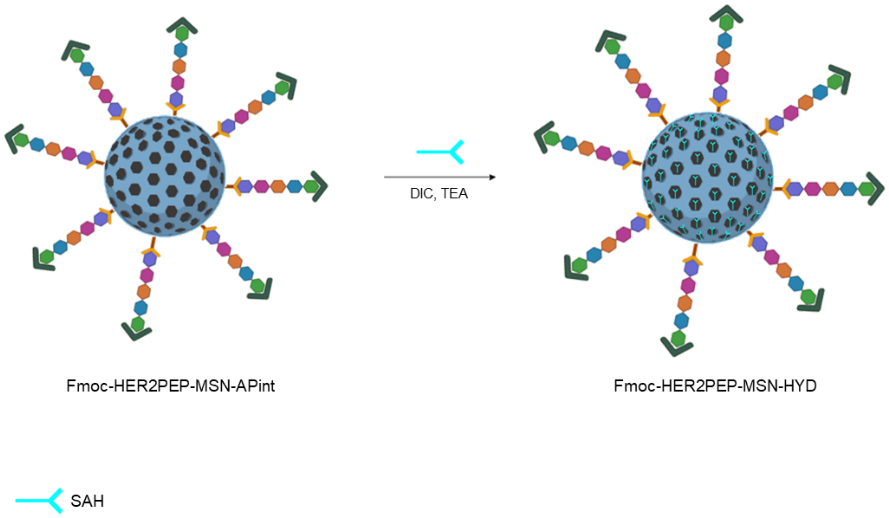

Scheme 4. Synthesis of Fmoc-HER2PEP-MSN-HYD.

Subsequently, doxorubicin was conjugated to the hydrazide-modified nanoparticles (Fmoc-HER2PEP-MSN-HYD) via the formation of a hydrazone bond, resulting in Fmoc-HER2PEP-MSN-DOXO (Scheme 5).

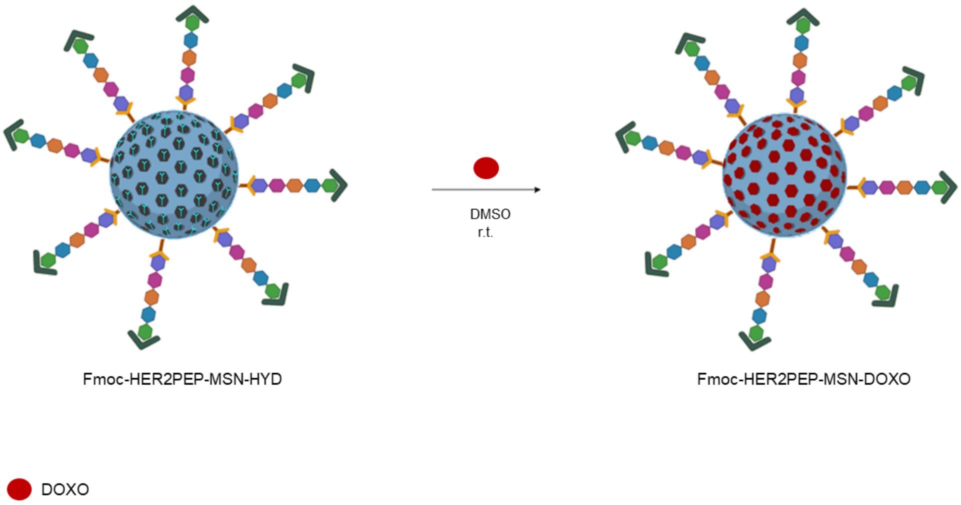

Scheme 5. Synthesis of Fmoc-HER2PEP-MSN-DOXO.

The final prototype, HER2PEP-MSN-DOXO, was obtained by removing the Fmoc protecting group from the N-terminal amine function of the peptide ligand using a 20%

(v/v) piperidine solution in DMF (Scheme 6). The resulting HER2-PEP-MSN-DOXO system was analyzed using FT-IR spectroscopy and TGA.

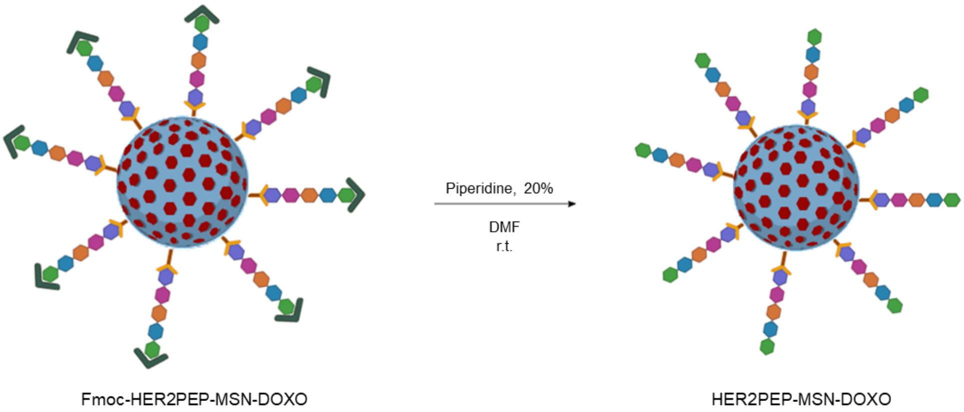

Scheme 6. Synthesis of HER2PEP-MSN-DOXO.

TGA analysis showed a doxorubicin loading content of 2.26%. The FT-IR analysis of HER2-PEP-MSN-DOXO did not reveal appreciable differences compared to the analysis of the FMOC-HER2-PEP-MSN system without DOXO, as the characteristic bands of doxorubicin overlap with those of the targeting peptide.

The biocompatibility and efficacy of HER2PEP-MSN-DOXO and vehicle alone (HER2PEP-MSN) were first investigated on tumor and normal cell models, expressing or not HER2. The effect of MSNs on cell proliferation was evaluated on human HER2+ SKBR3 breast cancer cell line, while the HER2- MDA-MB-468 (triple negative breast cancer) and MCF10A (human normal mammary epithelial) cell lines were used as negative controls, since they do not express the receptor (Figure 18A).

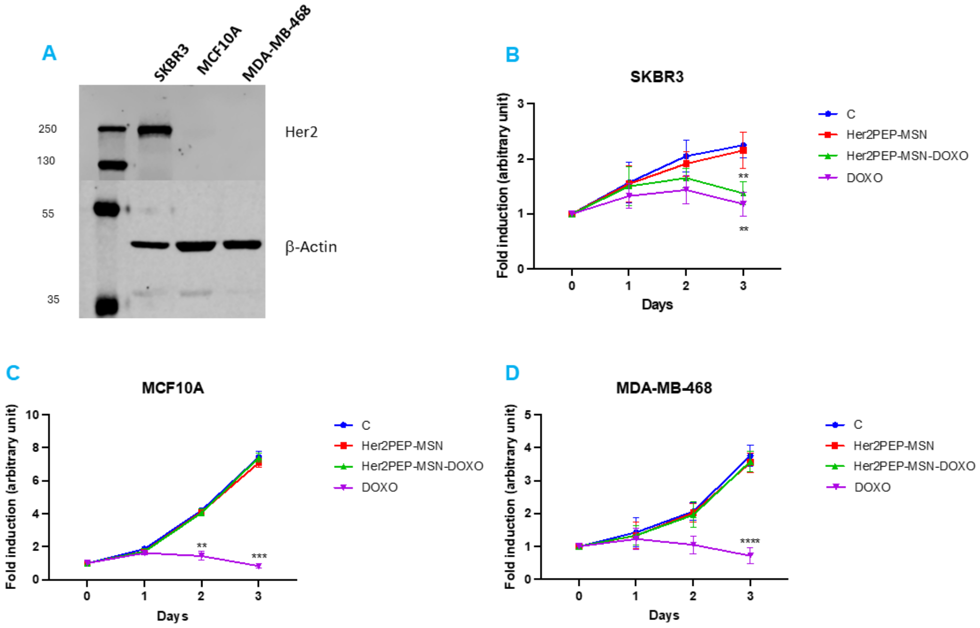

Figure 18. HER2PEP-MSN-DOXO selectively kill HER2-expressing cells. (A) 50 μg of total protein lysates of indicated cell lines were loaded and subjected to WB analysis for Her2 detection. β-actin was used as loading control. HER2PEP-MSN-DOXO induce death in HER2+ SKBR3 breast cancer cells (B), but not in HER2- normal breast epithelial MCF10A cells (C), nor in MDA-MB-468 triple negative breast cancer cells (D). Cells were treated for 1h with HER2PEP-MSN-DOXO or left untreated (C = control) and then harvested and counted at indicated time points. HER2PEP-MSN was used as negative control and the free drug DOXO as positive control (** $p \leq 0.05$, *** $p \leq 0.001$, **** $p \leq 0.0001$).

HER2PEP-MSN-DOXO significantly inhibited cell proliferation of HER2+ SKBR3 cancer cells (Figure 18B), while did not affect the growth of HER2- MCF10A normal cells (Figure 18C). Notably, a similar lack of effect was observed in HER2- MDA-MB-468 triple negative breast cancer (Figure 18D), very likely due to the lack of HER2 receptor on these cells. Conversely, free DOXO was not selective and was toxic for all cell lines tested, independently of their HER2 expression (Figure 18B-D), demonstrating how the carried drug loses its toxicity if loaded into MSNs. Moreover, it is worth mentioning that the vehicle per se (HER2PEP-MSN) was not toxic to either normal or cancer cells (Figure 18B-D).

TEM observations confirmed that HER2PEP-MSN-DOXO only enter HER2-expressing cells (red arrows in Figure 19, upper panel), while negligible uptake occurs in HER2- cells (Figure 19A, lower panel), thus preserving them from doxorubicin toxic effect. Immunogold labelling experiments on SKBR3 cells clearly show that HER2PEP-MSN-DOXO uptake occurs through HER2-mediated endocytosis (Figure 19B).

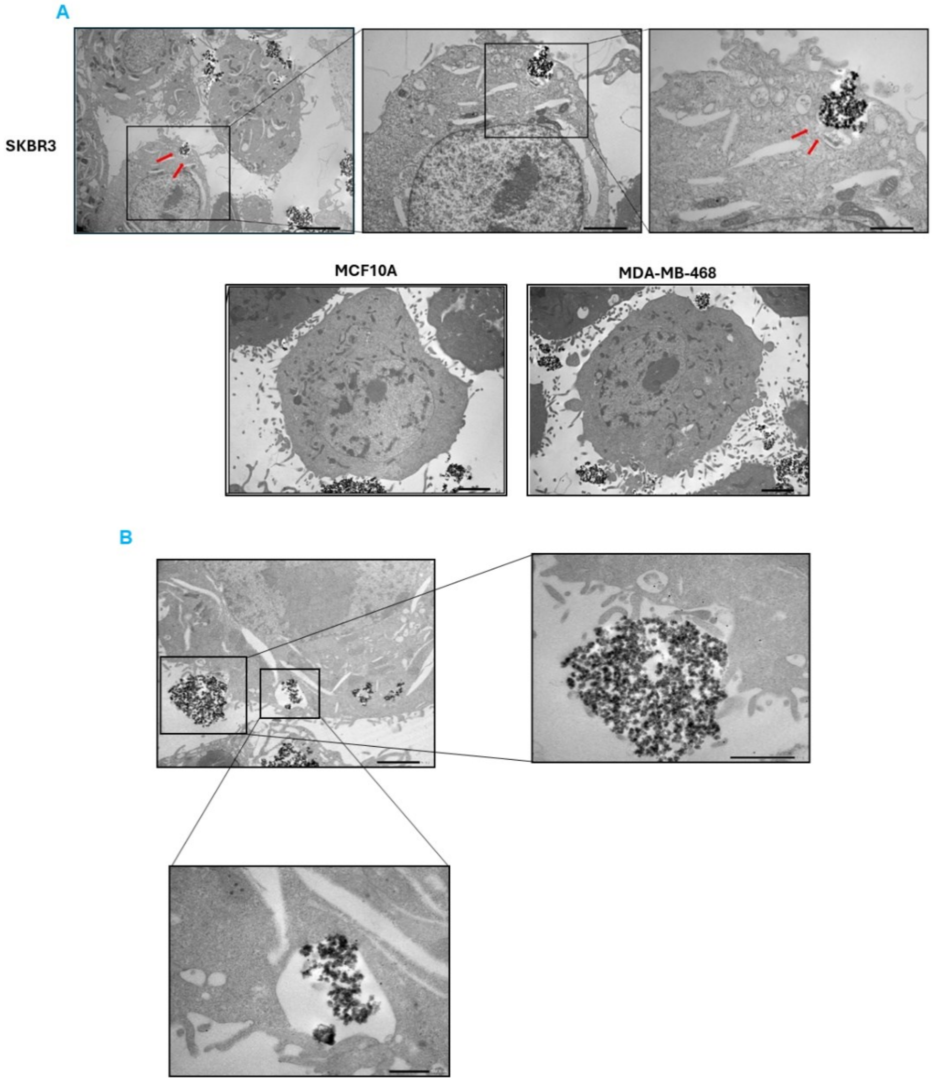

Figure 19. HER2PEP-MSN-DOXO enter HER2+ cells but not HER2- cells. SKBR3 (upper panels), MCF10A and MDA-MB-468 were processed for TEM analysis. MSNs are indicated by red arrows. Original magnification for SKBR3: 1500x, 4000x and 8000x from left to right. For MCF-10 and MDA-MB-468: 3000x magnification. (B) Colloidal-gold immunocytochemistry for HER2 (black dots correspond to HER2 positivity) in SKBR3 cells exposed to HER2PEP-MSN-DOXO for 1h (upper left panel). The HER2 recognition at the cell membrane (upper right panel) and the sequestration in HER2-immunopositive intracellular vesicles (lower panel) are shown. Original magnification: 4000x, 12000x and 15.000x, respectively.

2.3.2 Experimental

MATERIALS AND METHODS

Chemicals and reagents

Reagents were commercially available with analytical grade and used as purchased without further purification. Solvents were purified according to well-known laboratory methods and freshly distilled prior to use. Ultrapure water was distilled with the MilliQ® water, Millipore.

N-Fmoc-L-amino acids, Wang resin (100-200 mesh), N,N,N′,N′-Tetramethyl-O-(1H-benzotriazol-1-yl)uronium hexafluorophosphate (HBTU), diisopropylethylamine (DIPEA), triisopropylsilane (TIS), dimethyl sulfoxide-d6 (DMSO-d6), neutral polyoxyethylene(10) octylphenyl ether (Triton X-100), tetraethylorthosilicate (TEOS), (3-aminopropyl)-triethoxysilane (APTES), Diisopropylcarbodiimide (DIC), Dimethyl sulfoxide (DMSO), were purchased from Sigma-Aldrich. Diethyl ether, trifluoroacetic acid (TFA), N-methylpyrrolidone (NMP), Dichloromethane (DCM), N,N-dimethylformamide (DMF), Hexane and Cyclohexane were purchased from VWR.

Minimum Essential Medium (MEM), RPMI 1640 (1×) Medium, Dulbecco’s Modified Eagle’s Medium (DMEM), DMEM Nutrient Mixture F-12 (DMEM/F-12) and Fetal Bovine Serum (FBS) were from Gibco™ (Life Technologies, Monza MB, Italy). Trypsin-EDTA solution 10×, L-Glutamine, penicillin/streptomycin (pen/strep), D-Glucose, Hepes, Sodium Pyruvate, Non-Essential Amminoacids, Insulin, phosphate-buffered saline (PBS) and Doxorubicin were from Sigma Aldrich (Merck Spa, Milano MI, Italy).

Computational studies

The starting point of the investigations was the crystal structure of HER2 (PDB: 1N8Z) [55] in complex with light chain and heavy chain of antibody Herceptin Fab (HF). The HER2 consists of one chain of 607 amino acids (Chain C) while the antibody includes 214 residues for light chain and 220 residues for heavy chain. The peptide HER2PEP built by GaussView, was used for the docking calculations to bind the receptor with and without antibody.

Docking procedure was followed to obtain the complex of HER2 with the peptide performing calculations using Autodock4. Furthermore, AutoDock tools [56] were used to obtain the PDBQT (Protein Data Bank, Partial Charge (Q), & Atom Type (T)) coordinate files containing the information needed by AutoGrid and AutoDock softwares, namely polar hydrogen atoms, partial charges, correct atom types, as well as details regarding the articulation of the flexible ligand. Gasteiger-Marsili charges [57] were loaded in ADT (Auto Dock Tools). Three different regions of the HER2, the region A (residues 557-561), region B (residues 570-573) and region C (residues 593-603), were targeted during the docking for the examined systems. The center of the grid box was therefore located in every region with a dimension box of 40x40x40 Å^3. For ligand conformational searching the Lamarckian genetic algorithm (LGA) [58] was employed. The docking calculations were carried out obtaining 10 independent runs, population size of 150, random starting position and conformation, local search rate of 0.6 and 2500000 energy evaluations. Final docked poses were clustered using RMSD tolerance of 0.5 Å. The best docking pose was chosen according to the most negative docking score for the next molecular dynamics simulations.

Molecular Dynamics procedure

50 ns MDs were performed for three different systems and HER2:HER2PEP in region A, B and C. The systems were placed in an orthorhombic box with a buffer of 10 Å from the protein, containing the water molecules buffer using TIP3P water model [59] and with counter-ions to make the total charge zero. The general AMBER force field ff14SB [60] force field were used for treating peptide and proteins.

The solvated systems of peptide three bounded-forms of HER2:HER2PEP were first minimized and relaxed by applying positional harmonic constraints on all atoms (50 kcal mol^{-1} $Å^2$) using 5000 steps of steepest descent (SD), followed by 5000 steps of conjugate gradient (CG). In second minimization step, the entire system was released unconstrained and then a progressive heating was performed up to 300 K for 50 ps, followed by 5 ns at 300 K using Langevin thermostat in NVT ensemble. The system was also maintained at a constant pressure using NPT ensemble at 1 bar pressure using the Berendsen barostat with a time constant $\tau p = 2.0$ ps. The production phase for each complex was performed for 50 ns of MDs selecting an integration step of 2 fs, the SHAKE algorithm coupling (in all simulations, including preparation simulations) the Particle Mesh Ewald (PME) summation method. Electrostatic potential and long-range electrostatic interactions were calculated with cut-off distance 12 Å. GROMACS package was used to run the MDs [61]

In order to select different representative conformations of the system, root-mean square deviation (RMSD) based clustering of the whole trajectory was performed using the agglomerative bottom-up approach available in Amber16 tools [62]. After removing overall rotations and translations by RMS fitting the Cα atoms' positions of the trajectory, the average linkage clustering algorithm was applied, identifying 10 representative conformations of the protein.

Molecular Dynamics Analysis

Root-mean-square deviation (RMSD), root mean square fluctuation (RMSF), hydrogen (H)-bond analysis, RMSD-based clustering of MD trajectories, analysis of the distances and contacts were performed using cpptraj module of AmberTools 16 [63].

MM-P/GBSA

Binding free energies between the receptor investigated and the peptide were calculated by solving the linearized Poisson–Boltzmann equation using the Molecular Mechanics Poisson–Boltzmann and Generalized Born surface area (MM-PBSA) methods. The MM-P/GBSA calculation was carried out using the MMPBSA.py [64] module of AMBER16. [63] 200 snapshots from the 50 ns stable MD production trajectory of each complex were utilized for calculation. The value of the *igb* flag equal to 5, associated to a salt concentration of 0.1 M, was used.

SYNTHESIS OF FMOC-HER2PEP

Microwave assisted peptide synthesis protocol

The peptide chain was assembled using a CEM-Liberty microwave-assisted automated synthesizer.

The synthesis scale was 0.25 mmol. In the 50 mL bottles, the Fmoc-L-AA-OH (0.2 mmol) amino acids were dissolved in DMF. Subsequently, solutions containing 20% DIPEA in NMP, the HBTU coupling reagent dissolved in DMF, and 20% piperidine in DMF were prepared.

Fmoc-L-amino acid - Wang resin (0.79 mmol) was introduced into the reaction vessel and swollen in DMF (5 ml) for 30 min. Then, the reaction vessel was placed in the Discovery microwave and the temperature adjusted via optical fiber probe.

The loading of the resin with N-Fmoc-α-amino acids and all coupling steps were performed in DMF, and in the presence of HBTU (5 equivalents) and DIPEA (10 equivalents) for 5 min at 75 °C for all amino acids.

The Fmoc protecting group was removed by treatment of the resin with a 20% solution of piperidine in DMF (v/v) (10 ml).

Deprotection was performed in two steps with an initial deprotection of 30 sec, at 45 °C, followed by 3 min at 75 °C. Between each step, the resin was washed thoroughly with DMF. The completed peptide was washed with DMF and DCM.

The peptide was cleaved from the resin using a mixture of TFA, water, and TIS (9.5/0.25/0.25 by volume) for 30 min, the temperature was maintained at 38 °C via optical fiber control.

Peptide analysis

^{1}H and ^{13}C NMR spectra were recorded on a Bruker Avance 300 instrument at 300 MHz and 75 MHz, respectively. Spectroscopic analysis was performed at 293 K on diluted solutions of each compound by using DMSO-d6 as the solvent. Chemical shifts (δ) are reported in ppm. Coupling constants (*J*) are reported in Hertz (Hz). LC-MS analysis was carried out using an HPLC instrument (Agilent Technologies, California, USA) coupled to a QTOF mass spectrometer fitted with a ESI operating in positive ion mode. Chromatographic separation was achieved using a LC C18 preparative column (Agilent 5, C18, 50 x 10.0 mm) at 25 °C. The mobile phases consisted of eluent A (water) and eluent B (acetonitrile) These eluents were delivered at a flow rate of 0.4 mL/min with a linear gradient program as follows: 5% B from 0 to 3.0 min, 5–70% B from 3.0 to 7.0 min, 70–100% B from 7.0 to 10.0 min. Signal was acquired at 270 nm wavelength.

SYNTHESIS OF HER2PEP-FUNCTIONALIZED MESOPOROUS SILICA NANOPARTICLES (HER2PEP-MSN)

Synthesis of Mesoporous Silica Nanoparticles (MSNs)

The surfactant Triton X-100 (21 g) was dissolved in ultrapure water (230 g) at room temperature, with stirring for about four hours. To create two phases, a solution of TEOS (22 g) in cyclohexane (9.8 g) was slowly added along the vessel (molar composition TEOS: Cyclohexane: Triton X-100: H2O was 1: 1.08: 0.32: 120, respectively).

The synthesis was carried out at room temperature. The upper phase was removed, and the resulting precipitate was collected by filtration and washed three times with ultrapure water. Finally, the sample was dried in the oven at 70 °C for 24 h, resulting in a white powder was obtained.

Synthesis of Amine Functionalized MSNs (AP-MSN)

The nanoparticles' surface was coated with aminopropyl groups using (3-aminopropyl)triethoxysilane (APTES).

A solution of APTES in ethanol (33 mL, 0.85 g/mL) was added to a suspension of MSNs (8 g) in ethanol (27.85 mL). The mixture was stirred at room temperature for 48 h. Afterward, the suspension was filtered and washed once with ethanol and twice with ultrapure water. The resulting sample (AP-MSN) was dried in an oven at 70 °C for 24 h.

Synthesis of Fmoc-HER2PEP-MSN

Firstly, Fmoc-HER2PEP (0.35 mmol, 1 equivalent) was dissolved in a mixture of dry DCM and DMF (10 ML, 1:1 v.v) with DIC (0.7 mmol, 2 equivalents) and DIPEA (0.7 mmol, 2 equivalents) to activate the carboxylic function. The mixture was left to stir for 2 h at room temperature. Subsequently, AP-MSN powder (1 g) was added, and the reaction was carried out for 48 h, at room temperature. The suspension was then filtered and washed three times with dry DCM. The so-obtained nanoparticles were dried at room temperature.

A second step was performed by adding 10% of Fmoc-HER2PEP amount used for the first loading step. The reaction was left for 48 h at room temperature under gentle stirring. The sample was filtered and washed with the same procedure as described for the first loading. Subsequently, the surfactant within the pores was removed using 1 g of Fmoc-HER2PEP-MSN nanoparticles in 0.33 L of ultrapure water at room temperature. After 3 steps of extractions, Fmoc-HER2PEP-MSN-EXT sample was centrifuged and washed with dry 1,4-dioxane and DCM, then dried at 45 °C.

CONJUGATION OF DOXO TO HER2PEP-MSN USING PH-SENSITIVE HYDRAZONE BOND

Synthesis of HER2PEP-MSN-DOXO

Synthesis of Fmoc-HER2-MSN-APint

The inner pores of Fmoc-HER2PEP-MSN-EXT were functionalized with (3-Aminopropyl)triethoxysilane (APTES) to introduce amino groups, which are essential for subsequent drug anchoring via a hydrazone bond. To achieve this, Fmoc-HER2PEP-MSN-EXT (0.03 g/mL) was suspended in dry 1,4-dioxan, followed by the addition of APTES (2.2 g per gram of MSNs). After stirring for 18 h, the mixture was filtered, and the solid residue was washed with dry DCM. The resulting nanoparticles, Fmoc-HER2PEP-MSN-APint, were then dried at room temperature.

Synthesis of Succinic Acid Monohydrazide Linker

Succinic anhydride (1 g, 10 mmol) and DMAP (10 mg, 0.08 mmol) were dissolved in DCM (50 mL). Subsequently, a solution containing hydrazine monohydrate (0.320 g, 6 mmol) in DCM (10 mL) was added to the mixture dropwise under vigorous stirring at room temperature. After 10 h, the solvent was evaporated under reduced pressure, resulting in a white solid (1.1 g).

^{1}H NMR (300 MHz, DMSO-d6) δ: 11.80 (sbroad, 1H, COOH), 9.76 (s, 1H, CONH), 2.48-2.40 (m, 2H, (CH2COOH), 2.40-2.28 (m, 2H, (CH2CONHNH2).

^{13}C NMR (75 MHz, DMSO-d6) δ: 173.95, 170.36, 29.32, 28.51

Synthesis of Fmoc-HER2PEP-MSN-HYD

Succinic acid monohydrazide (0.218 g, 1.65 mmol) was dissolved in DMSO (20 mL), then DIC (0.256 mL, 1.65 mmol) and triethylamine (0.230 mL, 1.65 mmol) were added. After 1 h, a suspension of Fmoc-HER2PEP-MSN-APint in DMSO (0.05 g/mL) was added to the reaction mixture. The reaction was stirred at room temperature for 24 h. After that, the reaction mixture was filtered, and a second loading cycle was performed. Following this, the reaction mixture was filtered, and a second loading cycle was performed under the same conditions for another 24 h at room temperature. The mixture was then filtered, and the recovered powder was washed with DMSO and diethyl ether to afford Fmoc-HER2PEP-MSN-HYD (2 g).

Drug Loading

A solution of doxorubicin hydrochloride in DMSO (0.004 g/mL) was added to a suspension of Fmoc-HER2PEP-MSN-HYD in DMSO (0.015 g/mL). The pH was adjusted to approximately 5 by adding a few drops of acetic acid. The reaction mixture was stirred at room temperature under an inert atmosphere for 24 h. Subsequently, the nanoparticles were filtered and washed with DMSO. To achieve a higher drug loading, the resulting solid was resuspended in DMSO, and a second drug loading was carried out under the same conditions. Then, the reaction mixture was filtered and thoroughly washed with DMSO, dry 1,4-dioxane, and dry dichloromethane. The obtained nanomaterial

Fmoc-HER2PEP-MSN-DOXO was stored in sealed containers at -20 °C, under dry conditions and protected from light.

The amount of doxorubicin loaded (2.26%) onto the nanoparticles was determined by TGA and confirmed by UV-VIS spectroscopy (λabs = 481 nm).

Deprotection of Fmoc-HER2PEP-MSN-DOXO

The Fmoc group was removed from the N-terminal function of the targeting peptide using a 20% piperidine solution in DMF (30 mL). This deprotection process was carried out in a single 90-minute cycle. After the cycle, the resulting HER2PEP-MSN-DOXO nanoparticles were filtered and washed sequentially with DMF, dry 1,4-dioxane, and dry DCM. The nanoparticles were then dried at room temperature and stored in sealed containers at -20 °C under an inert atmosphere to prevent degradation of the drug.

The peptide structure and experimental data are not included at this time, as they may be part of a future patent application for the HER2PEP-MSN-DOXO prototype.

Cell Cultures and Treatments

Human HER2 positive (HER2+) breast cancer SKBR3, triple negative breast cancer MDA-MB-468 and HER2 negative (HER2-) human normal mammary epithelial MCF10A cells lines were purchased from ATCC, where they were authenticated. Cells were stored according to supplier’s instructions and used within 6 months after frozen aliquot resuscitations. Cells were purchased from ATCC and transferred to our laboratory at passage n = 3 and handled as described above.

SKBR3 were cultured in RPMI 1640 (1x) Medium, MDA-MB-468 in DMEM/F12, and MCF10A in DMEM/F12 containing 5% horse serum (Gibco), 20ng/mL EGF, 10 ug/mL human insulin, 0.5 mg/mL hydrocortisone, 100 ng/mL cholera toxin. All media contained

10% FBS, 100 IU/mL pen/strep and 0.2 mM L-Glutamine (all from Gibco, Thermo Fisher Scientific Inc.). All the other listed reagents were purchased from Sigma-Aldrich (Merck KGaA, Darmstadt, Germany).

Mycoplasma negativity was tested monthly (PlasmoTest, Invivogen, Aurogene, Rome, Italy). For cell treatments, MSNs were resuspended in serum-free media (SFM) on a magnetic stirrer, and a ratio of 1 μg MSNs/10^5 cells was used on the basis of titration experiments and added to the cells for 1 h. Free DOXO was added, as positive control, in amounts (in μg) corresponding to the % (in weight) of DOXO carried by HER2PEP-MSN-DOXO (1%).

Cell Proliferation Assays

MSNs effect on cell proliferation was assessed by trypan blue exclusion assay. Cells were seeded in triplicates for each condition, synchronized in SFM for 24 h and then treated for 1 h with 1 μg MSNs/10^5 cells. Cells were then switched to fresh growth medium (GM) plus 1% FBS and counted after 72 h. Cell viability was determined by Countess® II Automated Cell Counter (Invitrogen, Life Technology), according to supplier's instructions.

Western Blotting (WB) Assay

HER2 proteins expression were assessed by WB using total protein lysates from tested cell lines. 50 μg of denatured (for HER2 detection) proteins were run on an 10% polyacrylamide gel. The following primary Abs were employed: HER2/ErbB2 (D8F12, Cell Signaling, Inc. Danvers, Massachusetts,MA, USA), β-Actin (sc-69879, Santa Cruz Biotechnology, Inc.). IRDye (LI-COR Corporate, NE, USA) were used as secondary Abs. Images were acquired with the Odyssey FC Imaging System (LI-COR Corporate).

Transmission electron microscopy (TEM) and electron immunocytochemistry

Conventional TEM analysis and electron immunocytochemistry were conducted as previously described (2023-Mater. Chem. Front-MSNs-BTZ in MM). Cells were treated as described for growth experiments and harvested after 1h of treatment to detect MSNs uptake. Samples have been routinely fixed, dehydrated, and resin embedded using heat polymerization. Ultrathin sections were collected on copper grids and contrasted using both lead citrate and uranyl acetate.

For indirect immunolabeling, grids were floated on drops of 1% bovine serum albumin (BSA) in PBS containing 0.02-M glycine at room temperature for 30 min to reduce nonspecific binding. Sections were then incubated with a rabbit polyclonal antibody against HER2/ErbB2 (D8F12, Cell Signaling, Inc. Danvers, Massachusetts, MA, USA) at 4 °C overnight. The grids were then transferred to 50μL drops of secondary antibody conjugated to 10-nm gold particles for 1 h, at room temperature. Observations were performed under a Jeol JEM-1400 Plus electron microscope (Jeol Ltd., Tokyo, Japan) operating at 80 kV.

2.4 Conclusion

In this work, a mesoporous silica-based nanosystem (FOL-MSN-DOXO) was designed and synthesized for the targeted delivery and controlled release of the antineoplastic drug doxorubicin.

Foli acid grafted on the external MSN surface allowed recognition and internalization by cancer cells overexpressing the folate receptor (FR+). Inside the intracellular organelles, the drug, anchored within the silica pores via a pH-sensitive hydrazone linkage, was released in response to the acidic tumor microenvironment.

In vitro investigations conducted on both FR+ and FR- cell models demonstrated that FOL-MSN-DOXO was highly specific towards FR+ cancer cells, without significantly affecting the vitality of FR- normal cells. Furthermore, the *in vitro* compatibility and safety of the nanovehicle were confirmed. The uptake of FOL-MSN-DOXO occurred exclusively in FR+ tumor cells through FR-mediated endocytosis, confirming the role of folic acid in mediating cellular uptake process.

Encouraged by these results, we advanced to a more targeted DOXO MSN-based delivery system by substituting the folic acid targeting ligand with a peptide specifically designed to bind to HER2, a highly selective marker for breast cancer. The new HER2PEP-MSN-DOXO prototype efficiently delivered doxorubicin to HER2-overexpressing cancer cells through HER2-mediated endocytosis. HER2PEP-functionalized MSNs significantly inhibited cell proliferation in HER2+ breast cancer cells, while HER2- normal cells and HER2- breast cancer cells remained unaffected. Notably, the nanocarrier was not toxic to all tested cell lines.

These promising findings demonstrate that the anticancer drug doxorubicin (DOXO) significantly reduces its toxicity when delivered through the developed mesoporous silica-based nanodevices, resulting in improved efficacy and safety of cancer treatments. The HER2-targeting MSN-based nanotechnology offers increased specificity, representing a significant advancement in targeted breast cancer therapies.

References

1. Arcamone, F., Cassinelli, G., Fantini, G., Grein, A., Orezzi, P., Pol, C., Spalla, C. Adriamycin, 14-Hydroxydaimomycin, a New Antitumor Antibiotic from S. Peucetius var. caesius. Biotechnology and Bioengineering, 1969, 11, 1101-1110.
2. Alghorabi, A. A., Kabel, A. M., Elmaaboud, M. Doxorubicin: insights into dynamics, clinical uses and adverse effects. J. Cancer Res. Treat, 2019, 7(1), 17-20.
3. Denel-Bobrowska, M., Marczak, A. Structural modifications in the sugar moiety as a key to improving the anticancer effectiveness of doxorubicin. Life Sciences, 2017, 178, 1-8.
4. Pérez-Arnaiz, C., Busto, N., Leal, J. M., García, B. New insights into the mechanism of the DNA/doxorubicin interaction. The Journal of Physical Chemistry B, 2014, 118(5), 1288-1295.
5. Chatterjee, K., Zhang, J., Honbo, N., Karliner, J. S. Doxorubicin cardiomyopathy. Cardiology, 2010, 115(2), 155-162.
6. Injac, R., & Strukelj, B. Recent advances in protection against doxorubicin-induced toxicity. Technology in cancer research & treatment, 2008, 7(6), 497-516.
7. Alhowail, A. H., Bloemer, J., Majrashi, M., Pinky, P. D., Bhattacharya, S., Yongli, Z., ... & Suppiramaniam, V. Doxorubicin-induced neurotoxicity is associated with acute alterations in synaptic plasticity, apoptosis, and lipid peroxidation. Toxicology mechanisms and methods, 2019, 29(6), 457-466.
8. Chen, T., Shen, H. M., Deng, Z. Y., Yang, Z. Z., Zhao, R. L., Wang, L., Feng, Z.P., Li, W. H., Liu, Z. J. A herbal formula, SYKT, reverses doxorubicin-induced myelosuppression and cardiotoxicity by inhibiting ROS-mediated apoptosis. Molecular Medicine Reports, 2017, 15(4), 2057-2066.
9. Curigliano, G., Cardinale, D., Dent, S., Criscitiello, C., Aseyev, O., Lenihan, D., Cipolla, C. M. Cardiotoxicity of anticancer treatments: epidemiology, detection, and management. CA: a cancer journal for clinicians, 2016, 66(4), 309-325.
10. Cardinale, D., Biasillo, G., Cipolla, C. M. Curing cancer, saving the heart: a challenge that cardioncology should not miss. Current cardiology reports, 18,2016, 1-10.
11. Bloom, M. W., Hamo, C. E., Cardinale, D., Ky, B., Nohria, A., Baer, L., Skopicki, H., Lenihan D. J., Gheorghiade, M., Lyon, A.R., Butler, J. Cancer therapy–related cardiac dysfunction and heart failure: part 1: definitions, pathophysiology, risk factors, and imaging. Circulation: Heart Failure, 2016, 9(1), e002661.
12. Nitiss, K. C., Nitiss, J. L. Twisting and ironing: doxorubicin cardiotoxicity by mitochondrial DNA damage. Clinical Cancer Research, 2014, 20(18), 4737-4739.
13. Zamorano, J. L., Lancellotti, P., Rodriguez Munoz, D., Aboyans, V., Asteggiano, R., Galderisi, M.,Habib, G., Lenihsn, D. J., Lip, G. Y. H., Lyon, A.R., Fernandez, T. L., Mohty, D., Piepoli, M.F., Tamargo, J., Torbicki, A., Suter, T. M. 2016 ESC Position Paper on cancer treatments and cardiovascular toxicity developed under the auspices of the ESC Committee for Practice Guidelines: The Task Force for cancer treatments and cardiovascular toxicity of the European Society of Cardiology (ESC). European Heart Journal, 2016, 37(36), 2768-2801.
14. Shams, F., Golchin, A., Azari, A., Mohammadi Amirabad, L., Zarein, F., Khosravi, A., Ardeshirylajimi, A. Nanotechnology-based products for cancer immunotherapy. Molecular Biology Reports, 2022, 1-24.
15. Wakaskar, R. R. Promising effects of nanomedicine in cancer drug delivery. Journal of drug targeting, 2018, 26(4), 319-324.

16. Barenholz, Y. C. Doxil®—The first FDA-approved nano-drug: Lessons learned. Journal of controlled release, 2012, 160(2), 117-134.
17. Gu, W., Andrews, G. P., Tian, Y. Recent Clinical Successes in liposomal nanomedicines. International Journal of Drug Discovery and Pharmacology, 2023, 2(1), 52-59.
18. Anon. Celsion Announces Enrollment Completion Pivotal Phase III OPTIMA Study of ThermoDox® in Primary Liver Cancer–Duke OTC. https://investor.celsion.com/news-releases/news-release-details/celsion-announces-enrollment-completion-pivotal-phase-iii-optima.
19. Tang, F., Li, L., & Chen, D. (2012). Mesoporous silica nanoparticles: synthesis, biocompatibility and drug delivery. Advanced materials, 24(12), 1504-1534.
20. Yu, L., Lin, H., Lu, X., & Chen, Y. Multifunctional mesoporous silica nanoprobes: Material chemistry–based fabrication and bio-imaging functionality. Advanced Therapeutics, 2018, 1(8), 1800078.
21. Manzano, M., & Vallet-Regí, M. New developments in ordered mesoporous materials for drug delivery. Journal of Materials Chemistry, 2010, 20(27), 5593-5604.
22. Hu, Y., Zhi, Z., Zhao, Q., Wu, C., Zhao, P., Jiang, H., Jiang, T., Wang, S. 3D cubic mesoporous silica microsphere as a carrier for poorly soluble drug carvedilol. Microporous and Mesoporous Materials, 2012, 147(1), 94-101.
23. Mohammadpour, R., Cheney, D. L., Grunberger, J. W., Yazdimamaghani, M., Jedrzkiewicz, J., Isaacson, K. J., Dobrovolskaia, M.A., Ghandehari, H. One-year chronic toxicity evaluation of single dose intravenously administered silica nanoparticles in mice and their Ex vivo human hemocompatibility. Journal of controlled release, 2020, 324, 471-481.
24. Kang, Y., Sun, W., Li, S., Li, M., Fan, J., Du, J., Liang, X.-J. Peng, X. Oligo hyaluronan-coated silica/hydroxyapatite degradable nanoparticles for targeted cancer treatment. Advanced Science, 2019, 6(13), 1900716.
25. Mal, A., Prabhuraj, R. S., Malhotra, R., Valvi, S. K., Ingle, A., Srivastava, R., De, A., Bandyopadhyaya, R. pH-responsive sustained delivery of doxorubicin using aminated and PEGylated mesoporous silica nanoparticles leads to enhanced antitumor efficacy in pre-clinical orthotopic breast cancer model. Journal of Drug Delivery Science and Technology, 2022, 77, 103800.
26. Li, M., Zhang, W. K., Benvin, N. M., Zhou, X., Su, D., Li, H., Wang, S., Micheilidis, I.E., Tong, L., Li, X., Yang, J. Structural basis of dual Ca^{2+}/pH regulation of the endolysosomal TRPML1 channel. Nature structural & molecular biology, 2017, 24(3), 205-213.
27. Hosonuma, M., & Yoshimura, K. Association between pH regulation of the tumor microenvironment and immunological state. Frontiers in Oncology, 2023, 13.
28. Czupiel, P., Delplace, V., & Shoichet, M. Nanoparticle delivery of a pH-sensitive prodrug of doxorubicin and a mitochondrial targeting VES-H8R8 synergistically kill multi-drug resistant breast cancer cells. Scientific Reports, 2020, 10(1), 8726.
29. Etrych, T., Šírová, M., Starovoytova, L., Říhová, B., Ulbrich, K. HPMA copolymer conjugates of paclitaxel and docetaxel with pH-controlled drug release. Molecular pharmaceutics, 2010, 7(4), 1015-1026.
30. Bae, Y., Fukushima, S., Harada, A., & Kataoka, K. Design of environment-sensitive supramolecular assemblies for intracellular drug delivery: Polymeric micelles that are responsive to intracellular pH change. Angewandte Chemie, 2003, 115(38), 4788-4791.
31. De Santo, M., Giovinazzo, A., Fava, M., Mazzotta, E., De Napoli, I. E., Greco, M., Comandé, A., Argurio, Perrotta, I., P., Davoli, M., Tagarelli, A., Elliani, R., Granato, T., Nicolini, G., Semperboni, S., Ballarini, E., Crocamo, C., Cavaletti, G., Lombardo, D., Sisci, D., Morelli, C., Leggio, A., Pasqua, L. Engineered mesoporous silica-based

nanoparticles as smart chemotherapy nanodevice for bortezomib administration. Materials Chemistry Frontiers, 2023, 7(2), 216-229.

32. Lu, Y., & Low, P. S. Folate-mediated delivery of macromolecular anticancer therapeutic agents. Advanced drug delivery reviews, 2002, 54(5), 675-693.
33. Geng, L., Wang, Z., Jia, X., Han, Q., Xiang, Z., Li, D., Yang, X., Zhang, D., Bu, X., Wang, W., Hu, Z., Fang, Q. HER2 targeting peptides screening and applications in tumor imaging and drug delivery. Theranostics, 2016, 6(8), 1261.
34. Augustine, R., Hasan, A., Primavera, R., Wilson, R. J., Thakor, A. S., Kevadiya, B. D. Cellular uptake and retention of nanoparticles: Insights on particle properties and interaction with cellular components. Materials Today Communications, 2020, 25, 101692.
35. Depan, D., Shah, J., & Misra, R. D. K. Controlled release of drug from folate-decorated and graphene mediated drug delivery system: Synthesis, loading efficiency, and drug release response. Materials Science and Engineering: C, 2011, 31(7), 1305-1312.
36. Kovacs, E., Zorn, J. A., Huang, Y., Barros, T., Kuriyan, J. A structural perspective on the regulation of the epidermal growth factor receptor. Annual review of biochemistry, 2015, 84, 739-764.
37. Citri, A., Yarden, Y. EGF–ERBB signalling: towards the systems level. Nature reviews Molecular cell biology, 2006, 7(7), 505-516.
38. Harari, D., & Yarden, Y. Molecular mechanisms underlying ErbB2/HER2 action in breast cancer. Oncogene, 2000, 19 (53), 6102-6114.
39. Mitri, Z., Constantine, T., O′ Regan, R. The HER2 receptor in breast cancer: pathophysiology, clinical use, and new advances in therapy. Chemotherapy research and practice, 2012, (1), 743193.
40. Gutierrez, C., Schiff, R. HER2: biology, detection, and clinical implications. Archives of pathology & laboratory medicine, 2011, 135(1), 55-62.
41. Iqbal, N., Iqbal, N. Human epidermal growth factor receptor 2 (HER2) in cancers: overexpression and therapeutic implications. Molecular biology international, 2014, (1), 852748.
42. Moasser, M. M. The oncogene HER2: its signaling and transforming functions and its role in human cancer pathogenesis. Oncogene, 2007, 26 (45), 6469-6487.
43. Galogre, M., Rodin, D., Pyatnitskiy, M., Mackelprang, M., Koman, I. A review of HER2 overexpression and somatic mutations in cancers. Critical Reviews in Oncology/Hematology, 2023, 103997.
44. Slamon, D. J., Godolphin, W., Jones, L. A., Holt, J. A., Wong, S. G., Keith, D. E., Levin, W.J., Udove, J., Ullrich, A., Press, M. F. Studies of the HER-2/neu proto-oncogene in human breast and ovarian cancer. Science, 1989, 244(4905), 707-712.
45. Cavallaro, P. A., De Santo, M., Belsito, E. L., Longobucco, C., Curcio, M., Morelli, C., Pasqua, L., Leggio, A. Peptides targeting HER2-positive breast cancer cells and applications in tumor imaging and delivery of chemotherapeutics. Nanomaterials, 2023, 13(17), 2476.
46. Slamon, D. J., Clark, G. M., Wong, S. G., Levin, W. J., Ullrich, A., McGuire, W. L. Human breast cancer: correlation of relapse and survival with amplification of the HER-2/neu oncogene. Science, 1987, 235(4785), 177-182.
47. Cobleigh, M. A., Vogel, C. L., Tripathy, D., Robert, N. J., Scholl, S., Fehrenbacher, L., Wolter, J.M., Paton, V., Shak, S., Lieberman, G., Slamon, D. J. Multinational study of the efficacy and safety of humanized anti-HER2 monoclonal antibody in women who have HER2-overexpressing metastatic breast cancer that has progressed after chemotherapy for metastatic disease. Journal of clinical Oncology, 1999, 17(9), 2639-2639.

48. Cho, H. S., Mason, K., Ramyar, K. X., Stanley, A. M., Gabelli, S. B., Denney Jr, D. W., Leahy, D. J. Structure of the extracellular region of HER2 alone and in complex with the Herceptin Fab. Nature, 2003, 421(6924), 756-760.
49. Satyanarayanajois, S., Villalba, S., Jianchao, L., Lin, G. M. Design, synthesis, and docking studies of peptidomimetics based on HER2–Herceptin binding site with potential antiproliferative activity against breast cancer cell lines. Chemical biology & drug design, 2009, 74(3), 246-257.
50. Craik, D. J., Fairlie, D. P., Liras, S., & Price, D. The future of peptide-based drugs. Chemical biology & drug design, 2013, 81(1), 136-147.
51. Fosgerau, K., & Hoffmann, T. Peptide therapeutics: current status and future directions. Drug Discovery Today, 2015, 20(1), 122-128.
52. Ladner, R. C., Sato, A. K., Gorzelany, J., de Souza, M. Phage display-derived peptides as therapeutic alternatives to antibodies. Drug Discovery Today, 2004, 9(12), 525-529.
53. Wang, L., Wang, N., Zhang, W., Cheng, X., Yan, Z., Shao, G., Wang, X., Wang, R., Fu, C. Therapeutic peptides: current applications and future directions. Signal Transduction and Targeted Therapy, 2022, 7(1), 48.
54. Diao, L., Meibohm, B. Pharmacokinetics and pharmacokinetic–pharmacodynamic correlations of therapeutic peptides. Clinical Pharmacokinetics, 2013, 52, 855-868.
55. Cho, H. S., Mason, K., Ramyar, K. X., Stanley, A. M., Gabelli, S. B., Denney Jr, D. W., & Leahy, D. J. (2003). Structure of the extracellular region of HER2 alone and in complex with the Herceptin Fab. Nature, 421(6924), 756-760.
56. G. M. Morris, R. Huey, W. Lindstrom, M. F. Sanner, R. K. Belew, D. S. Goodsell and A. J. Olson, J. Comp. Chem., 2009, 30, 7. https://doi.org/10.1002/jcc.21256
57. J. Gasteiger and M. Marsili, Tetrahedron, 1980, 36, 3219–3228. https://doi.org/10.1016/0040-4020(80)80168-2.
58. G. M. Morris, D. S. Goodsell, R. S. Halliday, R. Huey, W. E. Hart, R. K. Belew and A. J. Olson, J. Comp. Chem., 1998, 19, 24. https://doi.org/10.1002/(SICI)1096-987X(19981115)19:14<1639:AID-JCC10>3.0.CO;2-BCitations: 8,341
59. Hornak, V.; Abel, R.; Okur, A.; Strockbine, B.; Roitberg, A.; Simmerling, C. Comparison of multiple Amber force fields and development of improved protein backbone parameters. Proteins: Struct., Funct., Genet. 2006, 65 (3), 712−725, DOI: 10.1002/prot.21123.
60. Maier, J. A.; Martinez, C.; Kasavajhala, K.; Wickstrom, L.; Hauser, K. E.; Simmerling, C. ff14SB: Improving the Accuracy of Protein Side Chain and Backbone Parameters from ff99SB. J. Chem. Theory Comput. 2015, 11, 3696−3713, DOI: 10.1021/acs.jctc.5b00255.
61. M. J. Abraham, T. Murtola, R. Schulz, S. Páll, J. C. Smith, B. Hess, E. Lindahl, GROMACS: High performance molecular simulations through multi-level parallelism from laptops to supercomputers 2015, 1 (2), 19–25.
62. D. A. Case, H. M. Aktulga, K. Belfon, I. Y. Ben-Shalom, J. T. Berryman, S. R. Brozell, D. S. Cerutti, T. E. Cheatham III, G. A. Cisneros, V. W. D. Cruzeiro, T. A. Darden, R. E. Duke, G. Giambasu, M. K. Gilson, H. Gohlke, A. W. Goetz, R. Harris, S. Izadi, S. A. Izmailov, K. Kasavajhala, M. C. Kaymak, E. King, A. Kovalenko, T. Kurtzman, T. S. Lee, S. LeGrand, P. Li, C. Lin, J. Liu, T. Luchko, R. Luo, M. Machado, V. Man, M. Manathunga, K. M. Merz, Y. Miao, O. Mikhailovskii, G. Monard, H. Nguyen, K. A. O'Hearn, A. Onufriev, F. Pan, S. Pantano, R. Qi, A. Rahnamoun, D. R. Roe, A. Roitberg, C. Sagui, S. Schott-Verdugo, A. Shajan, J. Shen, C. L. Simmerling, N. R. Skrynnikov, J. Smith, J. Swails, R. C. Walker, J. Wang, J. Wang, H. Wei, R. M. Wolf, X. Wu, Y. Xiong, Y. Xue, D. M. York, S. Zhao, P. A. Kollman, Amber 2016, University of California, San Francisco.

63. D. R.; Roe, T. E. Cheatham, PTRAJ and CPPTRAJ: Software for Processing and Analysis of Molecular Dynamics Trajectory Data. J Chem. Theory Comput. 2013, 9 (7), 3084−3095.
64. B. R., III Miller, T. D., Jr. McGee, J. M. Swails, N. Homeyer, H. Gohlke, A. E. Roitberg, MMPBSA.py: An Efficient Program for End-State Free Energy Calculations. J. Chem. Theory Comput. 2012, 8 (9), 3314.

Chapter 3

DESIGN AND SYNTHESIS OF HYBRID MATERIALS USING INNOVATIVE ECO-FRINEDLY METHODOLOGIES BASED ON MECHANOCHEMISTRY

3.1 Introduction

3.1.1 Green chemistry and green metrics

Green chemistry, being part of sustainable chemistry, is a research field concerning the design of chemical products and processes to reduce or eliminate the use and generation of hazardous [1-3]. The global attention garnered in the last two decades by Green Chemistry is due to its potential to innovate chemistry by facing environmental and economic issues simultaneously. It is based on twelve principles that outline the design rules for making a greener chemical, process, or product. Basically, these principles address to reduction or removal of dangerous chemicals from the synthesis to the application of chemical products. Besides concepts as hazards and chemical toxicity, Green Chemistry key points include energy consumption, waste reduction and life cycle perception [4].

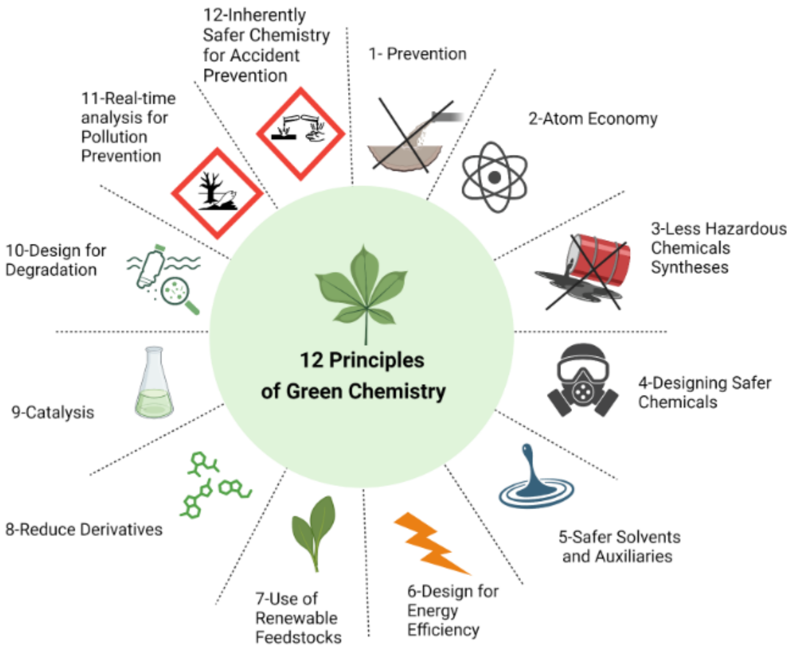

Figure 1. Twelve Principles of Green Chemistry [5].

Green chemistry metrics are measurable features that assess adherence to the principles of Green Chemistry for a chemical process, evaluating its overall efficiency, or environmental impact [6-8].

Atom economy (AE) and Environmental factor (*E*-factor) are the simplest and most popular green metrics. AE is a useful "*a priori*" indicator for quickly forecast the amount of waste generated from starting materials involved in a process. The optimal AE is 100% indicate a process where all reactants are found in the desired product. *E*-factor is the actual amount of waste produced per kg of product, including solvent losses and chemicals during reaction and work-up. Therefore, *E*-factor can be calculated once the experience has been done. Values of *E*-factor closer to 0 describe an eco-friendly process. Solvents have the ability to dissolve, suspend, separate or transport other substances. Their usage in synthesis and processes corresponds to a major part of produced waste [9].

Therefore, in a greener vision, solvents need to be reduced or eliminated during manufacturing and processing.

3.1.2 Mechanochemistry and mechanochemical methods

The rapid advances made in the field of Green Chemistry led to the development of fields of investigations, such as mechanochemistry, that is also a sustainable and enabling technology. According to IUPAC, mechanochemistry has been acknowledged as one of the top 10 technologies that could change the world [10]. Mechanochemistry enables powerful, sustainable, environmentally benign, cost-effective, and time-saving synthetic approach, objectively based on Green Chemistry and Green metrics [11]. This methodology provides chemical and physico-chemical transformations driven by mechanical forces forming through grinding and milling, often without the use of solvents. When a small quantity of solvent is necessary to enhance or control chemical reactivity, Liquid-assisted grinding (LAG) conditions are applied [12]. The empiric parameter η (μL of solvent per mg of solid reactants) characterizes LAG processes. When $\eta=0$ reaction occurs in neat grinding. For $0< \eta< 1$ LAG conditions are ensured. Values of η up to 6, the reaction is considered slurry, while if $\eta> 6$ the reaction is considered in solution [13].

The operating devices to conduct mechanochemical process consist of ball-mills (for batch processes), such as vibrating, planetary, and extruders (for continuous flow methods) [14]. In Figure 2 a schematic representation of ball mill operation modes is represented.

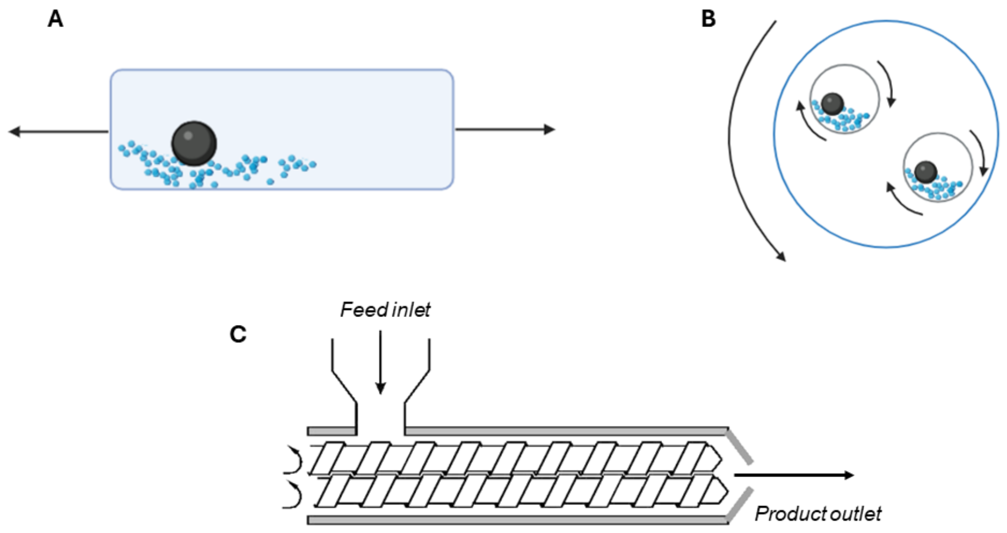

Figure 2. Schematic illustration of mode of motion of vibrating (A) and planetary (B) mill, and twin-screw extruder (C).

Vibrating ball mills are generally composed of a jar shaken at high frequency. Basically, ball milling process is based on transmission of mechanical energy to powders, contained inside, during the collisions of the balls in the jar with each other and with the jar walls. The resulting mechanical deformation gives rise to a physical and/or chemical transformation [15-19]. In a ball miller, vibration can occur vertically or horizontally.

Planetary ball mills consist of one or more jars that rotate simultaneously around their axis (in one sense) and a central axis (in the opposite sense), creating effective mixing and grinding of the reactants [20].

Twin screw extruders (TSE), widely set in industries, involve the conveyance of reactants through a barrel by the rotation of two intermeshing screws that can co- or counter rotate. The screw geometry can generate a strong forward conveying action, establishing intense shear and mixing forces [21]. However, TSE processes can not always be claimed as mechanochemical ones, if the reaction occurs in a melt phase, as often occurs for hot melt extrusion processes.

A fine tuning of several technical and process parameters must be taken into account during any mechanochemical reaction. Colacino and coworkers comprehensively summarized the most important variables to fix, including milling media (i.e. jars and balls) materials and type, size and number of milling balls, volume and filling ratio of jar, operating frequency, reaction time, temperature [22].

Revolutionizing conventional chemistry, mechanochemistry has powerful applications across multiple fields, such as preparation of active pharmaceutical ingredients (APIs) [23-31], food additives [32], protection of N-terminus [33] or C-terminus amino acid derivatives synthesis [34], transformation of porous metal-organic frameworks (MOFs) [35] and hybrid inorganic-organic materials [36].

Recently, mechanochemistry was successful exploited for the preparation of functionalized biohybrid bridged silsesquioxane nanoparticles via unconventional sol-gel process. The mechanochemical preparation of the organosilicon precursors was based on a sequential reaction pathway involving LAG and 1,1-carbonyldimidazole (CDI)-mediated one-pot/two-pot reactions conducted in planetary ball mill equipment. Successively, Si-based hybrid nanospheres with uniform size and controlled morphology were easily achieved with vibrational ball-mill-assisted mechanochemical sol-gel procedure, overcoming the limitation of conventional Stöber-base procedure in solution [37].

The design of suitable nanomaterials possessing controlled surface functionalities remains one of the major challenges in the field of material science. Technological progress pushes towards the accomplishment of increasingly sophisticated hybrid materials synthesized using advanced methodologies. Besides, developing synthetic processes that are straightforward, low-cost, time saving, high-yield, scalable, and safe is a global urgent need. Solution-based processing does not ensure that all goals are achieved. Differently, mechanochemistry moves in this direction. Solvent-free mechanochemical grafting of different inorganic and organic solid materials with various organosilicon compounds was explored.

The first approach, developed by Schüth *et al.,* involved ball milling of widely employed inorganic oxides or mesoporous structures together with organosilanes at room temperature [38].

Moreover, magnetic separable SBA-15 nanocomposites for catalysis applications were easily synthesized by Luque and his team using two-step dry milling solventless process, performed in a Retsch PM-100 planetary ball mill, using 18 stainless steel balls (ϕ 10 mm), at 350 rmp for 10 min. The ball milling protocol was applicable to a large variety of supports (*e.g.*, Al_2O_3 nanomaterials, carbon nanotubes, TiO_2 platforms) and metals (*e.g.*, Au, Ni, Mn, Co), conferring promising catalytic activities to functionalized materials [39].

3.2 Mechanochemical modification of mesoporous silica-based nanoparticles

3.2.1 Results and Discussion

The design of MSN-based nanosystems developed during the PhD course consists of a set of synthetic procedures that mostly could be considered low-impact. According to solvent-based procedures, the synthesis of starting architecture is carried out at room temperature, without catalyst agents, employing surfactant removal by water extractions with potential re-use. Mainly water or other not extremely toxic and easily recoverable solvents are used for final MSN nanocarriers. Scaling up the synthetic methodologies requires 25-fold larger reactor, working under the same operative small-scale conditions, demonstrating high reproducibility. Additionally, synthetic procedures for mesoporous silica preparation [40] and functionalization [41] based on microwave irradiation in solvent-free conditions have been explored.

When developing nanoparticles for drug delivery, the most impressive challenge that need to be addressed is their interaction with biological entities present in blood. Surface properties, such as charge density, functional group, defects, and morphology, play a key role, influencing these interactions [42]. It seems clear that nanomaterials surface property is strictly connected to hazard potential of these class of materials. Material scientists are increasingly aware of the urgent need to contribute to environmental health, ensuring safety and mitigating hazards. "*Safer-by-design*" strategy represent a possible emerging strategy for sustainable and responsible development of nanomaterials [43].

The potent scalable perspective prospective of mechanochemistry and its capability to control and assist chemical reactions for designing advanced hybrid MSN-based delivery systems were investigated during the PhD research activities at the Institute Charles Gerhardt Montpellier (ICGM) in France.

By applying mechanochemical synthetic approaches, MSU-type starting materials were opportunely and selectively functionalized on both external and internal surfaces in order to obtain suitable nanodevices potentially employed for drug delivery. Furthermore, mechanochemical methods were explored to dramatically improve the extraction of surfactant inside pores of MSNs, with highly reduced amount of solvent needed. A comparison between results under solution-based conditions and mechanochemical approach will be presented.

More efforts were made to well fit the high controlled, precise, and cleaner methodologies that mechanochemistry allow to implement, with material science approach. All the presented activities originated from a careful study of most important mechanochemical parameters as ball milling devices, milling media type, number and material of milling media, operating frequency, reaction time and temperature, followed by the optimization of the process. Experimental data details do not disclose because a patent application is going to be filed.

3.2.1.1 External functionalization of MSN-based nanomaterials with targeting molecules

The most disruption potentiality of MSNs is the selective modification of external and internal nanoparticles surfaces using one or more different functionalizing molecules. In particular, by decorating external surface of MSN-based drug delivery systems with ligands able to interact selectively with overexpressed receptors of tumor cells, specific retention and uptake of MSNs into cancer cells will be enhanced, avoiding toxic off target effects on healthy tissues. Most employed targeting ligands are small molecules [44], peptides [45], and aptamers [46]. The most widespread chemical bond used to modify MSN surface is covalent that includes chemical reactions of carbonyl reactive groups, amine reactive groups, sulfhydryl reactive groups and reaction known as click chemistry. Each of these conjugations must be stable enough under physiological conditions [47]. Importantly, targeted MSNs for drug delivery have to be engineered with a suitable targeting moiety density, in order to allow cell surface interactions, preventing any toxicity.

In an accurate process conducted during my PhD course and concerning the optimization of external modification of MSN-based nanodevices, it has been demonstrated that increasing the amount of the targeting ligand, folic acid, on the external surface of MSNs, the Folic acid-functionalized MSN nano-systems showed striking selectivity towards cancer cells, without toxicity on healthy tissues [48].

MSN-based nanomaterials were functionalized with small targeting molecules of different nature using mechanochemical methodologies. The investigations aimed to explore the possibility to optimize the traditional solvent-based process by reducing solvent usage, waste generation and time of reactions, maximizing the overall process efficacy.

In a typical solution-based procedure, MSNs were mixed with the targeting molecule (TM) in presence of an excess of an activating agent and a base. After stirring at room temperature for 40 h, TM-functionalized MSN nanoparticles were filtered, washed with organic solvents to remove unreacted reagents, and finally dried and collected as powder. The ~~extraction~~ procedure involving the ball milling technology, were carried out without solvent, using a safer and greener activating agent (Scheme 1).

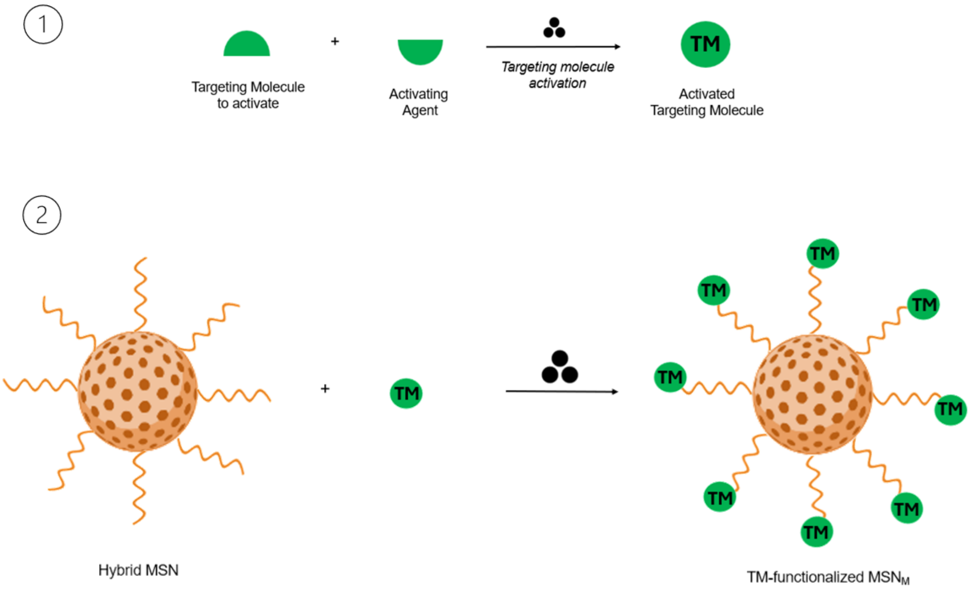

Scheme 1. Schematic representation of TM activation (1) and TM grafting of MSNs (2).

MSNs grafting by mechanochemical route made significant improvements to the process (Table 1).

Without even a drop of solvent, in reduced reaction time, and working with safer and fewer compounds, TM-functionalized MSN_M was efficiently synthesized.

Sample	Reaction Time [h]	Solvent used for synthesis [mL/g_{MSN}]	Activating Agent (AA)	mol_{AA}/mol_{FOL}
TM-MSN	40 h	5	DIC	3.5
TM-MSN_M	Shorter than in solution process	0	Safer and greener AA	Lower than in solution process

Table 1. Comparison of MSN functionalization: Mechanochemistry approach vs. solvent-based process.

The amount of TM grafted on MSN surface, was evaluated by UV-Vis absorption spectrophotometer analysis, on the basis of the standard curve using UV absorbance at 291 nm as reference (Figure 2).

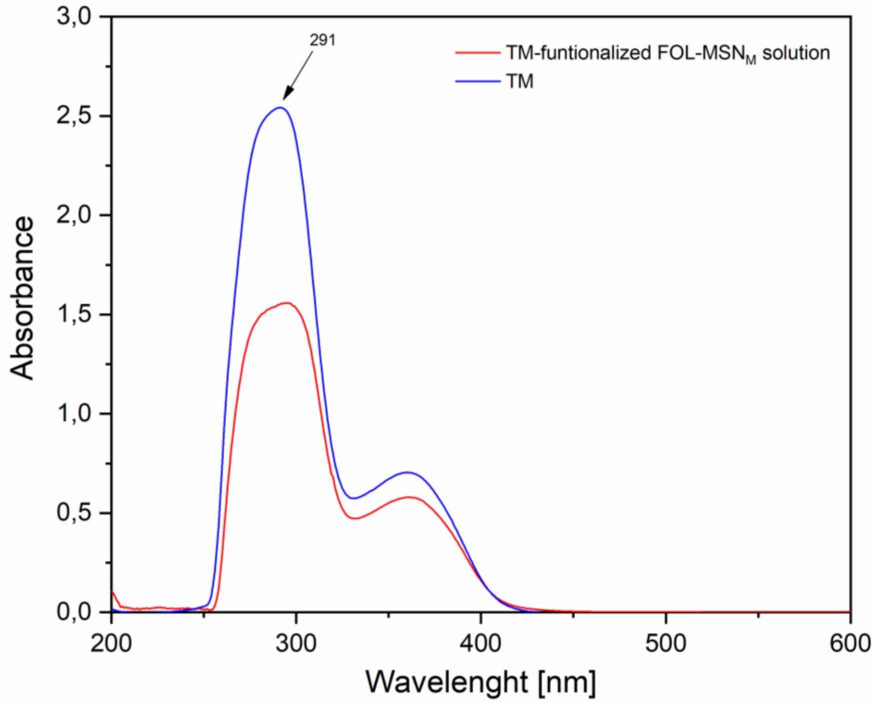

Figure 2. UV-Vis spectra of TM-functionalized MSN_M solution (red curve) and TM (75 µM, blue curve) in DMSO.

The successful of TM conjugation on MSN surface was further confirmed by UV spectra shown in Figure 3. Two absorbance peaks appeared at 283 nm and 365 nm on TG-functionalized MSN_M spectrum and belonged to TM, while its precursor MSN had no characteristic absorbance in this range.

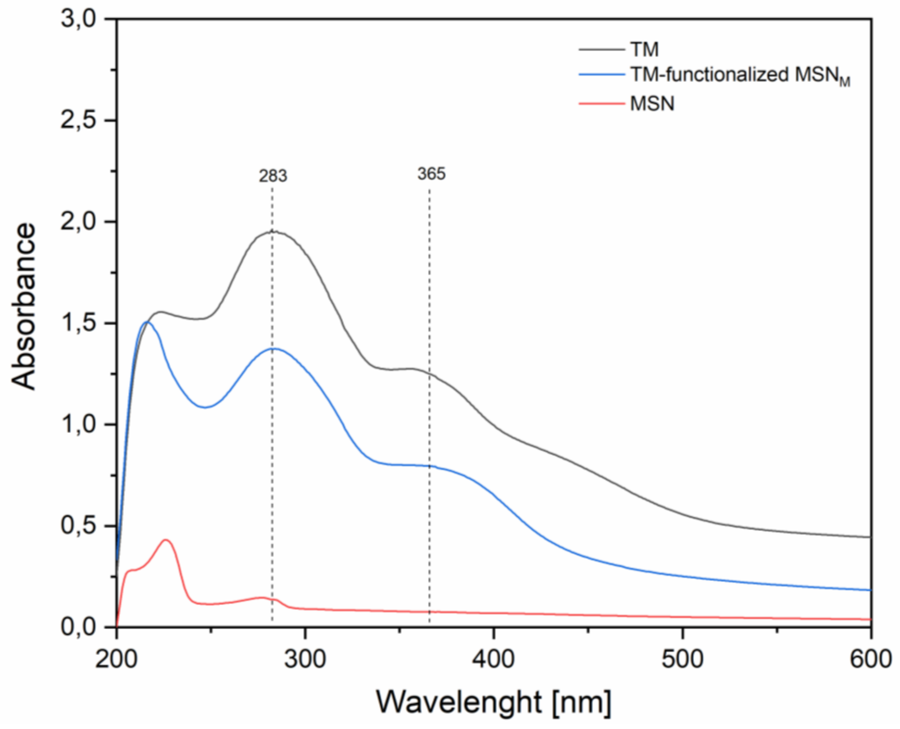

Figure 3. UV-Vis spectra of TM-functionalized MSN_M (blue curve), TM (black curve) and MSN in ethanol. Concentration of solutions: 1.25 mg/mL.

FTIR spectra were acquired to verify the accomplishment of TM grafting on nanoparticles, as illustrated in Figure 4. Peaks on TM-functionalized MSN_M spectrum (red curve), in the range 1694 cm^{-1} – 1338 cm^{-1}, not appreciable on MSN spectrum (black curve), clearly supporting the successful grafting of targeting molecule.

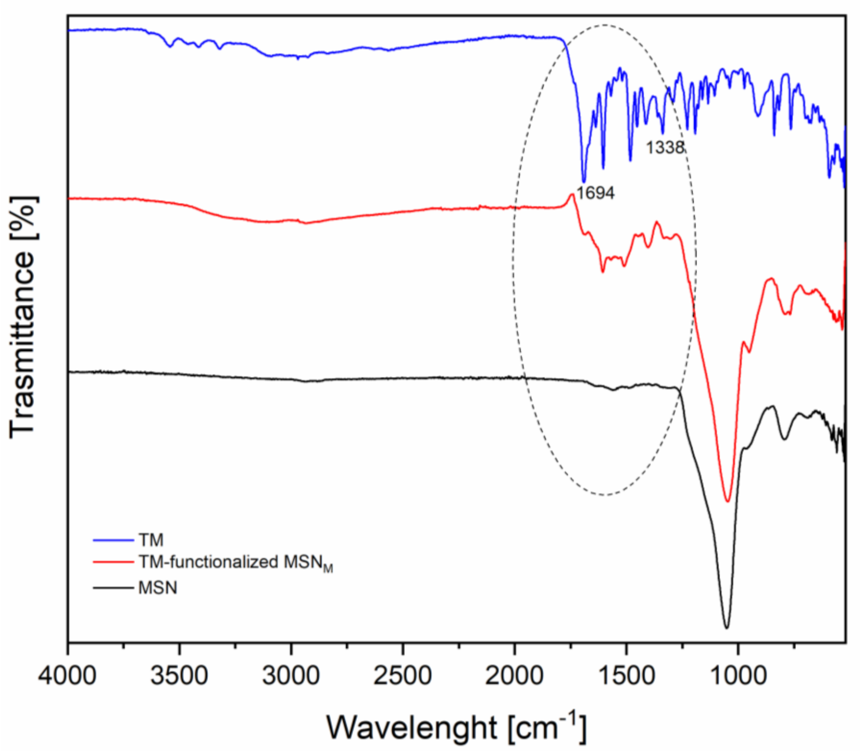

Figure 4. FTIR spectra of TM (blue), TM-functionalized MSN$_M$ (red) and MSN (black) samples.

Targeting molecule, was opportunely and efficiently grafted on external surface of MSNs. Before to start with inner functionalization of MSN walls, surfactant inside the pores of MSNs must be removed.

According to solvent-based method, surfactant was easily removed by water extraction. The number of extractions required to make a complete surfactant removal was established by monitoring, via TGA analysis, the total mass loss of little amounts of samples subjected to additional extraction steps, until a constant value was reached. The solvent protocol provided six steps of extraction (0.3 mL/mg$_{MSN}$). When mechanochemistry was applied to extraction process (Scheme 2), this condition was dramatically changed.

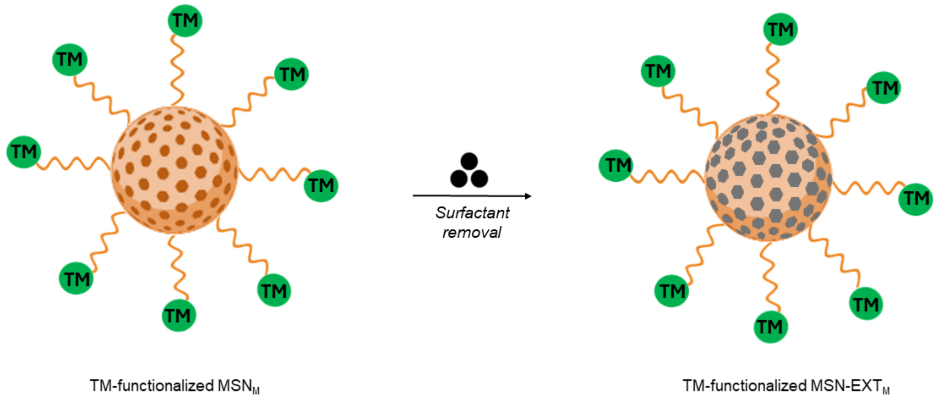

Scheme 2. Schematic representation of TM-functionalized MSN$_M$ extraction.

Water consumption for preparing extracted nanoparticles via mechanochemistry, was remarkably smaller than extraction under solvent protocol, and step extraction occurred in shorter time (Table 2).

Sample	Extraction step time [h]	mL$_{water}$/mg$_{MSN}$
TM-functionalized MSN-EXT	18	0.3
TM-functionalized MSN-EXT$_M$	Shorter than solution process	Lower than solution process

Table 2. Comparison time and water consumption.

Monitoring mass changes of samples at each extraction step via TGA measurements, TM-functionalized MSN-EXT$_M$ registered a lower organic content compared to extracted nanoparticles via solution-based methodology, TM-functionalized MSN-EXT. Interestingly, the best extraction efficiency was reached in mechanochemical conditions. In fact, the greater the template extraction removal, the less organic content, the better the efficiency of the operation. Moreover, the gap between the extraction steps when mechanochemistry was applied, was always higher than in solution procedure, denoting a greater pushing force in mechanochemical process. Potentially, a 7th extraction could be conducted, in order to empty MSN pores more.

3.2.1.2 Internal functionalization of hybrid MSN-based nanoparticles

Internal functionalization of MSN-based drug delivery systems is accomplished for controlling drug loading and release kinetics. For this purpose, MSNs can be modified introducing responsive molecules able to achieve zero premature drug leakage during blood circulation and trigger the cargo release under specific stimuli. A large variety of compounds sensitive to physical [49, 50], chemical [51, 52], and biological [53, 54] stimuli were explored.

Generally, the first step of modification is the functionalization with an organosilane, in order to introduce functional groups on the MSN surface, useful for construction of stimuli responsive linker.

Mechanochemical internal grafting of extracted MSNs with organosilane (OC) was studied and compared to solution-based approach.

According to solution conditions, extracted MSNs were mixed with an appropriate organosilicon compound (OC), bearing the desired functional groups to conjugate on MSN pores wall. In a suspension of MSNs was added a solution containing the organosilane. The mixture was stirred at room temperature for 18 h. Successively, the reaction mixture was filtered, washed, and dried, in order to afford MSN-OC nanoparticles. When mechanochemistry was applied, the milling medium equipped with a define number of balls was filled with MSNs and the organosilane (Scheme 3). A small (catalytic) amount of water was added to the jar, as a way to accelerate OC grafting onto

MSN inner pores. LAG condition was established with η value below 1. The amount of grafted OC was estimated through TGA measurement.

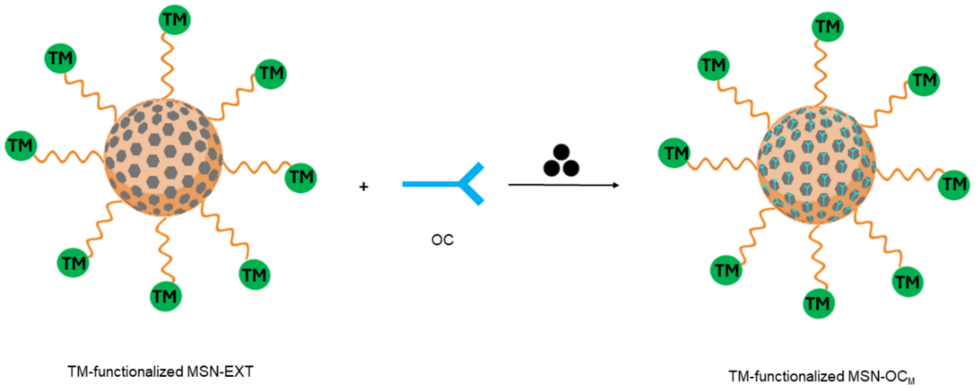

Scheme 3. Schematic representation of internal surface MSN functionalization with OC.

FT-IR investigation was conducted to support the mechanochemical grafting of OC. The spectra comparison of extracted precursor, TM-functionalized MSN-EXT, OC and TM-functionalized MSN-OC$_M$ were showed in Figure 5. The broad band detected on functionalized MSN-OC spectrum (red curve) in the range 2970 - 2870 cm^{-1} belonged to OC molecule and appeared after functionalization. No similar bands were observed on TM-functionalized MSN-EXT spectrum (black curve).

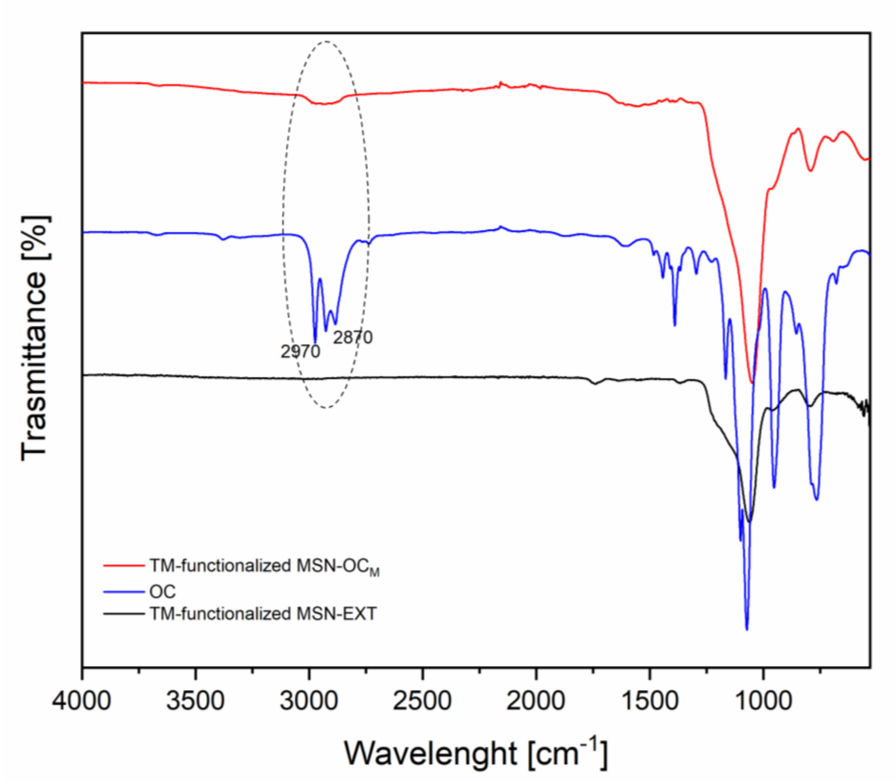

Figure 5. FT-IR spectra of TM-functionalized MSN-OC$_M$ (red curve), OC (blue curve) and TM-functionalized MSN-EXT (black curve).

3.2.1.3 pH-responsive hydrazone bond formation

Due to its faster hydrolytic rate at acidic pH and high stability in neutral physiological pH, hydrazone bond is one of the most employed pH-responsive linkages for drug delivery. Conjugation of the drug via pH-sensitive hydrazone linkage allows the selective release of therapeutic agent at the target cancer site, without affecting healthy tissues.

Hydrazones are formed by a condensation reaction between hydrazine or hydrazide with aldehydes or ketones. Generally, in solution, hydrazones are obtained in the presence of an acid catalyst. A pH value of about 4.5 is typically advantageous for hydrazone formation [55]. Higher or lower pH leads to lower yield and slower kinetics [56]. Solvent-free methodologies and mechanochemical synthesis of hydrazones are recently developed

[57-59, 28]. Reaction kinetics for hydrazone formation is better with aldehydes than ketones, making the employing of aldehydes well-wide.

As described, the pH-sensitive hydrazone bond in MSN-based nanodevices developed during PhD activities, was formed with the hydroxymethyl ketone presents on the drug molecule.

Taking into account the implication of cytotoxic substances, such as the manipulation of antineoplastic drug, and their high value in term of costs, appropriate model molecules were employed for the exploitation of mechanochemistry in hydrazone bond formation. Remarkably, ketone model molecules were used during mechanochemistry hydrazone bond formation.

A careful investigation of the of all mechanochemical conditions and parameters allowed to achieve the best result. ^{1}H NMR spectrum of the final product in Figure 7 agreed with that reported in literature, Singlet at δ =10.52 was accounted for hydrazone NH proton resonance, confirming the formation of desired hydrazone bond.

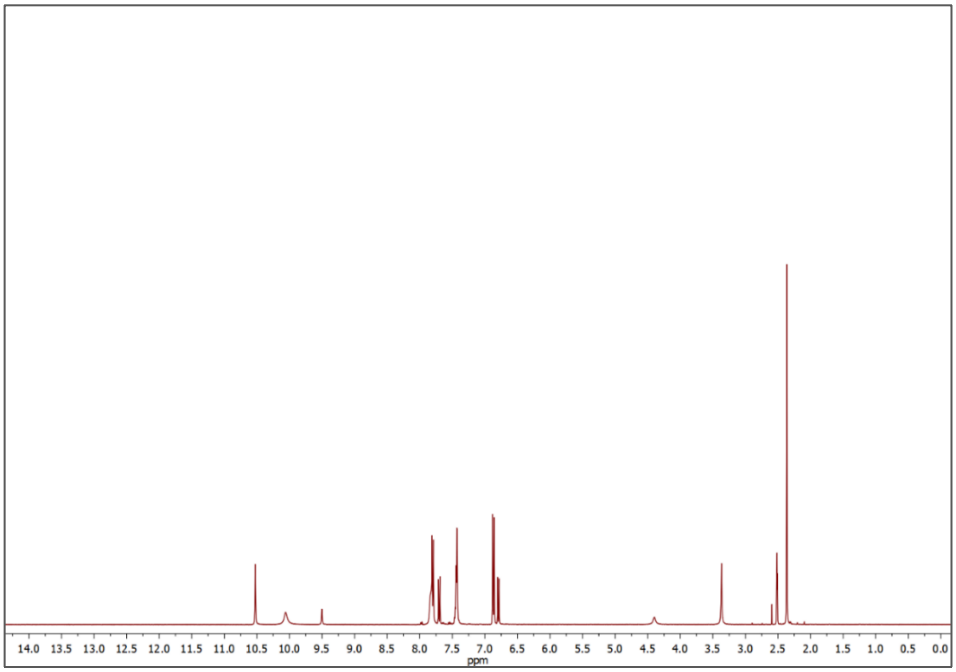

Figure 7. ^{1}H NMR spectrum of the final hydrazone-bearing product.

Mechanochemical research related to the preparation of hybrid MSN-based drug delivery systems stopped here because of 6 months duration of PhD period abroad. More investigations must be accomplished. However, it was clearly demonstrated the powerful advantages of mechanochemistry in the development of hybrid of MSN-based nanodevices. The overall process exhibited high efficiency and selectivity, simple routes of operations, drastic economy in energy, time, solvent, and waste. Definitively, the high-energy ball milling approach demonstrated to offer new synthetic opportunities in the development of hybrid nanomaterials.

3.2.1.4 Surfactant extraction from pores of MSNs

A crucial step in mesoporous silica materials is the removal of organic templates occluding the pores. This operation makes pores accessible to further modification, such as organosilane functionalization and drug encapsulation, affecting final properties of final desired materials.

The surfactant can be non-ionic, cationic, anionic, and even ionic liquid. Several removal methods are reported in literature, divided into physical, such as calcination [60], and chemical methods, such as solvent extraction [61, 62].

In an exhaustive study, Zhao and Ghaedi reviewed the recent development methodologies for surfactant removal from different families of mesoporous silica materials, discriminating advantages and drawbacks [63]. Most important details are briefly discussed above. Calcination is commonly conducted under air atmosphere at about 500 °C for more than 5 h. This methodology leads to significant structural shrinkage, reduction in silanol concentration, resulting in mesoporosity destruction [64]. Therefore, during calcination toxic gases are generated, with no possibility to recover and reuse templates.

Solvent extraction is the most common methodology for template removal. Water, methanol, ethanol dichloromethane are generally used, each of them with a proper efficiency. More silanol groups are preserved and mesoporous structure are conserved, indicating that solvent extraction method is more advantageous than the calcination. However, this method is not environmentally and economically beneficial due to a large consumption of organic solvent and the required high energy for solvent recovery. Furthermore, the template may not be completely removed.

It seems clear that the most recommended technique to prepare MSN-based materials for drug delivery is solvent extraction.

Conditions for surfactant removal of MSN materials developed during the PhD activities were described above. Briefly, in a typical solution-based procedure, six extraction steps lasting 18 h were performed using water (0.3 ml/mg_{MSN}) as solvent. The template to remove from mesopores was Triton X-100, a neutral, low-cost, non-toxic, and biodegradable surfactant.

Encouraging by enthusiastic results achieved with mechanochemical-based extractions of TM-functionalized MSN nanoparticles, surfactant removal from starting MSN materials was investigated via mechanochemistry approach.

Firstly, the mechanochemical parameters, such as milling media, balls, Hz, were kept the same as TM-functionalized MSN-EXT_M (black icon, Table 6, and Table 7). Successively, new conditions were tested. Mechanochemical-based extractions confirmed the most efficient results. More performing results were achieved when applying new extraction condition (green icon, Table 6, and Table 7), reaching the lowest organic residue content.

Potentiality of mechanochemistry in reduction of reaction time, solvent usage and waste production was once again provided, leading to the development of the desired product. Interestingly, a 7th extraction conducted in mechanochemistry, was able to reduce template content in mesopores, while no significant organic changes were registered with solution extraction method.

Sample	**Extraction step time [h]**	**mL_{water}/mg_{MSN}**
Solution	18	0.3
●●●	Shorter than in solution	Lower than in solution
🟢🟢🟢	Shorter than in solution	Lower than in solution

Table 6. Comparison time and water consumption.

	Solution	●●●	🟢🟢🟢
Step	**Organic ratio R.O. [%]**	**Organic ratio R.O. [%]**	**Organic ratio R.O. [%]**
Starting MSN	51.32		
EXTRACTION 1	48.31	Lower than in solution	Lower than in solution
EXTRACTION 2	46.65	Lower than in solution	Lower than in solution
EXTRACTION 3	44.31	Lower than in solution	Lower than in solution
EXTRACTION 4	42.21	Lower than in solution	Lower than in solution
EXTRACTION 5	40.12	Lower than in solution	Lower than in solution
EXTRACTION 6	38.89	Lower than in solution	Lower than in solution
EXTRACTION 7	38.12	Lower than in solution	Lower than in solution

Table 7. Comparison efficacy extraction under solution-based conditions and mechanochemical approaches (black and green icons).

3.2.2 Experimental

For confidentiality reasons related to patent filing it is not possible to indicate any experimental conditions or the structures of the systems involved.

3.3 Conclusion and possible future prospects

Here, it was partially presented a possible mechanochemistry revolution related to hybrid MSN-based preparation. During the doctoral experimental activity, mechanochemistry emerged as highly promising and simple approach able to compete with conventional solvent-based procedures in the design of MSN-based materials with more sustainable advanced functionalities. Attention on solvent usage, waste generation, and time consuming, was always kept high. Mechanochemical contribution in MSN synthesis goes beyond greener advantages, making the process safer and more efficient.

Further challenges and investigations are required to better understanding the possible scalability and reproducibility of the mechanochemical practise on material science.

References

1. Anastas, P. T., Warner, J. C. Green Chemistry: Theory and Practice. Oxford England: Oxford University Press, 1998.
2. Horváth, I. T., & Anastas, P. T. Introduction: green chemistry. Chemical Reviews, 2007, 107(6), 2167-2168.
3. Anastas. P. T., Williamson, T. C., in Green Chemistry: Designing Chemistry for the Environment, American Chemical Series Books, Washington, DC, 1996, pp. 1–20.
4. Anastas, P. T., Eghbali, N. Green chemisztry: principles and practice. Chemical Society Reviews, 2010, 39(1), 301-312.
5. Anastas, P. T., Warner, J. C. Principles of green chemistry. Green chemistry: Theory and practice, 1998, 29, 14821-14842.
6. Anastas P.T. Heine LG, Williamson TV, Green Chemical Synthesis and Processes. American Chemical Society, Washington DC, 2000.
7. Sheldon, R. A. Metrics of green chemistry and sustainability: past, present, and future. ACS Sustainable Chemistry & Engineering, 2018, 6(1), 32-48.
8. Erythropel, H. C., Zimmerman, J. B., de Winter, T. M., Petitjean, L., Melnikov, F., Lam, C. H., Lounsbury, A.W., Mellor, K.E., Jankovic, N.Z., Tu, Q., Pincus, L.N., Falinski, M.M., Shi, W., Coich, P., Plata, D.L., Anastas, P. T. The Green ChemisTREE: 20 years after taking root with the 12 principles. Green chemistry, 2018, 20(9), 1929-1961.
9. Lavilla, I., Romero, V., Costas, I., Bendicho, C. Greener derivatization in analytical chemistry. TrAC Trends in Analytical Chemistry, 2014, 61, 1-10.
10. Gomollón-Bel, F. IUPAC Top Ten Emerging Technologies in Chemistry 2021: Breakthroughs for a circular, climate-neutral future. Chemistry International, 2021, 43(4), 13-20.
11. Fantozzi, N., Volle, J. N., Porcheddu, A., Virieux, D., García, F., Colacino, E. Green metrics in mechanochemistry. Chemical Society Reviews, 2023.
12. Bowmaker, G. A. Solvent-assisted mechanochemistry. Chemical Communications, 2013, 49(4), 334-348.
13. Hasa, D., Jones, W. Screening for new pharmaceutical solid forms using mechanochemistry: A practical guide. Advanced drug delivery reviews, 2017, 117, 147-161.
14. Cuccu, F., De Luca, L., Delogu, F., Colacino, E., Solin, N., Mocci, R., Porcheddu, A. Mechanochemistry: new tools to navigate the uncharted territory of "impossible" reactions. Chem. Sus. Chem., 2022, 15(17), e202200362.
15. Sopicka-Lizer, M. (Ed.). High-energy ball milling: mechanochemical processing of nanopowders. Elsevier, 2010.
16. Delogu, F., Mulas, G. Experimental and Theoretical Studies in Modern Mechanochemistry, Transworld Research Network, Kerala, India, 2010.
17. Ali El-Remaily, M.A.E.A.A., Soliman, A. M. M., Elhady, O.M. Green Method for the Synthetic Ugi Reaction by Twin Screw Extrusion without a Solvent and Catalyst. ACS Omega, 2020, 5(11), 6194-6198.
18. Suryanarayana, C. Mechanical alloying and milling. Progress in materials science, 2001, 46(1-2), 1-184.
19. Baláž, P. Applied Mechanochemistry. Mechanochemistry in Nanoscience and Minerals Engineering; Springer: Berlin/Heidelberg, 2008, 297– 405.
20. Colacino, E., Carta, M., Pia, G., Porcheddu, A., Ricci, P. C., Delogu, F. Processing and investigation methods in mechanochemical kinetics. ACS Omega, 2018, 3(8), 9196-9209.

21. Giles, H. F., Wagner, J. R., Mount, E. M. Extrusion: The definitive processing guide and handbook, William Andrew, Elsevier, Amsterdam, 2014.
22. Tan, D., García, F. Main group mechanochemistry: from curiosity to established protocols. Chemical Society Reviews, 2019, 48(8), 2274-2292.
23. Colacino, E., Porcheddu, A., Charnay, C., & Delogu, F. From enabling technologies to medicinal mechanochemistry: an eco-friendly access to hydantoin-based active pharmaceutical ingredients. Reaction Chemistry & Engineering, 2019, 4(7), 1179-1188.
24. Geib, R., Colacino, E., Gremaud, L. Sustainable Beckmann Rearrangement using Bead-Milling Technology: The Route to Paracetamol. Chem. Sus. Chem., 2024, e202301921.
25. Mocci, R., Colacino, E., Luca, L. D., Fattuoni, C., Porcheddu, A., Delogu, F. The mechanochemical Beckmann rearrangement: An eco-efficient "cut-and-paste" strategy to design the "good old amide bond". ACS Sustainable Chemistry & Engineering, 2021, 9(5), 2100-2114.
26. Crawford, D. E., Porcheddu, A., McCalmont, A. S., Delogu, F., James, S. L., Colacino, E. Solvent-free, continuous synthesis of hydrazone-based active pharmaceutical ingredients by twin-screw extrusion. ACS Sustainable Chemistry & Engineering, 2020, 8(32), 12230-12238.
27. Porcheddu, A., Delogu, F., De Luca, L., Colacino, E. From lossen transposition to solventless "Medicinal Mechanochemistry". ACS sustainable chemistry & engineering, 2019, 7(14), 12044-12051.
28. Colacino, E., Porcheddu, A., Halasz, I., Charnay, C., Delogu, F., Guerra, R., Fullenwarth, J. Mechanochemistry for "no solvent, no base" preparation of hydantoin-based active pharmaceutical ingredients: nitrofurantoin and dantrolene. Green chemistry, 2018, 20(13), 2973-2977.
29. Konnert, L., Dimassi, M., Gonnet, L., Lamaty, F., Martinez, J., & Colacino, E. Poly (ethylene) glycols and mechanochemistry for the preparation of bioactive 3, 5-disubstituted hydantoins. RSC Advances, 2016, 6(43), 36978-36986.
30. Bonnamour, J., Métro, T. X., Martinez, J., Lamaty, F. Environmentally benign peptide synthesis using liquid-assisted ball-milling: application to the synthesis of Leu-enkephalin. Green chemistry, 2013, 15(5), 1116-1120.
31. Konnert, L., Reneaud, B., de Figueiredo, R. M., Campagne, J. M., Lamaty, F., Martinez, J., Colacino, E. Mechanochemical preparation of hydantoins from amino esters: application to the synthesis of the antiepileptic drug phenytoin. The Journal of Organic Chemistry, 2014, 79(21), 10132-10142.
32. Declerck, V., Nun, P., Martinez, J., Lamaty, F. Solvent-free synthesis of peptides. Angewandte Chemie International Edition, 2009, 48, 9318-9321.
33. Staab, v. H. A. Reaktionsfähige und N-carbonsäureamides des imidazols und triazols. Liebigs Ann. Chem. 1957, 609, 83−88.
34. Konnert, L., Lamaty, F., Martinez, J., Colacino, E. Solventless mechanosynthesis of N-protected amino esters. The Journal of Organic Chemistry, 2014, 79(9), 4008-4017.
35. Konnert, L., Lamaty, F., Martinez, J., Colacino, E. Solventless mechanosynthesis of N-protected amino esters. The Journal of Organic Chemistry, 2014, 79(9), 4008-4017.
36. Amrute, A. P., Zibrowius, B., Schüth, F. Mechanochemical Grafting: A Solvent-less Highly Efficient Method for the Synthesis of Hybrid Inorganic–Organic Materials. Chemistry of Materials, 2020, 32(11), 4699-4706.
37. Lupacchini, M., Mascitti, A., Tonucci, L., d'Alessandro, N., Colacino, E., Charnay. From molecules to silicon-based biohybrid materials by ball milling. ACS sustainable chemistry & engineering, 2018, 6(1), 511-518.

38. Amrute, A. P., Zibrowius, B., Schüth, F. Mechanochemical Grafting: A Solvent-less Highly Efficient Method for the Synthesis of Hybrid Inorganic–Organic Materials. Chemistry of Materials, 2020, 32(11), 4699-4706.
39. Ojeda, M., Balu, A. M., Barrón, V., Pineda, A., Coleto, Á. G., Romero, A. Á., & Luque, R. Solventless mechanochemical synthesis of magnetic functionalized catalytically active mesoporous SBA-15 nanocomposites. Journal of Materials Chemistry A, 2014, 2(2), 387-393.
40. Procopio, A., Das, G., Nardi, M., Oliverio, M., Pasqua, L. A Mesoporous ErIII-MCM-41 Catalyst for the Cyanosilylation of Aldehydes and Ketones under Solvent-free Conditions. Chem. Sus. Chem.: Chemistry & Sustainability Energy & Materials, 2008, 1(11), 916-919.
41. Pasqua, L., Procopio, A., Oliverio, M., Paonessa, R., Prete, R., Nardi, M., Casula, M. F., Testa, F., Nagy, J. B. Hybrid MCM-41 grafted by a general microwave-assisted procedure: A characterization study. Journal of Porous Materials, 2013, 20, 865-873.
42. Hu, B., Liu, R., Liu, Q., Shi, Y., Li, J., Wang, L., Li, L., Xiao, X., Wu, Y. Engineering surface patterns on nanoparticles: new insights into nano-bio interactions. Journal of Materials Chemistry B, 2022, 10(14), 2357-2383.
43. Lin, S., Yu, T., Yu, Z., Hu, X., & Yin, D. Nanomaterials safer-by-design: an environmental safety perspective. Advanced Materials, 32018, 0(17), 1705691.
44. Zong, M., Cheng, Y., Ye, B., Chen, S., Yu, S., Ding, M., Lu, L., Fan, L. Preparation of mesoporous silica nanocarriers targeting glucose-6-phosphate isomerase inhibition and application in the treatment of rheumatoid arthritis. Clinical and Experimental Immunology,2023, 211(1), 46-56.
45. Shadmani, N., Makvandi, P., Parsa, M., Azadi, A., Nedaei, K., Mozafari, N., Poursina, N., Mattoli, V., Tay, F. R., Maleki, A. Hamidi, M. Enhancing methotrexate delivery in the brain by mesoporous silica nanoparticles functionalized with cell-penetrating peptide using in vivo and ex vivo monitoring. Molecular Pharmaceutics, 2023, 20(3), 1531-1548.
46. Zhang, J., Shang, J., Tang, X., & Xu, X. TfR Aptamer-Functionalized MSNs for Enhancing Targeted Cellular Uptake and Therapy of Cancer Cells. ACS omega, 2023, 8(51), 48975-48983.
47. Hermanson, G. T. Bioconjugate techniques. Academic press, 2013.
48. De Santo, M., Giovinazzo, A., Fava, M., Mazzotta, E., De Napoli, I. E., Greco, M., Comandé, A., Argurio, Perrotta, I., P., Davoli, M., Tagarelli, A., Elliani, R., Granato, T., Nicolini, G., Semperboni, S., Ballarini, E., Crocamo, C., Cavaletti, G., Lombardo, D., Sisci, D., Morelli, C., Leggio, A., Pasqua, L. Engineered mesoporous silica-based nanoparticles as smart chemotherapy nanodevice for bortezomib administration. Materials Chemistry Frontiers, 2023, 7(2), 216-229.
49. Asghar, K., Qasim, M., Dharmapuri, G., Das, D. Thermoresponsive polymer gated and superparamagnetic nanoparticle embedded hollow mesoporous silica nanoparticles as smart multifunctional nanocarrier for targeted and controlled delivery of doxorubicin. Nanotechnology, 2020, 31(45), 455604.
50. Tian, Z., Yu, X., Ruan, Z., Zhu, M., Zhu, Y., & Hanagata, N. Magnetic mesoporous silica nanoparticles coated with thermo-responsive copolymer for potential chemo-and magnetic hyperthermia therapy. Microporous and Mesoporous Materials, 2018, 256, 1-9.
51. Zhang, B. B., Chen, X. J., Fan, X. D., Zhu, J. J., Wei, Y. H., Zheng, H. S., Wang, B. Y., Piao, J. G., Li, F. Z. Lipid/PAA-coated mesoporous silica nanoparticles for dual-pH-responsive codelivery of arsenic trioxide/paclitaxel against breast cancer cells. Acta Pharmacologica Sinica, 2021. 42(5), 832-842.

52. Sarkar, S., Osman, N., Thrimawithana, T., Wann, S. B., Kalita, J., & Manna, P. Alleviation of Diabetic Retinopathy by Glucose-Triggered Delivery of Vitamin D via Dextran-Gated Functionalized Mesoporous Silica Nanoparticles. ACS Applied Bio Materials, 2024.
53. Naz, S., Wang, M., Han, Y., Hu, B., Teng, L., Zhou, J., Zhang, H., Chen, J. Enzyme-responsive mesoporous silica nanoparticles for tumor cells and mitochondria multistage-targeted drug delivery. International journal of nanomedicine, 2019, 2533-2542.
54. Bagheri, E., Alibolandi, M., Abnous, K., Taghdisi, S. M., & Ramezani, M. Targeted delivery and controlled release of doxorubicin to cancer cells by smart ATP-responsive Y-shaped DNA structure-capped mesoporous silica nanoparticles. Journal of materials chemistry B, 2021, 9(5), 1351-1363.
55. King, T. P., Zhao, S. W., Lam, T. Preparation of protein conjugates via intermolecular hydrazone linkage. Biochemistry, 1986, 25(19), 5774-5779.
56. Gutte, B. Peptide: Synthesis, Structure, and Applications. Chapter 12: Synthesis and Applications of Branched Peptides, James P. Tam, 1995, 455-500.
57. Hajipour, A. A convenient and mild procedure for the synthesis of hydrazones and semicarbazones from aldehydes or ketones under solvent-free conditions. Journal of Chemical Research, Synopses, 1999, (9), 570-571.
58. Kaupp, G., Schmeyers, J., Boy, J. Iminium salts in solid-state syntheses giving 100% yield. Journal für praktische Chemie, 2000, 342(3), 269-280.
59. Nun, P., Martin, C., Martinez, J., Lamaty, F. Solvent-free synthesis of hydrazones and their subsequent N-alkylation in a Ball-mill. Tetrahedron, 2011, 67(42), 8187-8194.
60. Hung, C., Bai, H., Karthik, M. Ordered mesoporous silica particles and Si-MCM-41 for the adsorption of acetone: A comparative study. Separation and Purification Technology, 2009, 64(3), 265-272.
61. de Avila, S. G., Silva, L. C. C., Matos, J. R. Optimisation of SBA-15 properties using Soxhlet solvent extraction for template removal. Microporous and Mesoporous Materials, 2016, 234, 277-286.
62. Ji, H., Fan, Y., Jin, W., Chen, C., Xu, N. Synthesis of Si-MCM-48 membrane by solvent extraction of the surfactant template. Journal of non-crystalline solids, 2008, 354(18), 2010-2016.
63. Ghaedi, H., Zhao, M. Review on template removal techniques for synthesis of mesoporous silica materials. Energy & Fuels, 2022, 36(5), 2424-2446.
64. Huang, Z., Huang, L., Shen, S. C., Poh, C. C., Hidajat, K., Kawi, S., Ng, S. C. High quality mesoporous materials prepared by supercritical fluid extraction: effect of curing treatment on their structural stability. Microporous and Mesoporous Materials, 2005, 80(1-3), 157-163.

Chapter 4

THE ADVENT OF MOLECULAR TARGETED THERAPIES AGAINST CANCER: TOWARDS MULTI-TARGETING DRUGS THROUGH MATERILAS ENGINEERING: A POSSIBLE FUTURE

Marianna Puzzo, Marzia De Santo, Catia Morelli, Antonella Leggio, and Luigi Pasqua

Perspective article

Published on: *Small Science*, **2024**, 2400113.

DOI: 10.1002/smsc.202400113.

Nanotechnology and nanomedicine have revolutionized the detection and treatment of challenging diseases like cancer. Compared to conventional methods, nano-based targeted therapies have shown superior effectiveness in managing the complex nature of cancer, addressing previously unmet medical needs. The engineering of nanomaterials has enabled the development of sophisticated nanodevices that can be administered as pharmaceutical formulations. These nanodevices are designed to achieve controlled drug release in specific, therapeutically relevant areas of the body.

Since the approval of the first FDA-approved nanodrug, Doxil®, in 1995 [1], the market has seen the introduction of 100 nanomedicines, with an additional 563 currently undergoing clinical trials or at various stages of development, totaling 663 [2].

Despite the widespread effectiveness demonstrated by nanomedicine applications, clinical translation is challenged by the lack of specific protocols for physicochemical, stability, quality, and safety checks, which are essential for the transition from research to clinical use [3].

The current lack of a clear and definite understanding of the *in vivo* biological effects of nanosystems is a major barrier to transitioning from laboratory research to clinical application. Addressing these challenges requires a thorough investigation of the chemistry and manufacturing processes, safety considerations, and regulatory compliance.

Drawing from our research in developing mesoporous silica-based solutions for controlled drug release and targeted delivery of conventional chemotherapeutic drugs, this perspective study presents our viewpoint on the evolution over time of the needs and technical requirements for achieving optimal outcomes, both in terms of efficacy and the reduction of toxicity, when administering anticancer drugs to patients.

The evolution of these needs aligns with the progression of cancer-targeted therapy. Beginning with methotrexate and 5-fluorouracil and advancing through tyrosine kinase inhibitors (TKIs) and hormone therapy, modern targeted therapy is oriented toward the use of multi-targeting drugs.

In general terms, oncologic therapy is deemed targeted when a drug interferes with tumor-specific metabolic pathways. This definition includes diverse mechanisms of action, such as inhibiting specific enzymes or proteins vital for cancer cell growth and boosting the immune system's ability to eradicate cancer cells. Additionally, the prospect of selectively targeting cancer cells through alternative methods, like employing small-molecule drugs or monoclonal antibodies, is also recognized.

Each type of cancer is characterized by a unique set of somatic alterations that drive its pathogenesis. Understanding these changes is crucial for determining the appropriate therapeutic treatments. Consequently, the application of precision medicine represents a personalized medicine strategy, tailoring treatments based on specific somatic mutations that significantly influence prognosis. Significant advancements, on the other side, will concern the therapeutic solutions characterized by molecular targeted therapies (MTT), both broadly and in perspective. Emerging solutions, including nanostructured skeleton-based multivalent therapies, hold promise for improving prognosis and addressing challenges related to persistent drug resistance.

With the increasing understanding of the pathways and multistep genetic alterations involved in tumor growth and progression, Molecular Targeted Therapy (MTT) has gained significant attention. MTT offers a novel, highly specific, and accurate approach to cancer treatment. These therapies exert their anticancer effects through various mechanisms, including the inhibition of cell proliferation, metastasis, and angiogenesis. Additionally, MTT can induce apoptosis and overcome multidrug resistance. MTT allows for a deeper approach to cancer treatment by targeting the biochemical mechanisms driving cancer proliferation. Recent advancements in molecular profiling of cancer have led to the approval of increasingly safe and effective targeted therapeutic agents, providing novel treatment opportunities [4].

Drug discovery strategies have shifted their focus towards identifying tumor-specific druggable mutations and developing corresponding targeted agents.

Thus, the creation of multi-targeted drugs signifies a promising strategy, paving the way for the emergence of multi-target therapeutics currently in development. These therapeutic agents incorporate multiple substances and pharmacophores designed to interact with several targets simultaneously [5].

While molecular recognition and pH responsivity remain viable approaches, the strategic shift is toward molecular multi-targeted therapy, with nanotechnology playing a pivotal role in drug design.

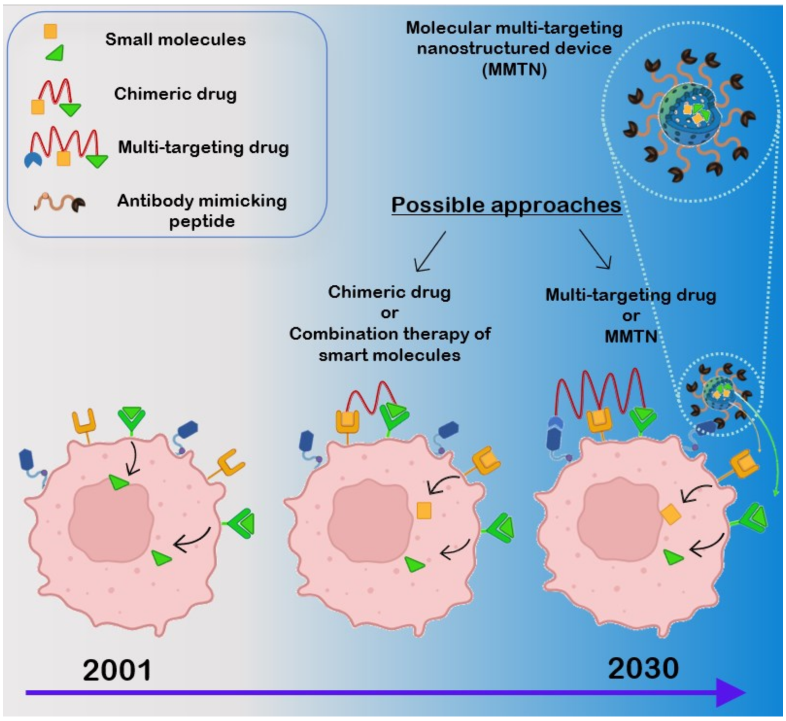

Figure 1. Schematic, non-exhaustive representation of some possible approaches in molecular targeted cancer therapies, among them, single-dual-, and multi-targeting drugs.

In Figure 1, we delineate real and perspectively imagined MMTN cancer therapeutics. Simultaneous targeting of multiple pathways enhances synergistic effects against cancer progression. Materials engineering allows the development of nanostructured devices to deliver drugs simultaneously to multiple targets, enabling precise and efficient therapeutic interventions.

In this perspective study we propose a polypharmacology approach to develop a purely molecular multi-targeting therapy. This innovative multi-targeting drug is created using a nanotechnology-based methodology, resulting in a molecular multi-targeting nanodevice. In the foreseeable future, the application of nanotechnology-based methodologies in multi-targeted drug design could become a highly effective option for cancer treatment. This advancement may lead to the development of a Molecular Multi-Targeting

Nanostructured Device (MMTN), representing a significant breakthrough in oncology therapeutics (Figure 2) [6].

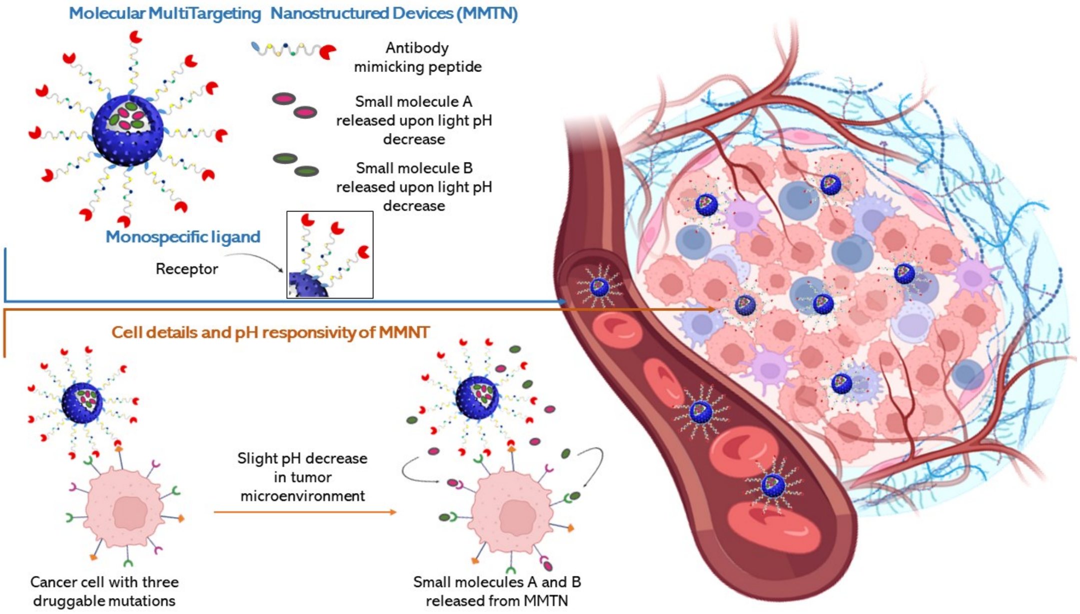

Figure 2. Graphical representation of the imaginary molecular multi-targeting nanodevice (MMTN) as a possible future scenario in the field of molecular targeted therapy (MTT).

A mesoporous silica-based nanodevice is hypothesized (Figure 2), characterized by an antibody-mimicking peptide conjugated on the external surface via an uncleavable bond, and two distinct small molecules attached inside the silica pores with a pH-sensitive bond that hydrolyses in the mildly acidic tumor microenvironment. The antibody-mimicking peptide would block extracellular target proteins, while the small molecules would penetrate the cell to inhibit intracellular target proteins.

This potential molecular multi-targeting nanodevice (MMTN) can be developed using established nanotechnological methods, representing a promising advancement in the field of molecular targeted therapy (MTT). Additionally, this approach encourages collaboration among experts from various disciplines, fostering the development of multidisciplinary solutions that leverage diverse expertise.

In my view, the future of Molecular Targeted Therapy (MTT) holds great promise, contingent upon a comprehensive understanding of nanostructure synthesis and tumor physiology.

References

1. Barenholz, Y. C. Doxil®—The first FDA-approved nano-drug: Lessons learned. Journal of controlled release, 2012, 160(2), 117-134.
2. Shan, X., Gong, X., Li, J., Wen, J., Li, Y., & Zhang, Z. Current approaches of nanomedicines in the market and various stage of clinical translation. Acta Pharmaceutica Sinica B, 2022, 12(7), 3028-3048.
3. U.S. Department of Health and Human Services Food and Drug Administration, Guidance for Industry on Drug Products, Including Biological Products, that Contain Nanomaterials, https://www.fda. gov/files/drugs/published/Drug-Products--Including-Biological-Products--that-Contain Nanomaterials---Guidance-for-Industry.pdf; V. Stone, H. Johnston, R. P. Schins, Crit. Rev. Toxicol. 2009, 39, 613
4. Min, H. Y., & Lee, H. Y. Molecular targeted therapy for anticancer treatment. Experimental & Molecular Medicine, 2022, 54(10), 1670-1694.
5. Fu, R. G., Sun, Y., Sheng, W. B., Liao, D. F. Designing multi-targeted agents: An emerging anticancer drug discovery paradigm. European journal of medicinal chemistry, 2017, 136, 195-211.
6. Puzzo, M., De Santo, M., Morelli, C., Leggio, A., Pasqua, L. The Advent of Molecular Targeted Therapies Against Cancer. Toward Multi-Targeting Drugs Through Materials Engineering: A Possible Future Scenario. Small Science, 2024, 2400113.